MEASUREMENT AND SIMULATIONS OF INTENSITY-DEPENDENT EFFECTS IN THE FERMILAB BOOSTER SYNCHROTRON

BY

DANIEL MCCARRON

Submitted in partial fulfillment of the
requirements for the degree of
Doctor of Philosophy in Physics
in the Graduate College of the
Illinois Institute of Technology

Approved ___________________________
Advisor

Chicago, Illinois
December 2010

ACKNOWLEDGEMENT

Foremost I must thank Linda Spentzouris, my thesis advisor, for helping me see this project to the end, through thick and thin. Often such acknowledgements could come across as somewhat perfunctory, but in my case success was at most times far from certain, and even frequently seemed unlikely. Her assistance and, indeed, persistence, in this manner was no small task, and by all means great credit belongs to her.

I would like, also, to thank Jennifer Gimmell for helping me see the light at the end of the proverbial tunnel, especially regarding a less arbitrary pursuit of brawn than the one with which I was for a decade preoccupied. Without her sense of community and good nature I may never have disabused myself from this habit and the accompanying baggage.

Finally I would like to thank my mother, mostly for her continually enduring hope that I see this to the end, without which the decision to stray from it forever would have seemed not only far more appealing, but, in retrospect, almost assured.

This work is, in my opinion, of a relatively lackluster quality, but nonetheless has exceeded a few expectations, and its final form seems arguably better than it has any right to be. In any case, I may, at least, at long last turn the page...

TABLE OF CONTENTS

CHAPTER

LIST OF TABLES

LIST OF FIGURES

Figure Page

Figure Page

Figure Page

LIST OF SYMBOLS

Symbol	Definition
α	Ratio of running-bucket area to stationary bucket area
β	Relativistic velocity
γ	Relativistic Lorentz boost factor
ε_x, ε_y, ε_L	Horizontal, vertical, and longitudinal emittance
ε_{xy}, ε_{xyL}	Transverse and total emittance
σ_c	Electrical conductivity
c	Speed of light
λ	Longitudinal particle density
χ	Wakefield longitudinal scaling factor
ν_x, ν_y	Horizontal and vertical betatron tunes
R	Vacuum-chamber radius
R_{path}	Accelerator Orbit Radius
h	Harmonic number
γ_T	Transition-energy Lorentz factor
η	Transition slip factor
β_x, β_y	Horizontal and vertical betatron functions
ϕ_s	synchronous phase angle
x', y'	horizontal and vertical particle deflection angles
x,y	Horizontal and vertical coordinates w.r.t design orbit
s	Longitudinal coordinate w.r.t synchronous particle
P	Particle trajectory
δ_p, $\Delta p/p$	Momentum error
f	Quadrupole focal length
B_x, B_y	Horizontal and vertical magnetic field strength
κ	Hill-equation linear-perturbation term
Q_x, Q_y	Fractional parts of the horizontal and vertical tunes

b	Magnet half-aperture
K_x, K_y	Lattice functions for betatron motion
ψ	Betatron phase advance
$(B\rho)$, p/e	Particle-beam magnetic rigidity
ζsc	Space-charge perveance
r_p	Classical proton radius
e	Charge of proton or electron
Ξ	Total number of particles in the beam
B', B''	Horizontal or vertical field gradient
ϕ	Quadrupole rotation angle
K	Particle Kinetic Energy
E, E_T	Particle Total Energy
k	Normalized field gradient
L	Magnetic element length
C_{trim}, C_{skew}	Corrector-element tune change w.r.t. field gradient
P_x, P_y, P_z	Particle-momentum components
C	Covariance matrix
ε_N	Normalized emittance
V, V_{RF}	RF accelerating voltage
ω_{RF}	$2\pi\times$RF frequency
σ_τ	Longitudinal bunch width in time
C	Orbit circumference
ψ_u	Longitudinal separatrix phase at unstable fixed point
D	Momentum dispersion function in horizontal plane
ϑ	Correlation excess from covariance matrix
L/G	ratio of linear to Gaussian area in IPM fitting
r	transverse radial coordinate
a	Beam radius under uniform-beam assumption
σ_{RMS}, σ_{ii}	RMS width of specified beam coordinate
σ_{ij}	Correlation term for RMS widths σ_{ii} and σ_{jj}

N	Number of particles in a typical bunch
M	Number of bunches in the particle beam
$\varepsilon_1, \varepsilon_2$	Laslett coefficients for incoherent motion
ζ_1, ζ_2	Laslett coefficients for coherent motion
B	Longitudinal bunching factor
W_m	mth-moment transverse wake function
Z_m	Impedance (Fourier transform) for mth-moment wake
γ_{damp}	Damping-frequency characteristic for conductor
ω_{rev}, f_{rev}	Particle revolution frequency
J_n	Bessel function of order n
δ, δ_0	Skin depth of material
Ω	Complex mode frequency
τ	Characteristic oscillation growth time
þ	Penetration distance of fields outside chamber boundary
Θ	Vacuum-chamber thickness
ς	Ratio of radial coordinate to RMS transverse width
σ_{ext}	Fitted Gaussian stopband width

ABSTRACT

The Fermilab Booster is a nearly 40-year-old proton synchrotron, designed to accelerate injected protons from a kinetic energy of 400 MeV to 8 GeV for extraction into the Main Injector and ultimately the Tevatron. Currently the Booster is operated with a typical intensity of 4.5×10^{12} particles per beam, roughly twice the value of its design, because of the requirement for high particle flux in various experiments. Its relatively low injection energy provides certain challenges in maintaining beam quality and stability under these increasing intensity demands. An understanding of the effects limiting this intensity could provide enhanced beam stability and reduced downtime due to particle losses and subsequent damage to the accelerator elements. Design of future accelerators can also benefit from a better understanding of intensity effects limiting injection dynamics.

Chapter 1 provides a summary of accelerator research during the 20th century leading to the development of the modern synchrotron. Chapter 2 puts forth a working knowledge of the terminology and basic theory used in accelerator physics, and provides a brief description of the Fermilab Booster synchrotron. Synergia, a 3d space-charge modeling framework, is presented, along with some simulation benchmarks relevant to topics herein.

Emittance, a commonly used quantity characterizing beam size and quality in a particular plane, is discussed in Chapter 3. Space-charge fields tend to couple the motion among the planes, leading to emittance exchange, and necessitating a simultaneous measurement to obtain a complete emittance description at higher intensities. A measurement is described and results are given. RMS beam emittances are shown to be in keeping with known Booster values at nominal intensities and emittance exchange is observed and accounted for. Unmeasurable correlation terms between the planes are quantified using Synergia, and shown to be at most an 8% effect.

Results of studies on the coherent and incoherent shifts of transverse (betatron) frequencies with beam intensity at injection energies are presented. In Chapter 4 the coherent frequency shifts are shown to be due to dipole- and quadrupole-wakefield effects. The asymmetry of the Booster beam chamber through the magnets, as well as the presence of magnet laminations, are responsible for the magnitudes and for the opposing signs of the horizontal and vertical tune shifts caused by these wakefields.

Chapter 5 details the procedures for obtaining a linear coherent-tune-shift intensity dependence, yielding $-0.009/10^{12}$ in the vertical plane and $+0.001/10^{12}$ in the horizontal plane. Data demonstrate a requirement of several hundred turns to accumulate to its maximal value. Two independent studies are compared, corroborating these results.

In Chapter 6, a measure of the incoherent tune shift with intensity puts an upper limit on the magnitude of the direct space-charge effect in the Fermilab Booster. A prediction is made for the representative incoherent particle tune shift using a realistic Gaussian distribution, allowing for growth of the beam envelope with intensity, and found to be $0.004/10^{12}$. The tune-spread dependence obtained by quantification of the resonant stopband width from beam-extinction measurements was measured at $0.005/10^{12}$, similar to the predicted value. These will be shown to be one order of magnitude smaller than the space-charge term from the Laslett tune shift for a fixed-size, uniform beam.

CHAPTER 1

A BRIEF HISTORY OF RESEARCH TO THE EFFECTS OF INTENSITY IN PARTICLE ACCELERATORS

1.1 Synopsis

Here we present an overview of the work in the field leading to current research in space-charge and related intensity-dependent phenomena. We start with the developments in accelerator technology from the 20th century, without which the discussion of intensity limitations in modern synchrotron accelerators would be irrelevant. There follows a discussion of the intensity-dependent effects as they were discovered and/or considered when particle densities became high enough, and highlight the application of these to the Fermilab Booster. Finally, we summarize the development of particle simulations as applied to accelerator physics leading to the work on this accelerator.

1.2 On the Developments Leading to the Synchrotron

One of the first working accelerators used in particle physics was constructed by J. Cockcroft and E. Walton in 1932, who at the behest of G. Gamow were seeking ways to overcome the electrostatic centrifugal barrier inhibiting study of the atomic nucleus [36][1]. These accelerators were electrostatic in nature, which limited them to an accelerating voltage around 1 MV from end to end before dielectric breakdown became a problem. While tandem constructions were devised to bring incremental gains, it was clear that an alternative acceleration scheme was necessary in the pursuit of higher energy. The predecessors of modern linear accelerators were first proposed by G. Ising and R. Widerøe in the 1920s [64,129], who considered a scheme of smaller alternating voltages in

---

[1] Corresponding to references in the Bibliography.

the short-wave-radio range (RF) confined to sections of vacuum pipes to achieve these higher energies. Their ideas were implemented by E. Lawrence and D. Sloan. Sloan built the first linear accelerator employing this effect in 1931 [115].

While this overcame the problem of dielectric breakdown, achieving higher energies in this fashion for lighter particles (i.e. electrons or protons) eventually meant the production of very long vacuum chambers, which was impractical at the time. To circumvent this problem, Lawrence went on to develop the first cyclic accelerator, the cyclotron, designed in 1929 and eventually patented in 1934 [77]. For constant magnetic fields, the orbit of the particles was spiral-like in nature due to their increasing velocities, and the number of repeated accelerations was limited by the size of the magnet. In 1940 D.W. Kerst developed the betatron [68, 69, 70], the first cyclotron relying on an induction-based scheme by varying the current in a massive central magnet to accelerate particles in many repeated, circular orbits, and compensating somewhat for the particle-velocity increase.

Although energies (of electrons) of up to 300 MeV were achieved this way, relativistic effects (effective mass increase) eventually limited the efficiency of this induction-powered acceleration. To overcome these effects, the synchrotron accelerator was proposed, independently by V. Veksler in 1944 and E. McMillan in 1945 [87, 123] (and purportedly unofficially by M. Oliphant [105] several years earlier). Particles are injected at sufficient energies through other means and are then accelerated by electric fields while being steered in a cyclic path by powerful dipole magnets. Veksler and McMillan realized that sinusoidal RF accelerating fields synchronized to the particle motion provided a certain amount of longitudinal stability, allowing for much higher energies than with previous accelerator designs. To this end, magnetic field strengths and frequencies are ramped to maintain the orbits of the particles under their increasing velocity and relativistic masses. While orbit control is still limited by the maximal magnetic field, unlike the cyclotrons, this design more or less removes the former size requirements of the necessary magnetic elements in the pursuit of higher energy.

The first high-energy synchrotron, the Cosmotron at Brookhaven National Laboratory, was constructed in 1948, reaching a particle energy of 3.3 GeV by 1953. A 10-GeV synchrotron would follow in the U.S.S.R. in the late 1950s. Energies steadily increased over the next few decades, in part due to the parallel development of high-powered RF generators and the improvements in superconducting magnet technologies. Such accelerators have since been employed almost exclusively in the high-energy regime[2], well into the TeV range with the Tevatron at FNAL and the newly commissioned LHC at CERN.

1.3 Intensity Improvements and the Collective Effects within Particle Beams

Beam intensity has become at least as important as beam stability. Experiments utilizing high-energy colliders often take months or years of run time, and depend very much on statistics, for which the frequency of events is paramount to achieve precise results within reasonable time scales. Some steps leading to improvements in beam intensity, and the subsequent challenges associated with them, are detailed in the following.

1.3.1 Alternating-Gradient Focusing. The physics of low-intensity beams (essentially

---

[2] For electron synchrotrons, a practical limit is eventually reached over 100 GeV because of significant energy loss due to synchrotron radiation, which scales as $(\text{mass})^{-4}$. Hence for protons, the necessary energies (10^{22} eV) for this to manifest itself may never be reached with synchrotron technology.

single-particle dynamics) has been studied since the 1930s, though much of this was secondary to the achievement of energies in working cyclotrons, given the rather meager attainable intensities by modern standards. In 1949, the invention of alternating-gradient or strong-focusing techniques by Christofilos [35] and independently by Courant, Snyder, Livingston and Blewett in 1952 [41] brought the potential for an increase in particle density practically unattainable with previous focusing methods (now called 'weak' focusing) as particle energies entered the GeV range. Such a design permitted separate functions for each magnetic element, helping to mitigate the magnetic saturation present when higher field strengths were employed, while significantly reducing the size of the magnets needed by minimizing the size of the beam. Almost all modern accelerators utilize this strong-focusing and separate-function design.

While interest in space-charge effects started during the 1950s largely in the plasma physics community, especially in the area of magnetic-confinement fusion [57, 121], by the 1960s, steady improvements in beam intensity, along with the prediction of synchrotron radiation by Pomeranchuk and Ivanenko in 1944 [65] (verified observation by Langmuir in 1946 [50]) necessitated the understanding of these collective effects in particle beams, both for high-energy colliders and the eventually emerging synchrotron light sources, the uses of which would soon greatly eclipse the applications of the collider accelerator.

1.3.2 Courant-Snyder Theory of Beam Dynamics and Space-Charge Forces. Following the implementation of the alternating-gradient focusing method, the groundwork for a description of beam dynamics in periodic focusing systems was first laid out by Courant and Snyder [39]. This was the first systematic discussion of the beam properties in terms of its single-particle motion, its maximal extent, or envelope, its oscillation phase, and a motional invariant later known as emittance. The formalism, using the method of Floquet transformation, has turned out to be far more general and was in fact developed many times in many disciplines. A historical overview has been prepared by R.C. Davidson and H. Qin [99,100]. Extension of this Courant-Snyder framework to space-charge forces in the presence of magnetic-focusing errors was done by F. Sacherer in 1968 [109], bringing better understanding to conditions for stable operation in an accelerator.

Much of the theory of the interactions within the beam under increasing intensity was extended from the domain of plasma physics. The cumulative work of R. Davidson [43] put the physics of collective effects in beams on a sound theoretical footing by incorporating the theory presented by A. Vlasov 20 years earlier [124-126]. The Vlasov equation describes the long-range Coulomb interactions within an ensemble of charged particles (a veritable staple in the plasma-physics community) and was applied equally well to high-intensity accelerator beams. This allowed for a complete, self-consistent[3] description of the evolution of the beam distribution under self- and external forces. A thermodynamic description of the beam was introduced by M. Reiser in the 1970s [101], and a statistical definition of this emittance introduced by Courant and Snyder was developed by P. Lapostolle in 1971 [71]. These concepts helped pave the way for the development of techniques to maintain or improve beam quality, such as stochastic cooling [122] and a variety of beam-manipulation methods colloquially referred to as "phase-

---

[3] "Self-consistent" in beam and plasma physics refers to systems whose evolution in time due to internal and external forces can be completely described by those same forces regardless of their commensurate dependence on the distribution change.

space gymnastics," where the phase-space portrait of the particles is modified to optimize certain beneficial properties of the beam.

Since the 1980s, further work has been done primarily by I. Hofmann [61], with others such as G. Franchetti, A. Fedotov, R. Gluckstern, to generalize this to the dynamics caused by nonlinear space-charge forces for various distributions using both the Vlasov and thermodynamic descriptions. Comprehensive discussions of the nonlinear Hamiltonian and Vlasov descriptions of the dynamics of particle beams have been well established and can be found in several modern textbooks on the topic.

1.4 Interaction with the Surroundings

With an increase in intensity, the interaction of the beam and its surroundings (i.e. the vacuum chamber) became important, as other potential instabilities were driven by this response. In 1963, L.J. Laslett was the first to consider the effect of a conducting chamber on the transverse oscillation frequencies of the particles in a high-intensity beam [73]. It was shown that for lower energies, the majority of the effect came from electrostatic repulsion within the beam, while for higher energies, the magnetic self-field cancellation inhibited this and the response from the vacuum chamber became the dominant factor. The inclusion of an imperfectly conducting structure (as most materials tend to be) was soon investigated by Laslett, Neil and Sessler [76], who showed that the resistive behavior of the material could produce transverse-oscillation growth under certain circumstances. The growth rate depended on the value of this resistivity within various frequency regimes due to the time-dependent fields of the passing beam.

This work culminated in an impedance-based description of this phenomenon, first presented by Sessler and Vaccaro in 1967 [111]. These concepts were later generalized by Sacherer and Nassibian [89], who recast the impedance in terms of driving particles (in front) and receiving particles (in rear), allowing for a description of impedance phenomena dependent both on the beam distributions as well as on chamber geometries. A detailed summary describing the analytical methods developed for calculating impedances has been performed by R. Gluckstern [55]. Recent publications by others [18,22,59] have also promoted better understanding of the impedance effects in the Fermilab Booster.

1.5 Prior Measurements of the Booster Impedance and the Known Complications

The Booster presents a complication in that much of its (noncircular) geometry is comprised of magnets constructed from stacked, epoxy-insulated laminations, which has been shown to measurably change the impedance behavior over a nonlaminated structure. A general discussion of the problem of transverse instabilities in the presence of laminated structures was completed by B. Zotter in 1969 [136]. The first analyses of impedance effects in the Booster were done by A. Ruggiero [106-108] and S.C. Snowdon [116] in 1970, who made predictions on the effect of the laminations on the longitudinal motion. Attempts to quantify the transverse coupling impedance as well have been done over the past years by R. Shafer [112], J. Crisp [42], and V. Lebedev [78]. A survey of the problem first detailed by Ruggiero, with further analysis, has been done by Gluckstern [54], and more analytical treatments have been given separately by A. Burov [19] and K.Y. Ng [91] in recent years. However, the problem of understanding the properties of the transverse impedance in the Booster and all of its important effects on beam stability, additionally taking into account these laminations, is considered rather formidable and to date has not been completely described.

1.6 Particle Simulations for Accelerators and the Application to the Booster

As with all many-particle, nonlinear systems, beam dynamics including space charge is analytically intractable, and many properties must be extracted using numerical methods. The mainstay of particle simulations, the so-called particle-in-cell technique, was developed in the late 1950s by the fluid mechanics community, in particular for the study of turbulent effects [58]. The application to plasma instabilities was soon to follow in the next two decades [44]. Advances in computing power have allowed its application to accelerators, where in addition to the nonlinear self-forces, hundreds of accelerator elements must be considered. Many particle-tracking codes have been developed over time, but in application to the Booster, the most recent work on simulating space-charge dynamics was done by S. Stahl in 1991 [117], before the Booster injection-energy upgrade from 200 MeV to 400 MeV [110], and before the commissioning of the Main Injector in 1993. Intensity has been significantly increased since then, and other considerations such as the inclusion of a more realistic Booster geometry necessitate a refresh of this work.

CHAPTER 2

BASIC ACCELERATOR TERMINOLOGY, BOOSTER TECHNICAL DETAILS, AND INTRODUCTION TO THE SIMULATION TOOLS

2.1 Some Fundamentals of Accelerator Physics

The primary impetus for the understanding of the effects of increasing particle intensity, both through mutual Coulomb interaction (space-charge) as well as the response from the surrounding vacuum-chamber, on particle-beam dynamics in circular accelerators is the desire to increase the luminosity of particle colliders, and, to a lesser extent, the brightness of synchrotron light sources, both of which are strongly dependent on intensity. We focus our discussion on the FNAL Booster, on which this work is based. During its nearly 40 years of operation, as of this writing, it has served as an intermediate synchrotron accelerator between the FNAL Linac and some accelerator bringing particles to their highest energy, most recently the Tevatron. Over the years, an increase in Tevatron-beam intensity has been achieved in part through an increase in Linac energy into the Booster from 200 MeV to 400 MeV, as well as from the construction of a larger-aperture Main Injector between the Booster and the Tevatron.

With the capability for a greater number of protons into the Tevatron, the Booster's workload (number of particles per pulse) has increased from well below its design intensity in the 1970s to (currently) roughly twice this intended limit during normal operations. Additionally, the need for protons in the production of neutrinos in both the NuMi and Miniboone experiments has pushed the intensity demands on the Booster further, by requiring a more continuous operation at these higher limits. Figure 2.1 presents a schematic of the current Fermilab accelerator chain.

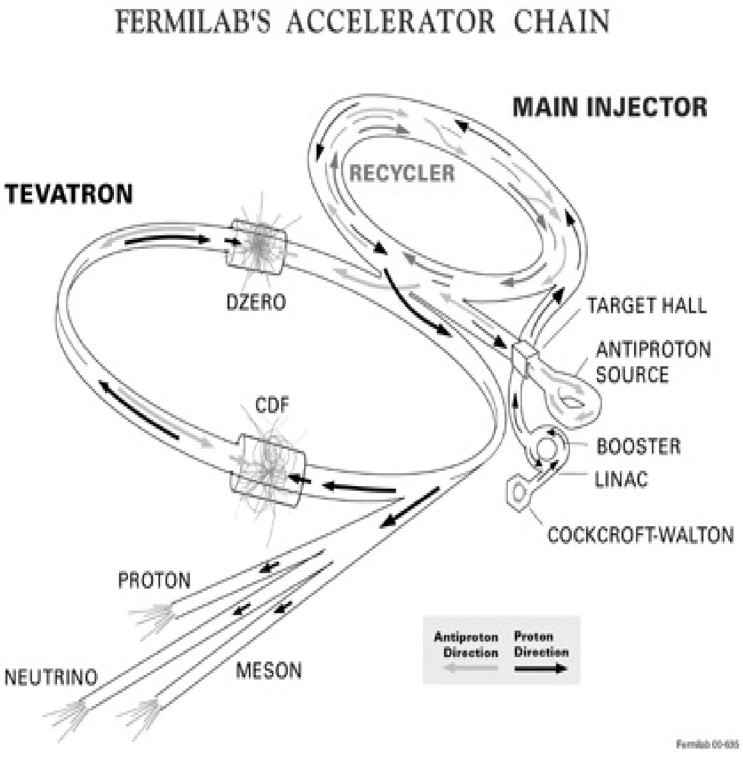

Figure 2.1. Schematic of the Fermilab Accelerator Chain (courtesy Fermilab Visual Media Services)

Intensity effects are an important consideration, for the following reason. To first order, particles are maintained in the ring of a circular accelerator by strong magnetic fields with dipole fields to steer the beam and quadrupole fields to focus it transversely. The formalism of the dynamics is well understood and very analogous to that of linear optics. To first order, these would be sufficient to contain the beam. But magnets are not perfect, of course, so higher-order correction (sometimes called “trim”) elements (rotated quadrupoles, sextupoles, etc.) are then utilized to maintain certain beam parameters within respective ranges required for stable operation and proper containment by the strong dipole and quadrupole magnets. The effect of these beam-focusing and correction elements may be reduced due to intensity-dependent Coulomb repulsion of large numbers of charged particles within the confines of the vacuum chamber. Furthermore, increasing intensity may cause the beam distribution and corresponding properties to change undesirably, leading in some cases to certain beam instabilities (resonances) and ultimately beam loss or breakup. To make matters worse, the surrounding vacuum chamber, comprised of many elements from magnets to accelerating cavities, also interacts more strongly with a beam of increased intensity, usually in a manner inimical to beam stability as well. Generally, these two effects, the mutual interaction of the particles on each other, as well as the interaction of the surroundings on the beam as a whole, are considered to be self-forces, since their existence depends on the beam intensity specifically.

2.1.1 Accelerator basics. We provide in this section an introduction to the accelerator-physics concepts utilized throughout. The purpose is to provide more of a working knowledge rather than a complete or comprehensive description of the terminology. A more complete treatment on introductory material can be found elsewhere [37, 47, 62, 80]. Further extensions or details will be provided *in situ* as needed.

2.1.1.1 Coordinate Description, Beam and Synchronous-Particle Definitions. The function of a particle accelerator, as the name suggests, is to increase the energy of charged particles, ultimately for collision with other particles or as a generator of high-brightness light. Generally, accelerators follow two main designs - single-pass, linear accelerators and multi-pass, circular accelerators. 'Circular' is a common description though somewhat imprecise. While they are closed, periodic structures, very few of them truly resemble circles. A 'ring' is perhaps a better term. In these accelerators, particles travel in orbits over many revolutions, being steered in their repeated path by powerful dipole magnets. The collection of particles, i.e. the beam, possesses a small transverse momentum relative to the longitudinal. For example, in the Booster, particle transverse momenta are typically no larger than 40 keV⁄c while forward momentum can range from around 900 MeV⁄c to 8 GeV⁄c within the cycle.

In any accelerator with energies over several MeV, alternating electromagnetic fields (colloquially termed RF, since their frequencies are generally in the radio range) provide the energy gain to the particles. Practical reasons have necessitated their use. First, electrostatic acceleration methods have been limited to around 1-2 MV⁄m before the need to avoid dielectric breakdown greatly complicates the design. Secondly, a certain amount of longitudinal stability is achieved *a priori* using sinusoidal fields, which are readily available using high-powered RF generators. Since oscillating fields would accelerate (positively) charged particles on the positive portion of the waveform and decelerate them on the negative, the beam must be shielded from the latter to ensure consistent acceleration. A beam thus comes in roughly equally longitudinally spaced “bunches” confined to the spatial extent of the instantaneous accelerating portion of the RF field. Because the longitudinal width is determined by the frequency of this RF field, it is often expressed experimentally in such terms, e.g. a bunch in a 200-MHz field is 200 MHz "long." This accelerating field must be some integer multiple of the revolution frequency (the so-called harmonic number), depending on how many bunches are designed to fit in the orbit circumference. Since the revolution frequency naturally increases with increasing energy (at low energies, at least), the location in the cycle is often quoted in terms of the number of revolutions, or 'turns,' rather than time.

Ideally, all particles would travel along a particular trajectory (design orbit) with a particular energy. Such an ideal particle is referred to, for reasons that will discussed, as the synchronous particle. Naturally, particles will not follow this trajectory exactly. Coordinates are based on the slight deviation relative to this synchronous particle. The motion is separated distinctly into transverse and longitudinal parts, requiring in general six coordinates to describe it fully. For a circular accelerator, a particle trajectory P is customarily described by (x, y, s) where x, y are the transverse positions (horizontal and vertical, respectively) relative to the beam centroid (so-called synchronous orbit) and s is the "absolute" longitudinal coordinate.[4]

The transverse particle deflection angles are defined by $x' = dx/ds$, $y' = dy/ds$, and are proportional to a particle's transverse momenta. Specifically, for $p_z >> p_{x,y}$ we may write $x' = p_x/p \approx p_x/p_z$ and similarly for y'. Hence they are conventionally used as the conjugate variable to position. In the s-direction we define the momentum error δ_p and the relative longitudinal position z given by $\delta_p = \Delta p/p$ and $z = s-\beta ct$, where p is the forward momentum of the synchronous particle, and βc is its velocity. The six coordinates describing the dynamics of a particle in the beam are then $P(x,x',y,y',z,\delta p)$. Often, the energy error δE through some characteristic transit time t is used instead of momentum and position error. An equivalent representation could then be $P(x,x',y,y',t,\delta E)$.

2.1.1.2 Lattice, Field Gradient, Quadrupole Focal Length. Because the energy difference between transverse and longitudinal motion differs commonly by several orders of magnitude, the dynamics of particle beams are almost always separated rather distinctly along these lines. The transverse motions of particles with such displacements relative to

---

[4] s can be periodic (taking values up to the circumference of the ring), or continuous, monotonically increasing. Since the particles see the same elements in the same physical locations, the periodic definition is more practical for our purposes.

the design orbit are maintained through sequential, orthogonal quadrupole fields arranged to provide alternating-gradient focusing, analogous to the systems of lenses in classical optics. Beam-centroid position is likewise maintained near the design orbit in the horizontal plane through dipole fields. In principle these elements provide sufficient linear restoring forces to maintain the beam in its orbit indefinitely. In practice higher-order magnetic multipoles are necessary to correct for certain nonlinear effects. Generally speaking, the periodic collection of magnets and drift spaces responsible for maintaining this transverse stability is referred to as the accelerator lattice.

The overall effect of these elements on the particles depends on their energy as well as the length of the magnet the beam traverses. While magnets are indeed of finite length, a "thin-lens" assumption, equivalent to the term in optics, is usually made wherein this length is very small relative to a relativistic, passing beam such that any focusing or deflection can be treated as if the magnet were of zero thickness. Hence the important quantity is not its field or field gradient, but the integrated field/field gradient over this longitudinal distance, i.e.

$$\int_0^L B^{(n/2-1)} dl \tag{2.1}$$

where (n/2-1) is the order of the transverse derivative of the n-pole field (zero for dipole, one for quadrupole, etc). The quadrupole will be of particular importance particularly in the subsequent section, so we detail it here.

The horizontal and vertical field components of a quadrupole oriented in the transverse plane are linear, and given by

$$B_x = \frac{\partial B_x}{\partial y} y, \qquad B_y = \frac{\partial B_y}{\partial x} x \tag{2.2}$$

By design, these components are usually equal, so that

$$B_x = Cy \qquad B_y = -Cx \tag{2.3}$$

where C is the uniform field gradient of the symmetric quadrupole. Naturally, this leads to a focusing in one plane and a defocusing in the other. If B is expressed in Gaussian units (MV/m or such), the "focal length" f of such a device can be written as

$$\frac{1}{f} = \frac{\int_0^L B'dl}{pc/e} \tag{2.4}$$

where p/e[5] is the magnetic rigidity of the beam given as the ratio of the momentum to the electric charge (higher-energy beams are 'stiffer' and more difficult to bend and focus). Proper periodic placement of these quadrupoles results in a sustainable restoring force to the beam.

2.1.1.3 Tune, phase advance, β-function, tune shift. As mentioned previously, particles bound in this accelerator lattice are thus subject to periodic magnetic restoring forces, hence the single-particle dynamics can be described, to first order, by the Hill equation.

$$\frac{d^2x}{ds^2} + K_x(s)x = 0 \tag{2.5}$$

where K(s) is the periodic focusing function provided by magnetic quadrupole elements distributed periodically around the ring. Its general solution is given by

$$x(s) = A\sqrt{\beta(s)}e^{\pm i\psi} \qquad \psi = \int_0^s \frac{dt}{\beta(t)} \tag{2.6}$$

---

[5] Often the rigidity is expressed as what is intended to be a single symbol '(Bρ)', representing the product of some bending field and the radius of the beam being bent by such a field. While far more ubiquitous in the literature, we shall seek to minimize the use of this expression in favor of the ratio p/e.

where β(s) is the so-called ‘beta-function,’ or 'betatron function',[6] a longitudinally varying quantity depending on the strength and spacing of the quadrupole magnets around the ring. Physically it may be interpreted as the instantaneous wavelength (divided by 2π) of a particle undergoing this transverse motion. $A\sqrt{\beta}$ represents the particle oscillation amplitude at s. Since β varies with s, so does the amplitude. The capabilities of the magnetic focusing elements determine this beta function.

The quantity ψ is referred to as the betatron phase or phase advance. If 2π is the complete phase angle representing one complete transverse oscillation of the particle, then the number of oscillations per turn (horizontal or vertical) may then be written as

$$\nu = \frac{1}{2\pi}\oint \frac{ds}{\beta(s)} \tag{2.7}$$

ν is referred to as the betatron *tune* of the accelerator. This tune, and the perturbations affecting it (tune shift), are of paramount importance in assessing beam stability under certain conditions.

The most notable of these stability issues is the onset of so-called betatron resonances. Particles the fractional part of whose tunes are integer harmonic numbers, i.e. 1, 1⁄2, 1⁄3,...,1⁄n, will arrive at the same betatron phase at any particular location in the accelerator after n turns. This also applies to values m⁄n, where m and n are integers and m<n, only the repeat period is every m×n turns. In the presence of gradient errors, however small, these particles will experience ever increasing amplitude growth from this error,

---

[6] The nomenclature is merely historical. The analysis of transverse motion of this type was first formally analyzed in betatron accelerators. All accelerators naturally exhibit this behavior.

ultimately leading to beam loss. In principle, this would apply to every rational number, essentially cluttering tune space like a minefield. In practice, because of certain damping mechanisms and other nonlinear effects, the first three are often the most important to avoid. Preparation of the accelerator lattice should intend to avoid these resonances, but effects shifting the tune substantially enough can foil this careful design.

The tune shift due to a perturbing force can be calculated for a single particle from the Hill equation (2.5). While such an approach provides an understanding of how certain quantifiable forces on particles in a beam affect this tune, such a framework also has certain limitations, discussed in the following section.

To calculate this shift in the tune in the presence of small external forces, we modify (2.5) in the presence of a perturbation. Let ν_0 represent the unperturbed tune. Then the equation of motion can be written in terms of the unperturbed frequency of oscillation,

$$\frac{d^2(x,y)}{ds^2}+\left(\frac{\nu_{(x,y)_0}}{R_{path}}\right)^2(x,y)=0 \tag{2.8}$$

where R_{path} is the accelerator radius. Let us consider a linear perturbation, κ, in the restoring force in (2.8). Let ζ represent either x or y, such that

$$\frac{d^2\zeta}{ds^2}+\left(\frac{\nu_{\zeta_0}}{R_{path}}\right)^2\zeta=\kappa\zeta \tag{2.9}$$

κ is small enough such that

$$\kappa\ll\left(\frac{\nu_{\zeta_0}}{R_{path}}\right)^2 \tag{2.10}$$

For this small perturbation we may approximate

$$\Delta\nu_\zeta = \nu_\zeta - \nu_{\zeta_0} \approx \frac{-\kappa R_{path}^2}{2\nu_{\zeta_0}} \tag{2.11}$$

We wish to express this in terms of the actual forces acting on a particle. (2.9) has the form of the simple-harmonic oscillator, in which case κ can be written as

$$\kappa = \frac{F/\zeta}{\gamma m\beta^2 c^2} \tag{2.12}$$

where γm is the relativistic particle mass and βc is the velocity[7]. F is the unwanted force perturbing the particle motion. The tune shift is then given by

$$\left|\Delta\nu_\zeta\right| = \frac{F/\zeta}{\gamma m\beta^2 c^2}\frac{R_{path}^2}{2\nu_{\zeta_0}} \tag{2.13}$$

We note that unless the force is linear with the transverse coordinate ζ, the linearized particle tune-shift is position-dependent. The tune shift presented will be applied to the case of a uniform beam to estimate the relative contribution of space-charge to the effects of a conducting vacuum chamber in Section 4.2.

One of the shortcomings of the preceding single-particle approach is that it does not account for the dynamics of collective motion. A particle beam is not a "frozen" collection of particles traversing the same path element by element. Particle trajectories differ in maximal amplitude as well as in tune. The resulting collective motion amounts to a dynamic beam envelope, and space-charge effects play a role in its evolution. A full description of this motion is necessarily distribution-dependent.

In order to obtain a dynamical equation for the beam envelope, rather than a sin-

---

[7] Unfortunately, β is substantially overemployed in accelerator physics. While the meaning should be clear from context alone, we shall strive to make it unambiguous.

gle-particle equation, a description of the particle distribution is needed. A beam distribution frequently is modeled transversely by an elliptical Gaussian function. Such distributions, though both realistic and accurate in their own right, are not valid indefinitely, since the forces within the beam changing the distribution, and the change in this distribution then modifying the forces will not maintain this Gaussian behavior. That is, the resulting equations of motion are not self-consistent. Given a linear space-charge self-force, we seek a four-dimensional ellipsoidal distribution (x,p_x,y,p_y) giving rise to this linear space charge force which in turn allows the ensemble to maintain the ellipsoidal distribution it started with. Such a distribution can be written formally as

$$\psi\left(x,p_x,y,p_y\right)=\frac{\lambda}{\pi^2\varepsilon_x\varepsilon_y}\delta\left(\frac{x^2}{x_{env}^2}+\frac{x_{env}^2p_x^2}{\varepsilon_x^2}+\frac{y^2}{y_{env}^2}+\frac{y_{env}^2p_y^2}{\varepsilon_y^2}-1\right)\tag{2.14}$$

where x_{env} and y_{env} are the horizontal and vertical beam-envelope dimensions and ε_x, ε_y are the horizontal and vertical emittances, and δ is the Dirac delta function. Emittance will be discussed in detail in Sections 4.1-4.3. For these purposes we consider them constant beam parameters characterizing the envelope size. First found by Kapachinskij and Vladimirskij, this (KV) distribution is of infinite extent longitudinally, and its 2-D transverse projections lead to uniform elliptical distributions [66]. The advantage of this lies in its linear space-charge forces and resulting envelope equations, which give analytic results. For this distribution the RMS beam widths, $\sigma_{x,y}$ behave as follows:

$$\sigma_x''+\left(\frac{\nu_x}{R_{path}}\right)^2\sigma_x-\frac{\varepsilon_{rms}^2}{\sigma_x^3}=\frac{\xi_{SC}}{4\left(\sigma_x+\sigma_y\right)}\tag{2.15}$$

$$\sigma_y''+\left(\frac{\nu_y}{R_{path}}\right)^2\sigma_y-\frac{\varepsilon_{rms}^2}{\sigma_y^3}=\frac{\xi_{SC}}{4\left(\sigma_x+\sigma_y\right)}\tag{2.16}$$

where the primes refer to differentiation with respect to the longitudinal coordinate and

ξ_{SC} is a parameter depending on intensity, corresponding to how strongly the space-charge fields disrupt the independent motion. ξ_{SC} is often referred to as the "space-charge perveance," and is given by

$$\xi_{SC} = \frac{e^2 r_p \lambda}{\beta^2 \gamma^3} \tag{2.17}$$

where r_p is the classical proton radius and λ is the linear density of particles with charge e.

For general distributions analytical solutions are less tractable (or impossible) and require numerical techniques and/or simulation to obtain quantitative results. The KV distribution is used extensively in such cases as a comparison to simulation models. Furthermore, other (realistic) distributions sacrifice the rigorous self-consistency present in the KV case, but to the extent that particle information is recalculated periodically in simulations, this issue can often be circumvented.

2.2 The Fermilab Booster Synchrotron

The Fermilab accelerator chain is currently a tool for high-energy research, producing collisions between protons and antiprotons at a center-of-mass energy of 1.96 TeV at an integrated luminosity (as of 2009) of 60 pb^{-1}. Both the cost and technical challenges of constructing a single accelerator capable of accelerating particles from the energies from the Linac to 1 TeV with sufficient intensity make such an effort practically infeasible. Such an undertaking has required the construction of several accelerators designed to accelerate particles within particular energy ranges leading to the TeV scale. A diagram of the accelerator chain was provided in Figure 2.1. We present a working description of the Booster in the following sections. The full technical details are documented elsewhere [16, 132].

2.2.1 Booster Function and Intensity Limitations. The Booster's primary function is as a proton source, receiving 400-MeV particles from a linac and accelerating them to 8 GeV before extraction to a large-aperture Main Injector. The Booster's more recently implemented secondary function is to provide protons to target for the production of neutrinos in the MiniBoone experiment. To provide the necessary protons to target or extraction, the Booster has been designed as a rapidly cycling accelerator, providing currently around 5×10^{12} protons per pulse at a rate of 15 Hz.

A substantial part of the intensity limitations with the Booster are due to its relatively lower-energy beam. It will be shown that space-charge forces scale with energy as γ^{-2}. Since particles at the energies near injection are not very relativistic (with $\gamma = 1.4$), space-charge forces, largest at this point, play a significant role in the beam dynamics.

Currently the Booster is being operated at an intensity twice that of its design to meet the proton requirements in the experiments. Integrated losses due to intensity have become a problem under these circumstances, requiring, among other things, the installation of collimators to mitigate the eventual resulting damage to diagnostics and radioactivation of the accelerator elements [88]. With typical intensities, it has been estimated that 10-20 kGy[8] of radiation has been deposited over its lifetime, with as much as 200 kGy in some locations, especially near epoxy magnet insulations [45]. Because of the demands by the neutrino experiments this number has been projected to exceed 1 MGy by 2015 [46]. While studies have shown magnet insulations accommodating as much as ten times this value [51], this amount of localized dose is of some concern, and minimizing beam

---

[8] 1gray is the absorption of 1J of energy in the form of ionizing radiation by a mass of material of 1kg. I.e. 1Gy=1J/kg

loss is thus extremely important.

2.2.2 Booster Lattice and Design. The FNAL Booster is a circular accelerator with a radius 74.5 meters. As with all such accelerators, "circular" is a loose description for a collection of regular, repeated sections forming a closed, periodic structure. In the case of the Booster, it is comprised of 24 such sections, or cells, (so for the pedant, Booster is closer to an icosakaitetragon, or such, than a ring). Each cell is comprised of four combined-function magnets (dipole-plus-quadrupole) 2.9 meters in length, interspersed among regions of drift space. Since the basic structure of the accelerator is periodic, the start of the cell is somewhat arbitrary. Conventionally, it is represented by the shorthand "FOFDOOD," i.e. a periodic sequence consisting of a (horizontally) focusing magnet (F), a "short" drift space of 1.2 meters, a second such magnet, a defocusing magnet (D), a "long" drift space of 6 meters (OO), and another defocusing magnet. Naturally, in the vertical plane, this would correspond to DODFOOF. The drift spaces (also referred to as "straight" sections) are identified colloquially as "long" and "short," and numbered starting from beam-injection location (i.e. Long 1). Beam travels downstream from Long 1 to Short 24, and then repeats. Figure 2.2 shows the schematic of the cell arrangement.

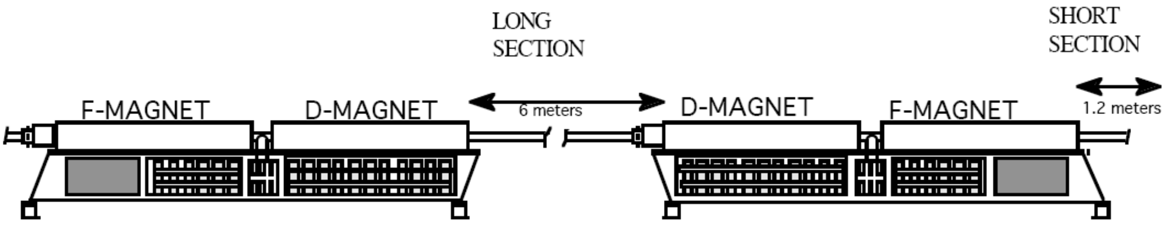

Figure 2.2. Schematic of Booster Magnet Arrangement (FDOODFO) (Courtesy B. Worthel, 'The Booster Rookie Book, V.3.0', 1998, p.15)

The long drift sections house a series of diagnostic tools, particularly beam position monitors (BPM's), as well as magnetic corrector elements and the RF accelerating cavities. The short sections as well hold additional corrector elements.

2.2.3 Beam Correction Elements. The original design had corrector packages comprised of "trim" dipoles and quadrupoles to compensate for steering and focusing errors, as well as skew-quadrupoles for transverse coupling correction. All short and long straight sections contain these types of correctors. Sextupoles, both nominal and skewed, were added shortly afterward to various cells when it was apparent that chromaticity and the third-integer harmonic also played a measurable role in affecting the beam. A single octupole, to correct for large-amplitude betatron motion, was further introduced, though this effect was found to be less important than the chromaticity.

As the operating intensity met and surpassed the design intensity, the strength of these magnets became insufficient further from injection. From 2007 to 2009 these elements were replaced by packages of self-contained, individually controlled units in all 48 sections. The upgraded elements consist of all magnet poles save for the octupole [67]. Since studies done for this research were done utilizing both new and old correctors, both specifications are provided for reference [15, 95]. Table 2.1 juxtaposes the relevant qualities of these corrector sets. It is to be noted that the skew-quadrupole and sextupole strengths were considered sufficient and their strengths were not significantly modified during the upgrade, though the magnets themselves were of course replaced to allow for precise, individual control if necessary.

Table 2.1. Juxtaposition of Old and New Booster Corrector-Magnet Strengths

Type	Integrated field/field gradient (former)	Integrated field/field gradient (latter)	Relative Improvement
H. Dipole	30 g-m	90 g-m	3
V. Dipole	30 g-m	150 g-m	5
Quadrupole	220 g	800 g	3.64
Skew Quadrupole	80 g	80 g	1
H. Sextupole	1.41×10^4 g⁄m	1.41×10^4 g⁄m	1
V. Sextupole	1.41×10^4 g⁄m	1.41×10^4 g⁄m	1

Families of trim elements are electrically connected such that the fields of all magnets of a similar type in either a short or long section are controlled simultaneously (i.e. all dipoles, quadrupoles, or skew-quadrupoles in the short or long sections have one control for each group). To ensure that the magnets affect the beam uniformly cell by cell, the currents of these magnets are scaled to the betatron phase at their respective locations.

2.2.4 Transverse and Longitudinal Profile Monitors. At the minimum, a feedback mechanism to maintain the beam in its orbit over the many revolutions is critical to the stability of operation. This is accomplished by the use of passive Beam Position Monitors (BPM's), devices that measure the center-of-mass position of the particle distribution. The Booster has 102 of these, four per cell and six more for certain specialized purposes. Naturally, more than just BPM's are necessary to obtain a more complete picture of the beam behavior. Compared to diagnostics in other machines in the accelerator chain, the Booster, constructed much earlier, is conservatively equipped. Two instruments utilized in the experimental results discussed in this work measure the transverse beam width and longitudinal bunch width per turn - the Ionization Profile Monitor (IPM) and Resistive Wall Monitor (RWM) respectively. In what follows we discuss the operation of these.

2.2.4.1 The Ionization Profile Monitor (IPM). The vacuum in the accelerator is not perfect. The residual gas particles present in the chamber can, however, be used to obtain details of the transverse beam distribution. The details of the instrument [134] are well documented, but a schematic illustrative of the IPM in operation is provided in Figure 2.3, as well as a typical profile obtained at 450 turns into the cycle. Particles ionized by the passing beam are collected onto micro-channel strips 1.5mm in width by a 5-kV potential. The ion count per strip depends on the charge of the beam in the vicinity. Independent calibration techniques [5] have produced reliable transverse beam-width profiles for both the horizontal and vertical plane.

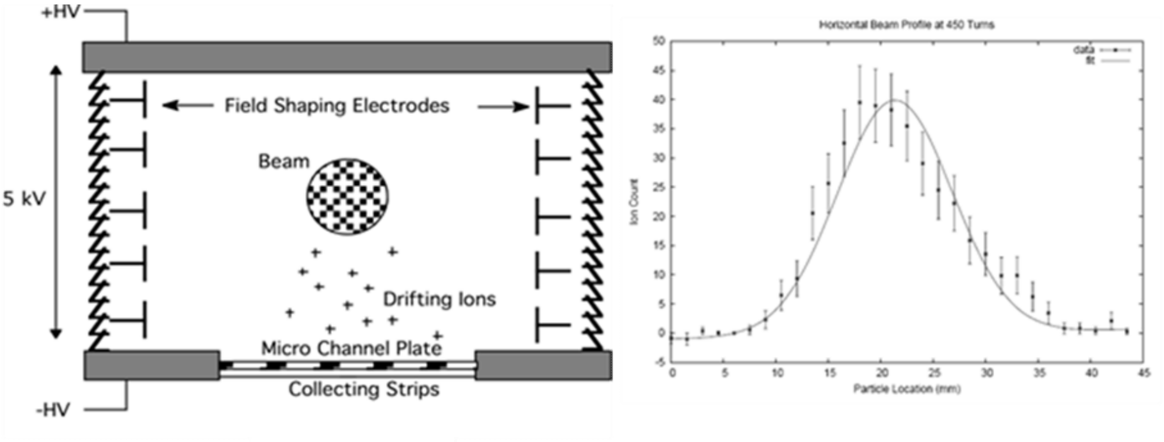

Figure 2.3. IPM Schematic (left) and Typical Fitted Beam Profile (right) at 450 Turns in the Cycle. Signal Amplitude is with Respect to the Center of the Detector (left figure courtesy J. Zagel and B. Graves).

2.2.4.2 The Resistive-Wall Monitor (RWM). Longitudinal density profiles are obtained by the so-called resistive-wall monitor [127]. Passing beam excites fields in the pipe walls. A measurable potential difference at a gap separating two vacuum-chamber elements is created using a resistive ceramic insert interfaced to a pickup, usually an oscilloscope. Signal response depends on the instantaneous longitudinal charge density. Figure 2.4 provides a conceptual schematic of this device, as well as a typical longitudinal profile 30 ms (15 turns) into the cycle.

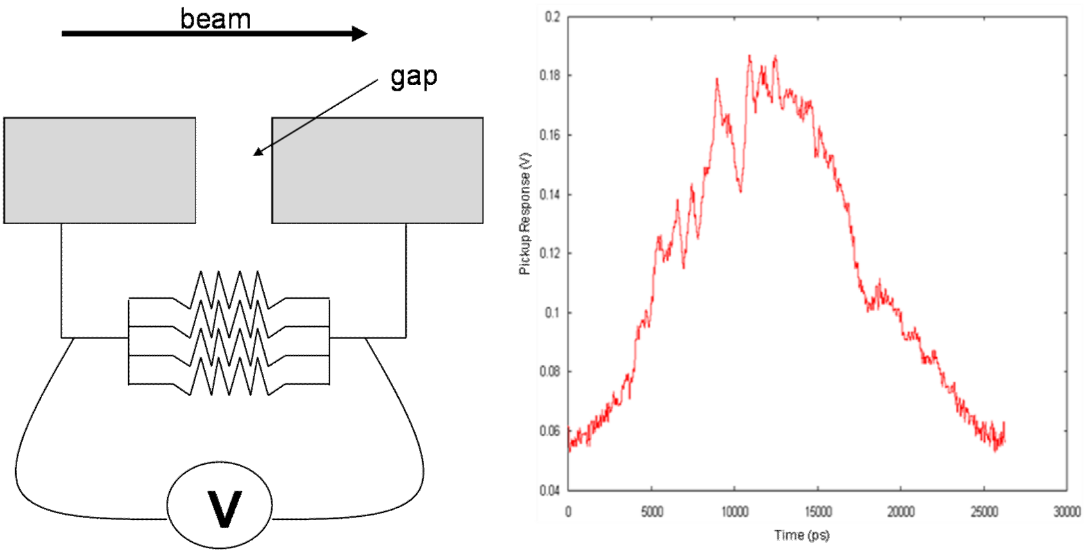

Figure 2.4. RWM Schematic (left) and Typical Longitudinal Profile (red trace) near 15 Turns (right). Signal Amplitude is with Respect to the Center of the Detector.

2.2.5 Acceleration Scheme. The accelerating structures in the Booster consist of 17 cavity resonators, employing an oscillating field from high-powered tube-amplifiers to achieve common gradients of 20-30 MV/m. Since velocity increase as a function of energy scales as γ^{-3}, at lower energy the decrease in particle transit time over the acceleration structures is significant. In a linear accelerator this problem can be easily circumvented by lengthening the drift spaces sequentially. In a circular accelerator in which particles traverse through many turns, such a luxury is impossible, and maintaining phase with the accelerating particles requires precise timing control of the RF fields. In the Booster, the frequency sweeps between 37 MHz at injection (400 MeV) and 53 MHz at extraction (8 GeV). With the frequencies given, a maximum of 84 bunches comprise the Booster beam.

Ramping of the accelerating gradients following injection is also necessary. Full acceleration after injection is not immediate. Capture of the particles into bunches with 37-MHz structure occurs over a few hundred turns, in which RF-cavity voltage phases are gradually aligned, starting more or less completely out-of-phase. This process, referred to as paraphasing, is done to allow particles from the 200-MHz Linac fields to decohere and adiabatically coalesce into the initial 37-MHz Booster structure. However, such a procedure is itself affected by space charge, with higher-intensity beams more difficult to adiabatically capture, resulting in injection losses further exacerbating the problem of accumulating radiation limits.

The inherent intensity limitations at low energy, coupled with the integrated losses from capture, possible resonances from the space-charge tune shift, beam dilution due to mutual Coulomb repulsion, and electromagnetic reaction with the vacuum chamber necessitate the study of these intensity-dependent effects.

2.3 Introduction to the Booster Simulation Tools

No analytical solutions exist for the motion of particles in arbitrary particle distributions in an accelerator, in particular those subject to space charge forces, so simulations are necessary. Accelerators are complex machines consisting of hundreds of elements, repeating their effects over thousands of turns; although machine elements are designed to provide primarily linear forces, the fields are not purely linear. The self-interaction of the beam is itself nonlinearly dependent on the beam distribution, which, due to both the external elements and these self-forces, is dynamic. A typical beam has 10^{12} to 10^{14} particles, and each has six degrees of freedom. As with many physical systems, certain properties can be extracted from hard analysis, but in the end, simulation is the only route to an accurate description of its evolution. The accelerator simulation package Synergia was employed to obtain this description. We summarize its features in the following section.

2.3.1 The Workings of Synergia. Synergia is a parallel, 3-D particle-tracking code. Its attractive feature is the ability to calculate the six phase-space coordinates of particles under both the influence of external magnetic optics and internal space-charge forces, i.e. the code is capable of fully three-dimensional beam-dynamics modeling [4]. What follows is an overview.

Given an initial set of phase-space variables ζ^i, one can map their evolution into a final set ζ^f via some mapping function M, corresponding to the Hamiltonian H. One can then describe the (phase-space) distribution of the beam, f(ζ,t), which evolves as [98]

$$f(\zeta,t)=f\left(M^{-1}\zeta,t_0\right) \tag{2.18}$$

We now separate the Hamiltonian corresponding to M into an external (magnetic optics) and internal (space-charge) part, namely [98],

$$H=H_{ext}+H_{sc} \tag{2.19}$$

We are motivated to this for two reasons. Foremost, H_{ext} is a very complicated expression about the reference trajectory, expressed usually as a Taylor polynomial. By comparison, H_{sc} is proportional to the scalar potential ϕ governing the particle configuration, namely, the solution to the Poisson equation

$$\nabla^2\phi=-\rho \tag{2.20}$$

Secondly, the space-charge forces, compared to those in the magnetic elements, vary slowly over the longitudinal coordinate. Implementation of this comes in the form of "split operators." Let M_{ext} be the map (Hamiltonian) for the external magnetic elements, and M_{sc} for the internal space-charge forces. If we let our time step[9] be τ, we may write [98]

$$M(\tau) = M_{ext}(\tau/2) M_{sc}(\tau) M_{ext}(\tau/2) \tag{2.21}$$

In other words, within a time step τ we apply a transport of the distribution from M_{ext} halfway through at $\tau/2$, followed by solution of Poisson's equation yielding a space-charge "kick" at τ, and another transport with M_{ext} through the remaining half-step at τ.

The external-optics portion of the Hamiltonian is provided by lattices created in the MAD (Methodological Accelerator Design) accelerator language. MAD has been a well established standard for reproducing the behavior of single-particle, nonlinear optics in accelerator simulations. A fully detailed description of the workings of Synergia is provided elsewhere [4,63,98]. For our purposes, Synergia consists mainly of two components, a Poisson solver tracking macroparticles in the presence of space-charge fields, and a MAD parser creating transport matrices accounting for the external optics specified by the MAD lattice file.

2.3.2 Simulation Benchmarking. Before applying the simulation to our data, it is useful to compare with analytically calculable results related to the work in this writing. In the following sections we present two clear benchmark sets of the simulation, one corresponding to the optics, the other to the beam dynamics.

---

[9] Often in accelerator physics, a longitudinal coordinate plays the role of time.

To verify the linear optics, the focusing strength of the trim quadrupoles and skew quadrupoles are compared to realistic Booster data. For the beam dynamics, the RMS beam size for a KV distribution in a simple repeating FODO[10] cell is compared to analytical results. This test of beam dynamics is perhaps the most suitable since it represents most clearly the collective effects of a charged particle distribution. Another important check is the space-charge algorithm against the Space-charge tune shift for a KV distribution with open boundary conditions. This remains as one of the few available analytic results for space-charge dynamics. Various other benchmarks have been done by the developers [8, 9].

2.3.2.1 Beam Dynamics Tests. For a KV-distributed beam, the RMS beam widths were given in (2.15). Figure 2.5 shows a KV beam with a current of 500 mA[11] in a FODO cell, with representative values of this quantity ε_{RMS}[12] having a value of 3 mm-mrad. Figure 2.6 represents the shift in the particle tune for a KV-distributed, longitudinally uniform beam due to space-charge forces using a simulated Booster lattice.

The tunes are expected, in this case, to behave according to [74]

$$\Delta\nu = \frac{-\Xi r_0}{8\pi\beta^2\gamma^3\varepsilon_{RMS}} \tag{2.22}$$

where Ξ is the number of particles in the beam, r_0 is the classical proton radius, and ε_{RMS}

---

[10] FODO is short for to focusing-drift-defocusing-drift. Quadrupole magnets that focus in one plane defocus in the other. A FODO cell is then a pair of quadrupoles oriented 90 degrees to each other and separated by a drift space.

[11] Beam intensity has been assumed to be the number of particles in the ring, or bunch in some cases. Often this is used interchangeably with current, but this is only valid in the ultrarelativistic case, where longitudinal particle velocity is nearly independent of energy. In general, the current, I, is given by $I=eNf_{rev}$, $f_{rev}=\beta c/C$

[12] Emittance will be discussed more thoroughly in Chapter 3

is this same RMS emittance. Particle positions were sampled 24 times per turn for 100 turns to obtain both the integer and fractional part of the particle tunes. Agreement between simulation and analytical results is quite good, demonstrating that Synergia reliably reproduces the dynamics of the beam due to the self-fields.

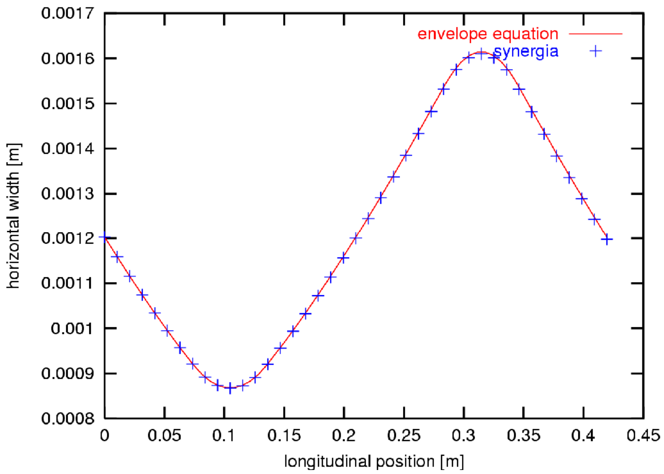

Figure 2.5. Envelope Width at 500-mA Beam Current with KV Distribution. Simulation (blue) is Compared to Analytical Prediction (red).

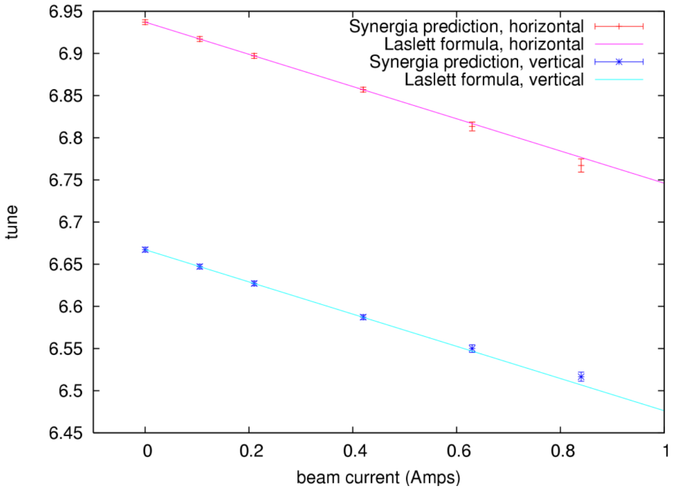

Figure 2.6. Comparison of Horizontal (magenta) and Vertical (blue) Space-Charge Tune Shifts to Simulated Values for Various Intensities[13]

---

[13] Synergia example scripts producing Figures 2.6 and 2.7 were developed by J. Amundson, Computing Division, FNAL.

2.3.2.2 Linear Optics Tests. To test the optics, a realistic Booster lattice with correctly placed trim quadrupoles and skew quadrupoles was used. For a beam with rigidity p⁄e, The tune change due to N quadrupoles at similar locations in a lattice of periodicity N is given by

$$\Delta\nu = \frac{N}{4\pi}\frac{\beta(s)}{p/e}\int_0^L B'dl \tag{2.23}$$

Where β(s) is the local β-function in the relevant plane, and B’ is the field gradient of one of the N quadrupoles. Likewise for the skew-quadrupoles, the shift in the tune is

$$\Delta\nu = 2\phi\frac{N}{4\pi}\frac{\sqrt{\beta_x\beta_y}}{p/e}\int_0^L B'dl \tag{2.24}$$

where φ is the rotation angle of the quadrupole, and $\sqrt{\beta_x\beta_y}$ is the geometric mean of the horizontal and vertical β-functions.

Particle energy in the Booster is given operationally in terms of the kinetic energy, and the simulation follows suit. The rigidity p⁄e can be expressed in terms of the kinetic energy K as

$$\frac{p}{e} = \frac{K}{c}\sqrt{1+2\frac{E_0}{K}} \tag{2.25}$$

where E_0 is the rest energy of the proton. At injection this value is around 954 MeV⁄c.

We now discuss the tune shifts as predicted from Booster parameters. The correction elements sit in the center of the short and long drift sections. Table 2.2 lists the horizontal and vertical β-functions at these drift locations. Here the values are either a maximum or a minimum in the accelerator.

Table 2.2. Horizontal and Vertical Functions at the Centers of the Booster Drift-Space Components

β-functions (m)	Short Section	Long Drift Section
Horizontal	33	6.8
Vertical	4.1	20.5

Our purpose is to compare tune shift dependence on focusing strength given by (2.23-24) with those obtained from a Synergia simulation of the Booster. A magnet will affect the motion of a particle only as strongly as its field or field gradient. Comparing the tune change due to a certain maximal field from an actual trim magnet to a simulated result requires manipulation of these equations, since the particle optics used by the simulation are expressed in terms of focusing strength. In the MAD language, for quadrupole magnets, the focusing power of a quadrupole is determined by the "normalized" field gradient,

$$k = \frac{1}{L}\frac{1}{p/e}\int_0^L B'dl \tag{2.26}$$

where L is the length of the magnet. The length is embedded into the definition to account for the existence of "thin" magnets of zero thickness but finite focusing power. We assume a longitudinally uniform gradient, in which case

$$k = \frac{B'}{p/e} = \frac{1}{fL} \tag{2.27}$$

where f is the focusing strength of the quadrupole given in (2.4).

The tune shifts as a function of focusing strength may thus be written in terms of this normalized gradient as

$$\Delta\nu_{trim} = \left[\frac{N}{4\pi}\beta(s)\right](kL) = C_{trim}(kL) \tag{2.28}$$

$$\Delta \nu_{skew} = \left[2\phi \frac{N}{4\pi} \sqrt{\beta_x \beta_y} \right] (kL) = C_{skew} (kL) \qquad (2.29)$$

The bracketed terms, C_{trim} and C_{skew} then represent the predicted slope of the particle tunes as a function of inverse focal length 1⁄f. Given the listed β-functions in Table 2.2, the slopes are given in Table 2.3.

Our comparison was performed by running Synergia using first-order maps[14], for ten settings in each quadrupole strength. Tunes were obtained from discrete Fourier transform of centroid motion over 1000 turns.

Table 2.3. Numerical Values of Coefficients Corresponding to Correction Elements Obeying (2.26)

Quadrupole	Quad Long	Quad Short	Skew Long	Skew Short
C_H(m)	13	63	35.4	34.9
C_V(m)	39.2	7.83	35.4	34.9

Figure 2.7 shows the result. Slopes of the linear fits are provided in the legend for each corrector element for comparison with Table 2.3. Agreement is good in all cases beyond 5×10^{-5} m^{-1}. Below this value the shift in the frequency spectrum was difficult to resolve simply because with 1000 turns the resolution in tune was limited to 0.001, roughly 100% of the actual shift. Nonetheless points agree faithfully for realistic tune changes. The exception lies in the skew-quadrupole values, which are depressed by a factor of 1⁄√2. This arises from the 45° tilt angle and how it is interpreted in the MAD parser. In any case, it is a consistent multiplier and can be easily compensated.

---

[14] I.e. without considering nonlinear lattice effects (sextupoles, etc).

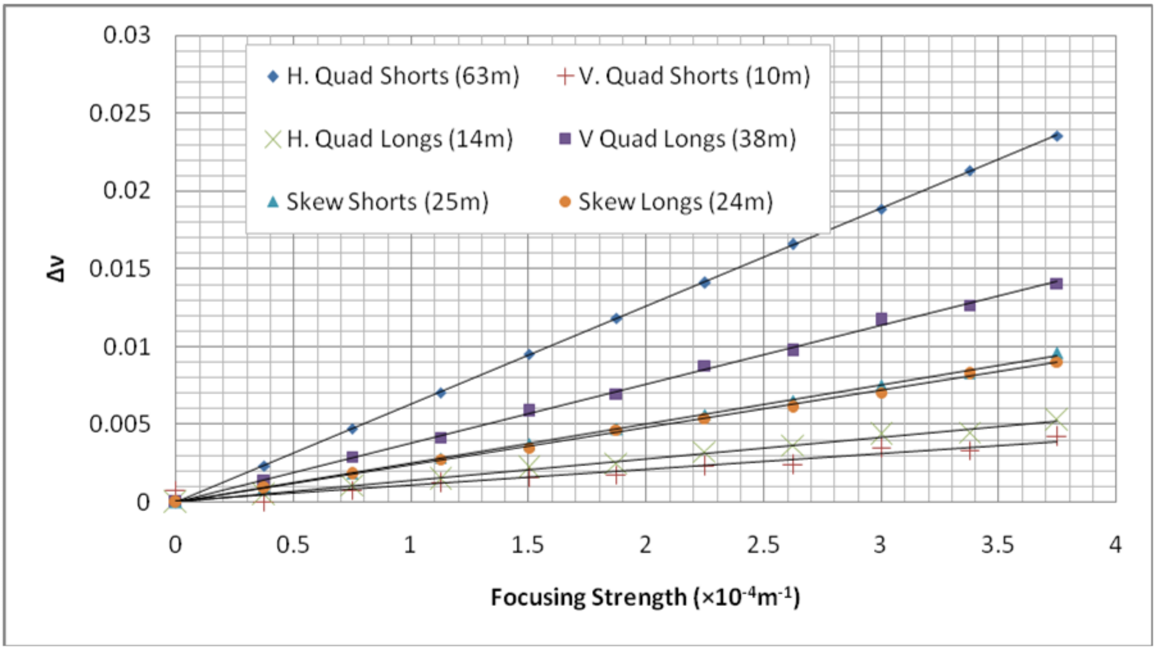

Figure 2.7. Comparison of Calculated vs. Simulated Tune Change under Increasing Strength of Various Corrector Elements. Different Colors Represent Different Corrector Types. Slopes of the Fits are Provided in the Legend.

The results of the simulation will be used whenever possible to corroborate experimental findings throughout this work.

CHAPTER 3

EXPERIMENTAL DETERMINATION OF SIX-DIMENSIONAL EMITTANCE AND BEAM-HALO FRACTION IN THE FERMILAB BOOSTER NEAR INJECTION

3.1 Synopsis

Emittance is a quantity used as a figure of merit to assess quality of a particle beam, representing the phase-space area occupied by the distribution of the particles. We present a method for measuring, with some assumptions, the emittance simultaneously in three dimensions for the horizontal, vertical, and longitudinal planes of motion, from which the product of these (total six-dimensional emittance) can be thus obtained. Techniques for calculating the horizontal and vertical emittance from transverse profile widths are discussed, as well as several longitudinal measurements necessary to obtain simultaneously the longitudinal values. A correction the measurements based on simulation results is then applied, leading to a final value as a function of intensity, whose behavior can be used to pinpoint beam dilution that cannot be as adequately seen through single-plane measurements. The chapter is concluded with a demonstration of a method to characterize the fraction of beam possessing excessive large-amplitude motion, referred to as the beam halo, using existing data and instrumentation. Results will be shown for a wide range of intensities

3.2 Theory of Emittance as a Constant of the Motion in a Beam

The concept of emittance as an invariant in the motion of the particle beam has been present since the theory of Courant and Snyder was developed in 1958 [39]. A terse but complete review of emittance and its various interpretations has been done by Buon [8]. What follows is a brief overview of the concept and its use as a statistical quantity.

Let us consider the simplest case of a single particle with large longitudinal momentum P_z executing transverse oscillatory motion in a circular accelerator with completely linear focusing elements. Let P_x be the transverse momentum component, with $P_x \ll P_z$, and x the particle's transverse position relative to a reference orbit. The slope of the trajectory is then given by $x' = dx/dz = \dot{x}/\dot{z} \approx P_x / P_z$. At some location in the accelerator (some coordinate z along the direction of beam propagation), if we follow the single-particle phase-space coordinates turn after turn, an ellipse in x-x' phase space would eventually be mapped.[15]

At all points in the accelerator, this particle will exhibit similar behavior, tracing out an ellipse in phase space as the coordinates are plotted each time it arrives at that location. The correspondingly mapped ellipse will vary in eccentricity and orientation, but its area will remain constant. This conservation of phase-space area is important, but to adequately be applied to the dynamics of a particle beam, this one-particle, two-dimensional phase-space invariant must be generalized to the case of N particles moving in three directions. The six-dimensional phase-space volume occupied by these particles is connected to a quantity describing the beam called the emittance, and its general invariance is a result of the well-known Liouville Theorem.

Over time the particles will change their positions in configuration and momentum space, and thus correspondingly in the phase space, distorting the shape of the phase-space volume containing the beam. Assuming no particle loss, the total volume remains constant. However, in applications of accelerator physics, this shape distortion is of im-

---

[15] For a rational number, this "ellipse" would be a series of phase-space dots equal in number to the denominator of the fractional part of the tune.

portance, as we shall show.

3.2.1 The Liouville Theorem in Hamiltonian Systems Applied to Accelerators.

The theory of phase-space invariants in Hamiltonian systems has been well established. We briefly review a few points for reference. Let us consider a phase-space particle density n given by

$$n = n(x, y, z, p_x, p_y, p_z, t) \tag{3.1}$$

A number dN of particles in a small phase-space volume dV is then given by

$$dN = n\,dV = n\,dx\,dy\,dz\,dp_x dp_y dp_z \tag{3.2}$$

A phase-space velocity v for each particle exists, where $\vec{v} = \{\dot{q}_i, \dot{p}_i\}$ and the p's and q's are the usual canonical positions and momenta. Since the total number of particles, hence the number of phase-space points, is constant, the continuity equation must be obeyed, i.e.

$$\vec{\nabla} \bullet (n\vec{v}) + \frac{\partial n}{\partial t} = 0 \tag{3.3}$$

We assume a Hamiltonian $H(q_i, p_i, t)$ can be defined for this system, in which case it can be shown that [103]

$$\vec{\nabla} \bullet \vec{v} = \sum_{i=1}^{3} \left(\frac{\partial^2 H}{\partial p_i \partial q_i} - \frac{\partial^2 H}{\partial q_i \partial p_i} \right) = 0 \tag{3.4}$$

Hence

$$\frac{\partial n}{\partial t} + \vec{v} \bullet \vec{\nabla} n = 0 \tag{3.5}$$

The left-hand side of (3.5) is the total time derivative of n, so we may write

$$\frac{dn}{dt} = 0 \Rightarrow n = n_0 = \text{const} \tag{3.6}$$

Hence the phase-space particle density, and correspondingly the volume occupied by a given number of particles in phase space, is a constant of the motion. This result is a representation of the Liouville Theorem applied to Hamiltonian systems. In accelerator language it is closely related to the emittance introduced by Courant and Snyder. This preservation of the phase-space area can be used as a figure of merit representing the quality of the beam. A low-emittance beam is generally desirable, since high particle density is preferred for many experiments. A few caveats are necessary, however. First, from an operational perspective, no standard definition of emittance is consistently used in the literature.[16] More importantly, however, a small phase-space area (i.e. seemingly "low emittance") does not guarantee a high-quality (well-behaved) beam. Two different phase-space distributions of equal area but differing shapes naturally may have very different behaviors, some of which could be beneficial, while others harmful, to stability. In what follows we detail these issues more precisely.

3.2.2 Trace-Space Emittance. One can express in one plane the area in x-x′ space occupied by the particles at a location in the accelerator. As in the single-particle case, for an ensemble of particles at z, the area occupied by the points corresponding to all particles in the beam in this plane can be expressed (somewhat loosely) as

$$A_x = \oint\!\!\oint_{periphery} dxdx' \tag{3.7}$$

This experimentally is referred to as the emittance. The area in this x-x′ space, however, does not necessarily correspond to phase space occupied by the particles, whose motion

---

[16] In fact, a plurality of definitions exist both in conventions for numerical factors as well as in conceptual interpretation.

in a Hamiltonian system is bounded by some constraints and in general is in some way correlated. A snapshot of the area occupied in this x-x′ space may not account for this. A very distorted shape has different correlations than a smooth elliptical one, for example. The area of this space is not precisely that of phase space but rather what is referred to as trace space [102] for reasons that will be evident shortly.

3.2.3 Statistical Definition of Emittance. The single-particle emittance is, of course meaningless since the quantity is intended to assess a property of the whole beam. However, many particles trace many of these ellipses of varying areas as they traverse some location (longitudinally) in the accelerator turn by turn. No one phase-space trajectory, large or small, is thus representative of the distribution. RMS quantities then become important, and the emittance can be defined statistically in terms of the RMS widths. As long as the particle motion between planes is uncoupled, one can consider an emittance associated with each direction independently. Considering motion in one dimension, say, the x-direction, the first moments (RMS widths) of the distribution may be expressed as σ_{xx}, $\sigma_{x'x'}$, $\sigma_{x'x}$, and $\sigma_{xx'}$. The first two are the position and momentum widths, while the last two are the cross-correlations (covariant widths), and are usually equal for realistic distributions. For completely uncorrelated motion, the emittance may be defined as the product of the position and momentum width.

$$\varepsilon = \sigma_{xx}\sigma_{x'x'} \tag{3.8}$$

Otherwise,

$$\varepsilon = \sigma_{xx}\sigma_{x'x'} - \sigma_{x'x}^{2} = \det\begin{pmatrix} \sigma_{xx} & \sigma_{x'x} \\ \sigma_{xx'} & \sigma_{x'x'} \end{pmatrix} \tag{3.9}$$

where the bracketed term in (3.9) is the covariance matrix of the beam distribution in one dimension. This definition represents, statistically, the RMS phase-space area of the beam, accounting additionally for the shape of the distribution in x-x′ space. While the determinant of this covariance matrix is the RMS emittance in one dimension, the diagonal product of this matrix represents the RMS area analogous to what was expressed in (3.7). This quantity is sometimes called the RMS "trace-space" emittance.

3.2.3.1 The Six-Dimensional Covariance Matrix. Emittance is of course not limited to two-dimensional quantities in the three separate planes. While horizontal, vertical, and longitudinal emittance individually represent constants of the motion in an uncoupled, linear system, in general it is possible for emittance to be exchanged among the planes of motion, most commonly between the horizontal and vertical. In general, a statistically defined emittance including all correlations can be obtained from the 6×6 covariance matrix as follows.

$$C = \begin{pmatrix} \sigma_{xx} & \sigma_{x'x} & \sigma_{yx} & \sigma_{y'x} & \sigma_{zx} & \sigma_{z'x} \\ \sigma_{xx'} & \sigma_{x'x'} & \sigma_{yx'} & \sigma_{y'x'} & \sigma_{zx'} & \sigma_{z'x'} \\ \sigma_{xy} & \sigma_{x'y} & \sigma_{yy} & \sigma_{y'y} & \sigma_{zy} & \sigma_{z'y} \\ \sigma_{xy'} & \sigma_{x'y'} & \sigma_{yy'} & \sigma_{y'y'} & \sigma_{zy'} & \sigma_{z'y'} \\ \sigma_{xz} & \sigma_{x'z} & \sigma_{yz} & \sigma_{y'z} & \sigma_{zz} & \sigma_{z'z} \\ \sigma_{xz'} & \sigma_{x'z'} & \sigma_{yz'} & \sigma_{y'z'} & \sigma_{zz'} & \sigma_{z'z'} \end{pmatrix} \tag{3.10}$$

The product of the diagonal elements of C is the six-dimensional trace-space emittance[17], while the determinant is the fully correlated representation. The variables z and z' are somewhat ambiguous because the longitudinal motion can be expressed in terms of several types of conjugate pairs. Momentum error and longitudinal distance from synchron-

---

[17] Such a term is actually a misnomer, because the trace is the sum of the diagonal elements, not the product.

ous particle (e.g. in units of nm) or synchronous-particle energy difference and longitudinal phase angle (e.g. degree-MeV) are used frequently in analytical work and simulation. Another common pair of quantities, used experimentally, is the energy difference and bunch width measured in transit time (e.g. eV-sec).

3.2.3.2 RMS Emittances and Conventions. In actual measurement, RMS quantities depend strongly on the distribution. For most purposes, emittance is obtained experimentally using the assumption of essentially Gaussian distributions. In such cases no distinct edge of the beam exists, and one must consider a region of phase space in which a representative fraction of particles reside. While many different conventions exist regarding what is "representative," the most commonly employed is the so-called "95%" emittance, in which such an area in phase space contains, statistically, around 95% of the particles within its periphery at any instant[18]. For a Gaussian beam (in width and momentum), $\varepsilon_{95\%} = 6\varepsilon_{RMS}$. ε_{RMS} is what is measured usually, and $\varepsilon_{95\%}$ is what is reported as the representative figure of merit of the beam. In general, the fraction, m, of particles contained within some multiple n of ε_{RMS} is given by [83]

$$m = 1 - e^{-n/2} \tag{3.11}$$

The 95% convention is most useful for discussing emittance in the transverse plane, because the transverse oscillation amplitude is what is limited by the machine aperture, and having 95% of the particles well within its limits is considered good measure for practical design consideration. In the longitudinal plane the incentive to use such a

---

[18] For unbounded motion, 100% of the particles would not be enclosed in any finite region of phase space.

convention is far less strong, the reasons for which shall be outlined in section 3.3.2. Longitudinal values often are simply given as ε_{RMS}.

3.2.3.3 Emittance under Acceleration. The given descriptions of emittance so far are only valid for a coasting beam. It is well known that beam width and relative momentum spread decrease as a function of energy for relativistic particles. These are relativistic-geometric effects. Emittance as defined cannot be preserved for differing energies. One corrects for this with the so-called normalized emittance,

$$\varepsilon_N = \beta\gamma\varepsilon \tag{3.12}$$

The normalized emittance is preserved under acceleration, and is thus typically the quantity quoted in the literature.

3.3 Experimental Determination of the Emittance

It is desirable to have a simultaneous emittance measurement in the Booster to separate the presence of emittance exchange from that of emittance growth. For an uncoupled, linear lattice with no space-charge effects we expect the emittance to be constant in each plane. In the presence of coupling and/or space charge this will no longer be the case.

Emittance is, loosely speaking, a measure of the spread in energy and position of the particle distribution in a particular plane of motion. Since energy can be exchanged between the planes by one method or another, individual measurements are insufficient to obtain an adequate picture. A simultaneous measurement, in which the total emittance is taken to be the product of the three measured emittances, should remove these interchanges and can be used, in principle, to indicate the presence and rate of emittance growth.

Based on available instrumentation in the Booster, an indirect measurement of the emittance can be made using a few assumptions. The transverse beam size measurements may be performed using IPM data, while the longitudinal beam size may be obtained from the RWM. The assumptions, expressions, and techniques leading to these measurements are detailed in the following subsections.

3.3.1 Obtaining Transverse Measurements. In the transverse plane the beam width may be measured from the IPM, but its momentum width cannot be directly determined simultaneously. However, if we assume that the shape of the distribution is governed by the β-function, the position width is sufficient. In this case the horizontal and vertical emittances may be expressed, using the notation above, as

$$\varepsilon_x = \frac{\sigma_{xx}^2 - D^2\sigma_{z'z'}^2}{\beta_x} \tag{3.13}$$

$$\varepsilon_y = \frac{\sigma_{yy}^2}{\beta_y} \tag{3.14}$$

The second term in the horizontal plane corrects for the momentum dispersion. Particles with differing momenta will naturally have differing positions because their orbit radii will be affected. This effect complicates the dynamics of the horizontal beam size but its associated displacement is unrelated to the horizontal oscillation. The dispersion function, D, determines how much of an influence this effect has at a particular accelerator location. The relative momentum error, $\sigma_{z'z'}$ is naturally energy-dependent and can be expressed as

$$\sigma_{z'z'} = \sigma_{(z'z')_0}\sqrt{\frac{\gamma_0^2 - 1}{\gamma^2 - 1}} \tag{3.15}$$

where the initial momentum width $\sigma_{(z'z')0}$ has been separately determined.

Assuming a Gaussian-distributed beam, IPM widths were obtained through a fitting algorithm fitting the IPM data to a Gaussian distribution with a linear term [133]. IPM data are somewhat noisy turn by turn, but since we are interested in the overall features over hundreds of turns, the data were smoothed with a 250-points low-pass filter, with a frequency cutoff of 1⁄100 turns (i.e 1⁄100 samples, once per turn). A typical profile width, along with its filtered counterpart, is shown in Figure 3.1. Data are shown through the first 3000 turns in the cycle, where the kinetic energy increases from 400 MeV to around 1.5 GeV. A decrease in width can be observed due to this acceleration.

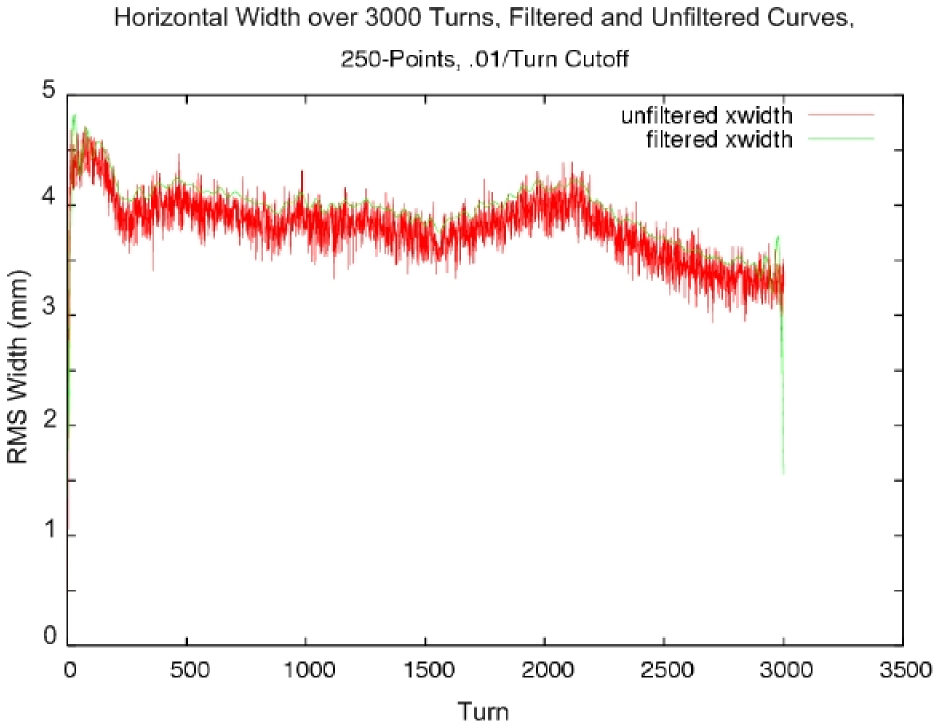

Figure 3.1. Sample Filtered (green) and Unfiltered (red) Horizontal Width over 3000 Turns for 3 Turns of Injected Beam

Data in Figure 3.1 also showcase the filtering procedure (smoothed, green curve above the red data). With the width given turn-by-turn, as well as knowledge of the momentum dispersion and β-functions at the IPM location, the transverse emittance can be calculated from (3.13-14). For example, at the IPM in the Booster, the horizontal β-function is 6.5 m, the dispersion function is 1.8 m, and Δp/p is around 10^{-4}. Using (3.12), at 400 MeV, β = 0.71 and γ = 1.4. Given the profile width above, a normalized value of 1.2π mm-mrad[19] is found. The normalized, 95% emittance is then 7.2π mm-mrad at injection. Typical values are often around 12π mm-mrad at nominal intensities in both transverse planes [131], so for this case where intensity was less than half this value, our calculations give consistent results. The full details of these transverse emittance calculations for a wide range of intensities will be given in section 3.4.

3.3.2 Obtaining Longitudinal measurements. Calculating longitudinal emittance from the corresponding longitudinal quantities is considerably more involved. In the longitudinal plane, RF fields are responsible for accelerating the particles, and for keeping them within a certain phase range relative to the synchronous particle. The evolution of this particle phase and energy are given by the set of dynamical equations [81]

$$\frac{d}{dt}\left(\frac{\Delta E}{\omega_{RF}}\right)=\frac{1}{2\pi}eV\left(\sin\phi-\sin\phi_s\right) \tag{3.16}$$

$$\dot{\phi}=\frac{h\omega_{RF}^2\eta}{\beta^2 E}\frac{\Delta E}{\omega_{RF}} \tag{3.17}$$

where V is the accelerating voltage, ΔE is the energy gain, E is the synchronous particle energy, η is the machine “slip factor,” (discussed in the following section) and ω_{RF} is the

---

[19] Because transverse phase space has position and angle (measured typically in radians) as the dynamical variables, the factor of π is often extracted from the numerical value and expressed explicitly (yet another convention to add to the emittance description).

RF angular frequency. ϕ_s is the "synchronous phase," essentially the location on the accelerating RF wave along which the synchronous particle traverses. The motion of the particles in the longitudinal plane is thus intrinsically nonlinear, and this sinusoidal dependence leads to a phase-space boundary between bounded and unbounded motion (commonly referred to as the separatrix[20]). In accelerator language the area enclosed by this separatrix is referred to as a “bucket.” The shape and size of the separatrix depends on the synchronous phase in a nontrivial way. Our aim is to calculate the longitudinal emittance for an unaccelerated bucket first, and then apply the correction due to acceleration.

3.3.2.1 Stationary Bucket Area and RMS Longitudinal Emittance. When the beam is not accelerating, calculation of the longitudinal emittance can be obtained from the measurement of longitudinal bunch width, and knowledge of the bucket area. The assumption is made that the phase-space area of the beam maintains the same shape as that of the bucket containing it, and that the changing shape of the bucket under acceleration occurs slowly enough that the beam continues to maintain this shape. It can be shown that the bucket area, and thus RMS longitudinal emittance, $\varepsilon_{L,rms}$ are given by [60, 82]

$$A_B = 16\left(\frac{R_{path}}{hc}\right)\sqrt{\frac{eV_{RF}E_T}{2\pi h|\eta|}} \tag{3.18}$$

$$\varepsilon_{L,rms} = \sqrt{\frac{\beta^2 \pi e V_{RF}\omega_{RF}^2 E_T}{2h|\eta|}}\sigma_\tau^2 \tag{3.19}$$

respectively, where R_{path} is the accelerator radius, σ_τ is the longitudinal RMS bunch width (in transit time), βc is the relativistic velocity, V_{RF} is the accelerating voltage, E_T is the

---

[20] It is, of course, the separatrix for the motion of a simple pendulum in particular, and belongs to a general class of such separatrices for elliptic functions in dynamics.

total particle energy, h is the harmonic number, ω_{RF} is the accelerating RF angular frequency, and η is the so-called 'slip factor,' given by [49]

$$\eta = \frac{1}{\gamma^2} - \frac{1}{\gamma_T^2} \tag{3.20}$$

where γ_{T} is a machine-specific parameter, and γ is the familiar Lorentz boost. The location in the cycle where $\gamma = \gamma_{\mathrm{T}}$ is called the "transition." Near this transition, where $\eta \rightarrow 0$ these expressions are singular and must be dealt with in an analytically graceful manner. Far from this point, however, they are valid. For the Booster the value of γ_{T} is 5.45. Near injection, the particles have a total energy of about 1.33 GeV, with γ being 1.4, and η 0.4765. The RF voltage is around 900 kV, with a frequency of 37 MHz, and $\beta^2 = 0.5$. We obtain a value of 0.10 eV-s for the bucket area with these values. Nominal values of the bucket area (i.e. typical total longitudinal phase space area available for one bunch) for Booster are acceptably more or less in this range (0.08-0.10 eV-s) near injection [93], where this expression is valid.

To calculate emittance, the total (synchronous) particle energy is needed. Calculation of the energy gain per turn would properly require knowledge of the RF synchronous phase, but to minimize the number of parameters needed for calculation we know the RF frequency is a harmonic of the revolution frequency (with a value of 84 in Booster). Given the orbit circumference, C, we then can obtain β, γ, and E_{T} in terms of f_{RF}. The emittance is then given, after a little algebra, by

$$\varepsilon_L = \frac{2\pi C f^2}{hc}\sqrt{\frac{\pi}{2}}\sqrt{eVE_{\mathrm{R}}}\sqrt{\frac{1}{\left|\frac{\gamma_T^2-1}{\gamma_T^2}-\left(\frac{Cf}{hc}\right)^2\right|}}\sqrt[4]{\frac{1}{1-\left(\frac{Cf}{hc}\right)^2}}\sigma_\tau^2 \tag{3.21}$$

where h is the harmonic number, c is the speed of light, and E_{R} is the rest energy of the particle. Still, (3.21) is valid only when the particle is not accelerating. We must now correct for the fact that in general the bucket (and hence the beam) is of a different configuration at the onset of acceleration.

3.3.2.2 Running-Bucket Correction Factor. The synchronous particle will receive an energy increment from the RF field. The strength of this increment depends on its arrival relative to the RF phase, ϕ_S. At $\phi_S = 90°$ we obtain maximal acceleration, but beam longitudinal stability is compromised, since particles with phases below this value will (for a sinusoidal accelerating potential) continually fall further behind. At 0° we achieve maximal phase stability but no acceleration. ϕ_S is thus an intermediate value, and in some accelerators it is changed during the acceleration cycle to adjust for changes in machine or beam conditions. In order to adjust the bucket size from that of a stationary (non-accelerating) bucket, an emittance correction factor α(s) [84] is introduced, defined to be the ratio of the accelerating bucket area to the area of an unaccelerated bucket[21].

$$\alpha(\phi_s) = \frac{1}{2\sqrt{2}} \int_{\psi_u}^{\pi-\psi_u} -\operatorname{sgn}(\eta)\sqrt{\left[\cos\psi + \cos\phi_s - \left(\pi - \psi - \phi_s\right)\sin(\phi_s)\right]}d\psi \tag{3.22}$$

Where

$$\cos\psi_u + \psi_u \sin\phi_s = -\cos\phi_s + \left(\pi - \phi_s\right)\sin\phi_s \tag{3.23}$$

The quantity ψ_u represents location of the "unstable fixed point" in phase space. Its interpretation can best be seen from Figure 3.2. ψ_u and π-ψ_u are located on the intersection of the horizontal axis and the separatrix. For $\phi_S = 0$ the bucket area is maximized, but of

---

[21] We assume, of course, that the phase-space distribution of the beam maintains a similar shape to the bucket area.

course, particles receive no acceleration. For larger values of the synchronous phase (to 90°) the bucket area shrinks between these two limits, providing smaller regions of phase stability.

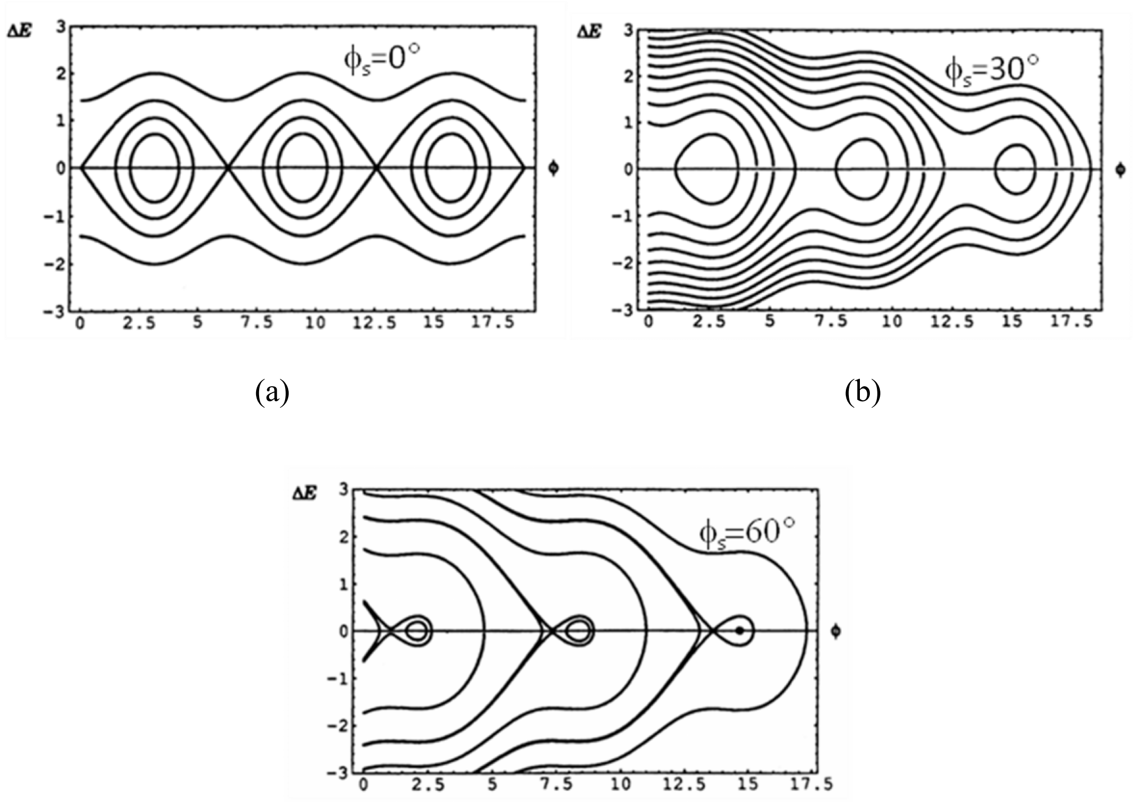

(a) (b)

(c)

Figure 3.2. Phase-Space Portrait for Bucket Area under Various Acceleration Phases, (a) No Acceleration, (b) $\phi_s = 30°$, (c) $\phi_s = 60°$. (plots courtesy D.A. Edwards and M.J. Syphers, 'An Introduction to the Physics of High Energy Accelerators,' John Wiley & Sons, 1993, p.40)

The ratio of the running-bucket to stationary bucket area obtained by (3.22-23) numerically is plotted in Figure 3.3, along with a useful approximate value to it to facilitate calculation, given by

$$\alpha(\phi_s) \approx \frac{1-\sin\phi_s}{1+\sin\phi_s} \tag{3.24}$$

The error in the approximation is usually negligible, with a maximum of 7.5% for ϕ_s near 20°.

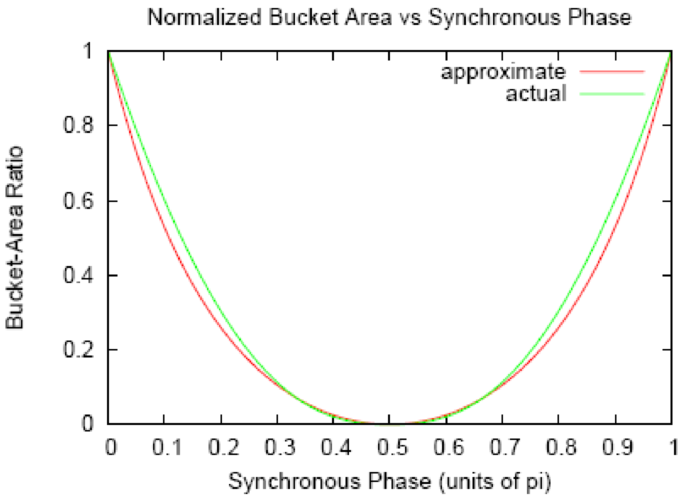

Figure 3.3. Approximate (red) and Actual (green) Ratios of Accelerated Bucket to Stationary Bucket as a Function of Synchronous Phase.

In addition, longitudinal emittance is affected by energy increase in the same manner as the transverse. Thus, the corrected, normalized, under-acceleration emittance in the longitudinal plane is given by

$$\varepsilon_{L,n,a} = \alpha\beta\gamma\varepsilon_L \tag{3.25}$$

where ε_L is the previous emittance given for a stationary bucket.

3.3.2.3 Tracking of Bunch Width, RF Frequency, and Accelerating Voltage. Measurement of the longitudinal emittance requires simultaneous tracking of the RF voltage and RF frequency in addition to the longitudinal width and synchronous phase, which also vary over the cycle. To accomplish this a 20-Gsample oscilloscope (Tektronix DPO7054) capable of obtaining these values with sufficient resolution over 4000 turns was used. Bunch width was obtained on-the-fly using a fitting routine through a Labview$^{\mathrm{TM}}$ interface from the scope's front-end PC controller [118]. RF frequency and voltage, as well as the synchronous phase, were also obtained simultaneously from four separate channels. All data were retrievable from the FNAL ACNET console via application on page W27 [119], which reports and stores these values according to a specified timeline event, in this case to event $17, typically signaling a Booster study-cycle event. Maximal time resolution was every ten turns of the Booster cycle. Figure 3.4 shows typical curves for RF frequency and voltage. In Figure 3.5 the synchronous phase (in radians) and calculated bucket correction are provided.

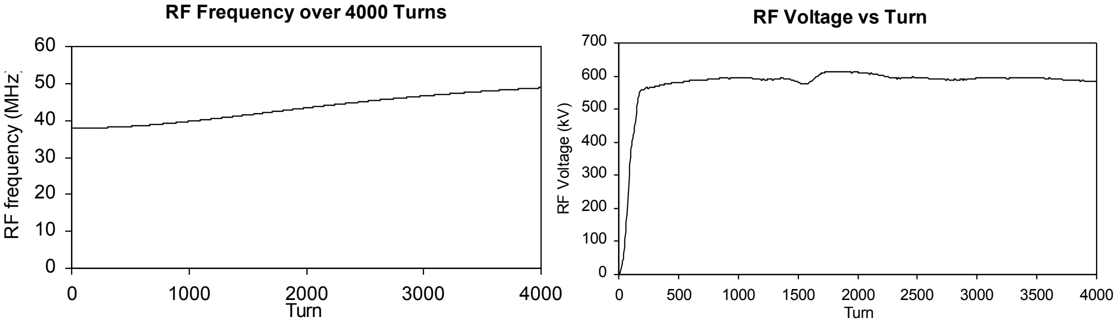

(a) (b)

Figure 3.4. (a) RF frequency and (b) Accelerating Voltage over 4000 Turns for a Typical Booster Cycle

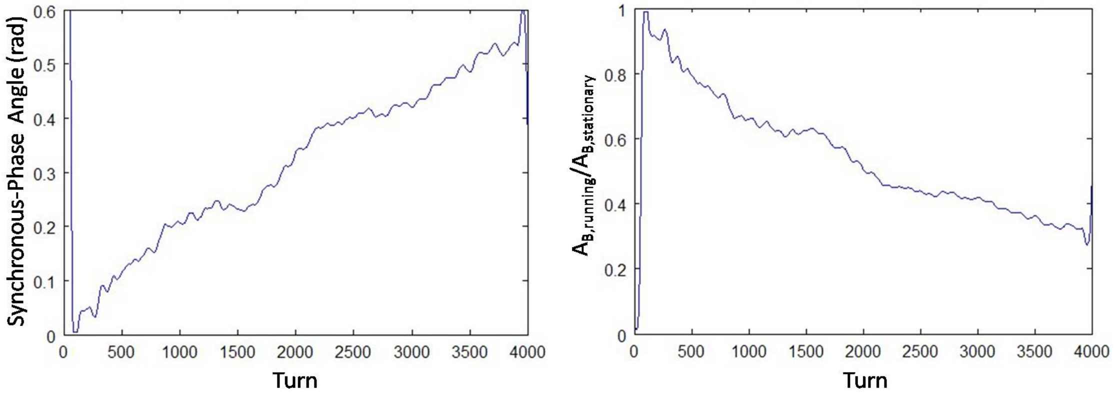

(a) (b)

Figure 3.5. (a) Synchronous Phase and (b) Bucket Area Correction Factor over 4000 Turns

The quantities in Figures 3.4 and 3.5 are typically independent of intensity. Figure 3.6 shows a typical longitudinal bunch width (1σ) for 3.5×10^{12} particles, or seven turns of injected beam. The shrinkage over 4000 turns is a consequence of the acceleration, just as it is in the transverse plane.

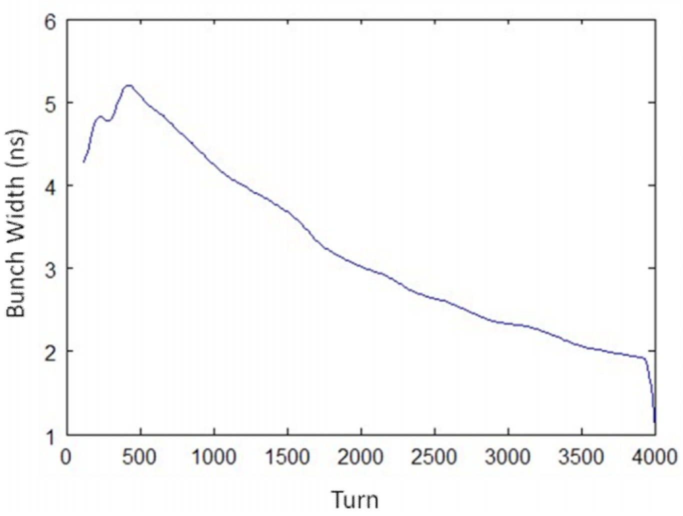

Figure 3.6. Typical Bunch Length (1σ) from RWM Data to W27 Console Application

At injection, given the parameters listed for the bucket area and the figures above, one obtains a typical value of 0.3 eV-sec for the Booster beam (all 84 bunches). Quoted values are around 0.25 eV-sec [131], in keeping with this value. In the longitudinal plane, these refer to ε_{RMS} itself (39% of the particles), not the typical 95% emittance or $6\varepsilon_{RMS}$.

3.4 Procedure for a Simultaneous Measurement

In order to obtain measurements of longitudinal and transverse widths simultaneously, the RWM and IPM were triggered on the same timeline event ($17), beginning from injection, and recorded on the RWM up to 4000 turns (400 data points on the W27 program). The trigger at injection for both RWM and the IPM was set to a typical value of 2ms following the $17 clock event to allow the instrumentation ample time to respond. IPM and RWM measurements were synchronized to begin data-taking on turn 1, but while the IPM was capable of obtaining profile widths turn-by-turn, the ten-turn resolution of the interface to the RWM required interpolation over this interval. Adequate time (roughly one minute) between events was given for manual writing of these data to file. Intensity was varied from 1.5 to 5×10^{12} particles per pulse (three to ten turns of injected beam). Five data sets were taken for each intensity. Profile widths and bunch lengths were averaged over these five sets. Intensity curves were seen not to vary significantly.

3.4.1 Profile Widths over Increasing Intensity. The horizontal, vertical, and longitudinal widths for the above intensities are shown in Figures 3.7 and 3.8. Corresponding intensities are also given. Data in the transverse plane has been filtered using the same cutoff and sampling features as in Figure 3.1. Longitudinal data have also been smoothed slightly with a 20-points filter and a frequency cutoff of 1⁄20 turns. Coloring scheme is provided in the legend of each figure.

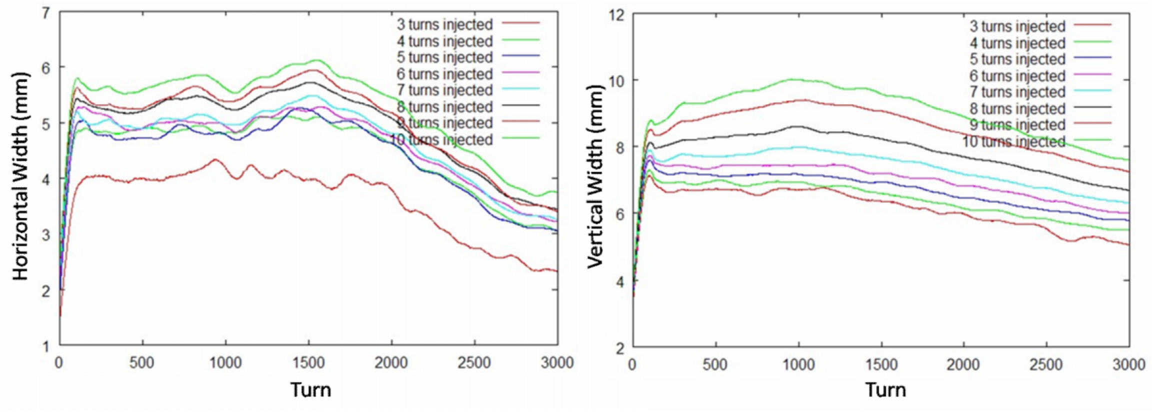

(a) (b)

Figure 3.7. Smoothed Horizontal (a) and Vertical (b) Profile Widths from IPM Fitting for Various Intensities over 3000 Turns. Coloring Specified by Legend.

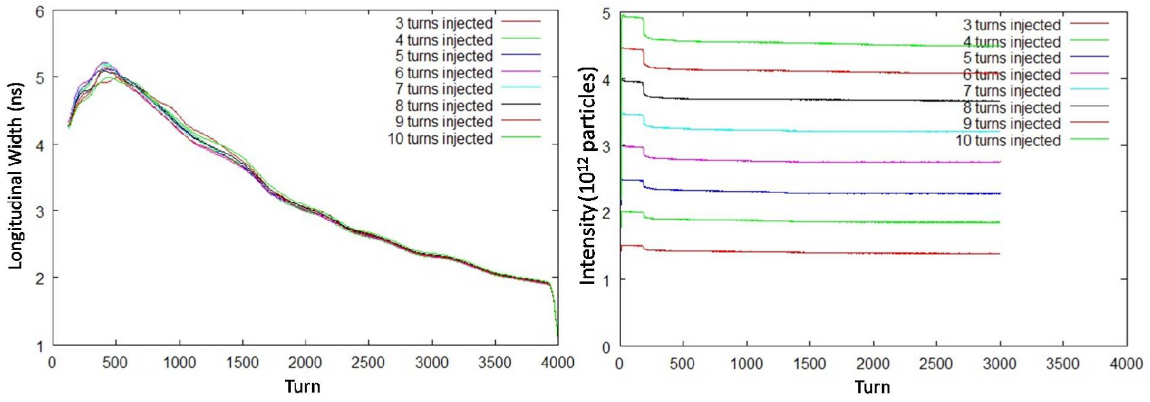

(a) (b)

Figure 3.8. Fitted Longitudinal Width from RWM Response (a) and Corresponding Intensities (b) over 4000 Turns. Coloring by Intensity Specified by Legend.

Notably the data in the longitudinal plane reveal little change in the bunch length as a function of intensity for the range recorded. A dip in the intensities at 250 turns is the effect of the notcher, a device designed to remove a section of the beam for diagnostic purposes near acceleration, which was left operational during the measurement.

3.4.2 Transverse, Longitudinal, and Total Emittance, Experimentally Obtained.

Necessary parameters for obtaining the transverse emittance curves from (3.13-14) are given in Table 3.1

Table 3.1. Booster β-Functions, Dispersion at IPM Location, and Momentum Spread Near Injection

β_x at IPM location	6.5 m
B_y at IPM location	20.5 m
Dispersion (D) at IPM	1.8 m
$\Delta p/p$ at Injection	10^{-4}

To properly normalize the emittance, the quantity βγ must be known throughout the cycle. Acceleration in the Booster is not always constant turn by turn, however, so its value must be obtained otherwise. Operationally, knowledge of the RF frequency, f, is usually sufficient, since the revolution frequency of the synchronous particle is simply the RF frequency divided by the harmonic number. In such case,

$$\beta\gamma = \left[\left(\frac{ch}{Cf} \right)^2 - 1 \right]^{-1/2} \tag{3.26}$$

where h is the harmonic number, c is the speed of light, and C is the orbit circumference. The evolution of this quantity over the first 4000 turns is given in Figure 3.9.

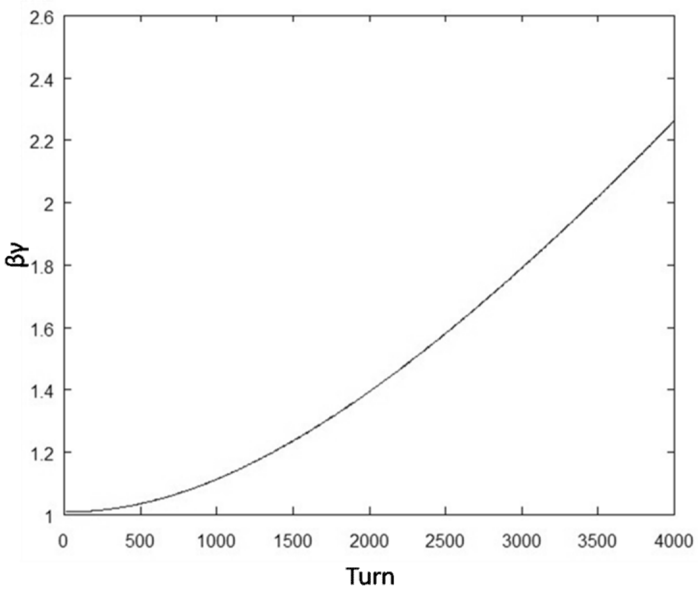

Figure 3.9. Behavior of βγ over the First 4000 Turns in the Cycle

Emittances in the three planes, using filtered horizontal and longitudinal widths and along with their corresponding intensities are shown in Figures 3.10-13. Correction for dispersion is performed in the horizontal plane given the values of Δp⁄p and D in Table 3.1, and (3.15). As (3.15) shows, this correction becomes less important at higher energies. For nominal intensities of 5×10^{12} particles (ten injected turns from the Linac), the horizontal and vertical emittances (1σ) calculated with these parameters in Table 3.1 and Figure 3.7 are expected to be roughly 1.7π mm-mrad in both planes. The 95% emittances, then, would be 10π mm-mrad and 10π mm-mrad. Typical values for this intensity are known to lie in this range [131], providing confidence in the measurement and our assumptions leading to these calculations. Horizontal and vertical RMS (95%) emittances in over the first 3000 turns are given in Figure 3.10.

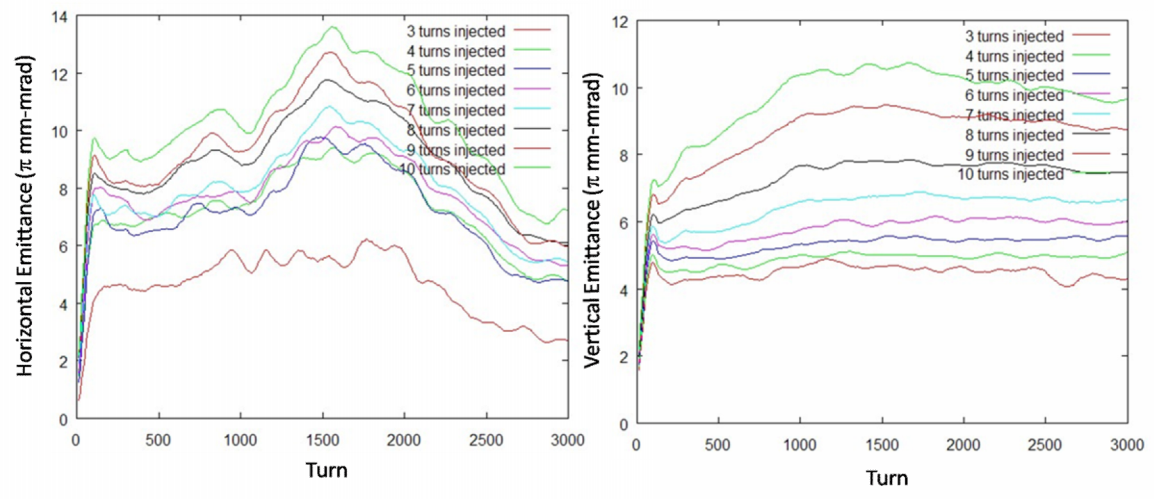

(a) (b)

Figure 3.10. Horizontal (a) and Vertical (b) 95% RMS Emittances over 3000 Turns for Various Intensities from 1.5×10^{12} to 5×10^{12} Particles. Different Intensities are Colored According to the Legend.

The longitudinal emittance calculated from the parameters in (3.25) is shown in Figure 3.11. The 95% convention was not applied to the longitudinal plane, since the comparative numbers did not utilize this either. A value of 0.25-0.35 eV-sec was observed, in keeping with typical Booster values between 0.25-0.40 eV-sec [93,131].

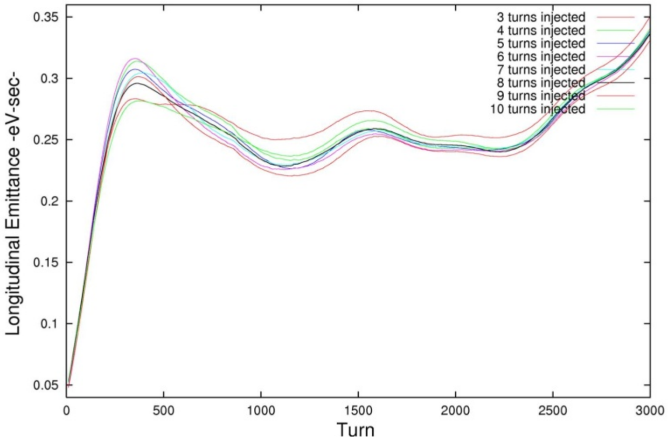

Figure 3.11 Longitudinal RMS Emittance over 3000 Turns for Various Intensities from 1.5×10^{12} to 5×10^{12} Particles. Different Intensities are Colored According to the Legend.

The horizontal plane exhibits a large growth starting at 1000 turns followed by a decrease after 1500. The vertical plane does not show such dramatic behavior, meaning emittance is not exchanged between these planes to sufficiently explain this. In general, emittance can grow because of certain nonlinear effects (e.g. space charge) during operation, but excluding particle loss, emittance cannot decrease. As seen in Figure 3.8b, aside from the notch at 250 turns, particle loss was ruled out. The longitudinal plane shows some commensurate oscillation but significant coupling between the transverse and longitudinal planes is seldom present because of the large difference in energy scales. The total, six-dimensional emittance is given experimentally as the product of the three measured emittances,

$$\varepsilon = \beta^3\gamma^3\varepsilon_L\varepsilon_x\varepsilon_y \tag{3.27}$$

In Figure 3.12 the total emittance is plotted. We notice the bump around turn 1500, with the longitudinal plane taken into account, does not vanish. It is unlikely that the emittance is varying to this degree, especially since emittance cannot diminish without a loss of particles. This behavior reflects a likelihood of an instability affecting the beam's Gaussian shape. Looking at the horizontal plane, we see a curious behavior in the horizontal beam profile, illustrated in Figure 3.13.

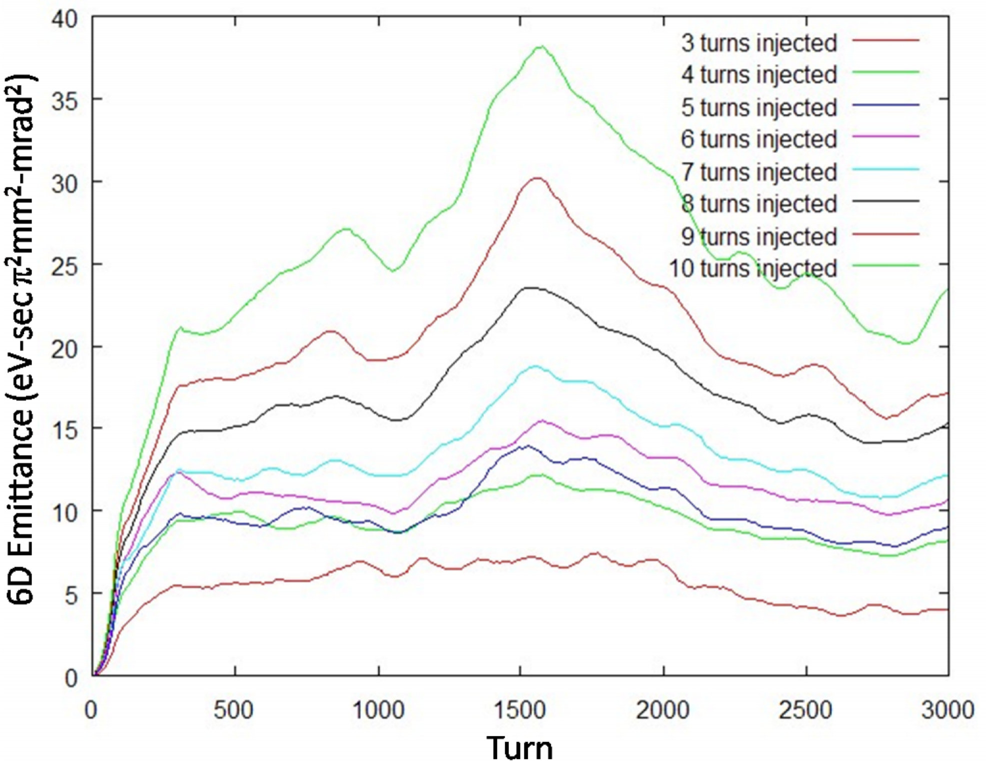

Figure 3.12. Total Emittance as the Product of the three Emittances over 3000 turns for Various Intensities from 1.5×10^{12} to 5×10^{12} Particles. Different Intensities are Colored According to the Legend.

The first curve, 500 turns into the cycle, shows a Gaussian distribution with a shoulder. The second, at 1500, demonstrates an approximately bimodal shape. The third, after 3000, shows that the beam has returned to a more Gaussian form. The existence of this bimodal shape is not accounted for in the fitting routine, and the width is thus exaggerated, leading to a false emittance-growth peak.

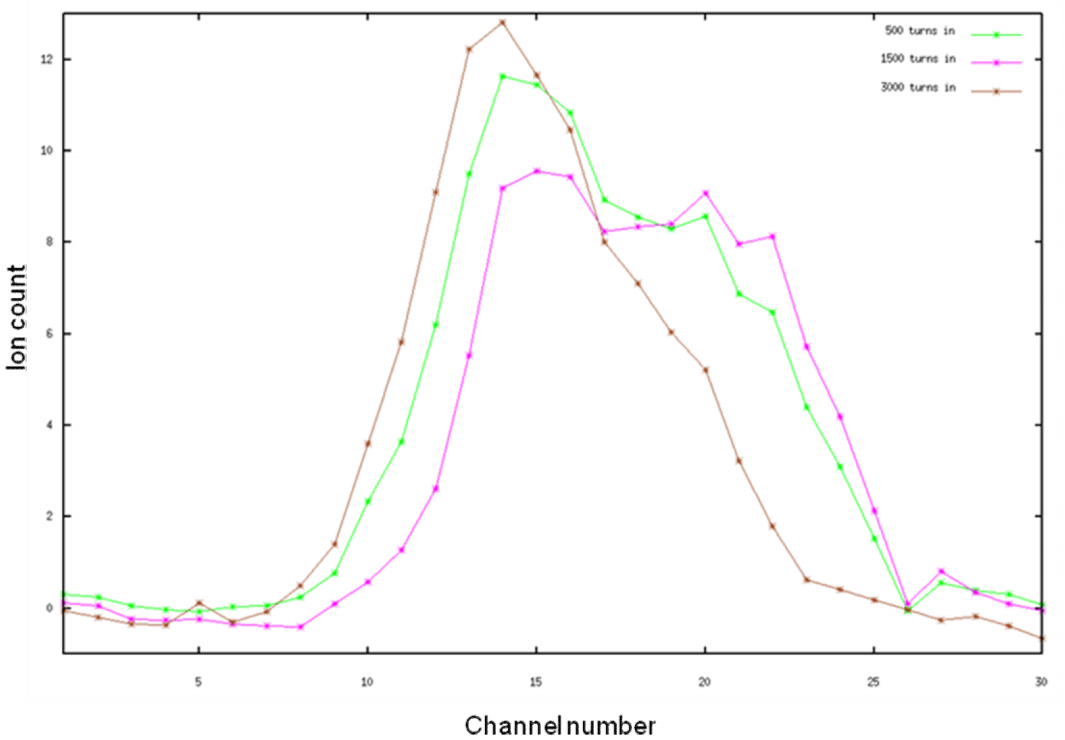

Figure 3.13. Characteristic Horizontal IPM Profiles for an Intensity of 5×10^{12} Particles at 500 (green), 1500 (magenta), and 2500 (brown) Turns

This method, then, is naturally inadequate for poorly behaved (i.e. highly non-Gaussian) beams. However, for relatively well-behaved beams, one can get a good sense of where emittance is growing and where it is being exchanged (i.e. coupling). Furthermore, in the absence of particle loss, this method has the indirect collateral benefit, as shown above, of indicating beam instability wherein the normal Gaussian distribution is significantly distorted.

3.4.3 Correction for Correlation Terms. Total RMS emittance was given by the determinant of the covariance matrix in (3.10). While a simultaneous measurement in the three planes provides a much better picture than independent ones, the correlations are unaccounted for with the measuring techniques presented. In principle, the product of the three measured emittances would be the total emittance for completely uncorrelated motion, among the planes. Here the simulation can be used synergistically[22] to determine the relative importance of these effects. The calculation of emittance in Synergia was done for an elliptical Gaussian beam of 4 mm in size with initial RMS horizontal and vertical emittances of 3 mm-mrad. The longitudinal emittance for the beam was 0.1°-MeV, a somewhat peculiar unit carried over from the development of the IMPACT portion of the software [96, 97]. The effect of bunching was not considered, however, so longitudinal correlations were expected to be minimal in any case.

A typical simulated Booster lattice was used[23], taking into account second-order mapping, in which nonlinear space-charge effects were considered. No random gradient errors were introduced, however, nor were any nonlinear elements of the lattice (e.g. sextupoles, octupoles) activated. A range of intensities from 0 to 14 turns injected was used. Figure 3.14 juxtaposes the full 6D emittance (given by "a" in the legend) to the product of the three uncorrelated emittances (given by "p").

The "correlation excess," ϑ, can thus be defined by taking full determinant of the covariance matrix (3.10) and subtracting off the portion corresponding to the uncorrelated components, which is the product of the body-diagonal elements, to which we refer as Dp(C). Therefore,

$$\vartheta = \det(C) - \mathrm{Dp}(C) \tag{3.28}$$

---

[22] Excuse the pun.

[23] This lattice was prepared in the MAD language by Norman Geflund (1998).

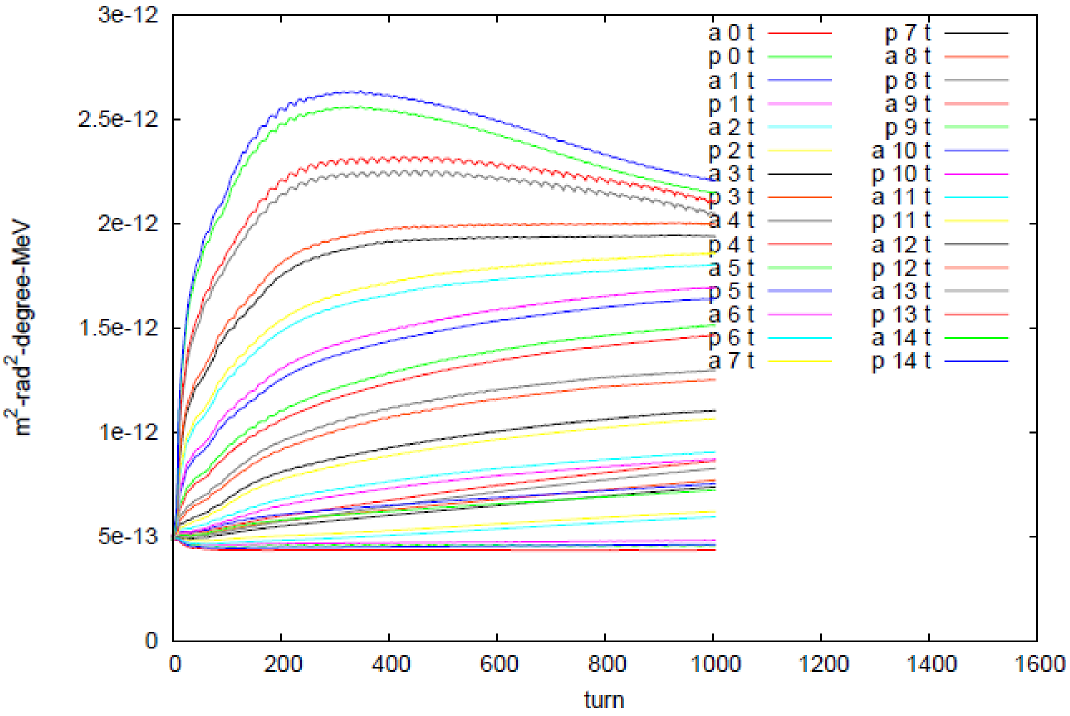

Figure 3.14. Juxtaposition of the Full 6D Emittance (**det**(C)) and the Product of the Three Uncorrelated 2D Emittances (**Dp**(C)). Color Scheme for the Various Intensities is Provided in the Legend.

In Figure 3.15, the maximal value of ϑ is plotted as a function of intensity. The value of ϑ increases with increasing intensity, but the fractional change between the correlation-corrected value of the 6D emittance and the uncorrelated "trace-space" emittance product is never more than 8% in this case. The validity of these corrections hinges on the fidelity of the simulation to the actual running conditions of the Booster.

The simulation as presented could have been refined further if it were likely that the correction were somewhat larger. In any case, the simulation can be performed to estimate the effect of the correlation terms, which could then in turn be applied to the measurement to correct for this correlation effect.

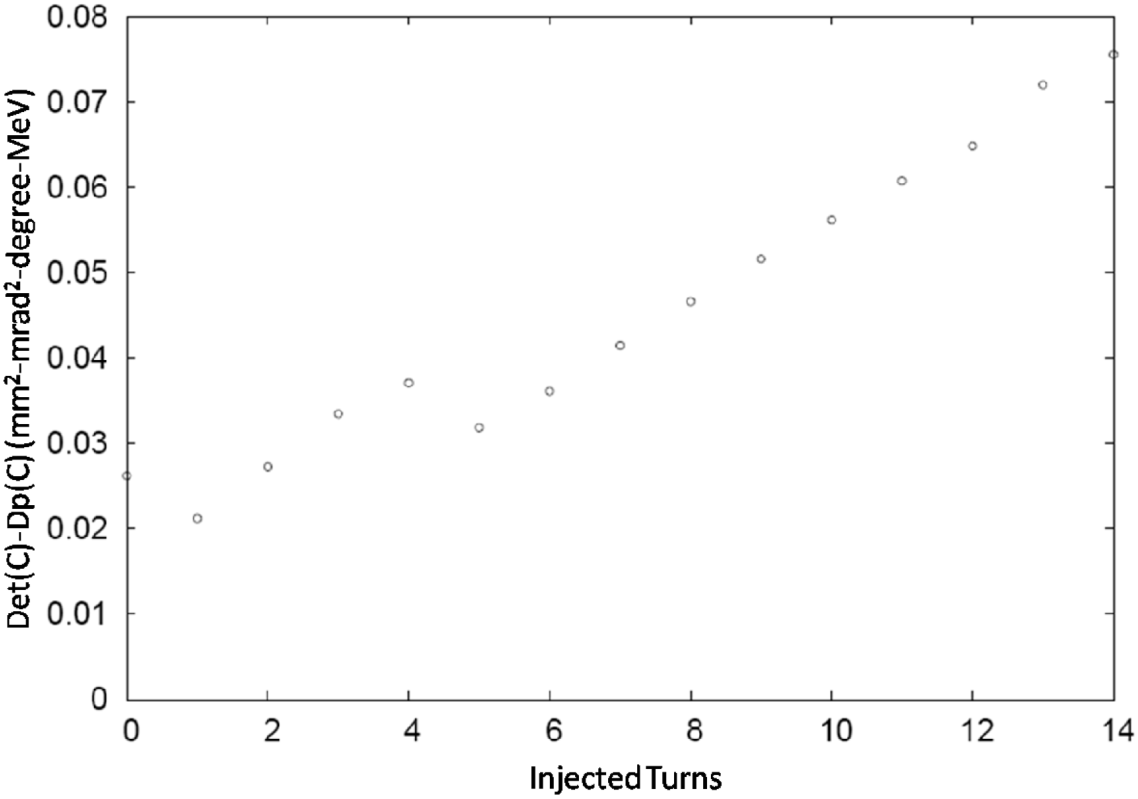

Figure 3.15. Discrepancy Between Correlated and Uncorrelated Emittance as a Function of Intensity in Simulation.

3.5 A Method for Characterizing the Halo Fraction of the Beam

From the previous sections it has been shown that a real beam is neither uniform nor does it have a defined boundary, rather its distribution tends to be denser toward the center with a diffuse collection of particles in the periphery. This has necessitated the introduction of RMS values for many quantities characterizing the beam, such as transverse position and momentum widths and emittance.

The definition of emittance using a certain fraction of the phase-space area occupied by the particles as a measure of the beam quality is prudent because the majority of the particles tend to lie within some reasonable phase-space region, while the outlying fraction occupies a much greater region. The typical convention for hadron colliders at

FNAL has been to consider the area occupied by 95% of the particles in the transverse planes. The other 5% were those whose motion is considered high enough amplitude (in position and momentum) that their inclusion would exaggerate the size of the RMS emittance. These particles do not faithfully obey the Hill-equation trajectories as particles with smaller amplitude would. While they comprise a small fraction of the total particle count, their presence is responsible in part for the exceeding of operating radiation limits and eventual damage to the accelerator elements, since these high-amplitude particles are what scrape the boundaries of the vacuum chamber.

With increasing intensity the space-charge forces will push more of the beam into this high-amplitude, nonlinear regime. The ability to quantifying the halo fraction for various intensities is thus important. In what follows we demonstrate a method of characterizing the relative beam-halo fraction using IPM data.

The transverse distribution is modeled as an elliptical Gaussian. A completely well-behaved transverse distribution would maintain a perfect Gaussian shape for all radial coordinates. A characterization of beam halo in the Booster has been done successfully by fitting the IPM response with a Gaussian-plus-linear distribution [134]. The ratio of area of the linear term (L) to that of the Gaussian term (G) can be used to give a measure of the fraction of particles residing in the halo. The larger the linear contribution to the fit, the greater the proportion of particles in the beam 'tails', outside the central core of the beam. The method was presented by J. Amundson *et. al* [6], where its properties as a figure of merit of beam quality were discussed.

We test the method under a large range of intensities from two injected turns (0.95×10^{12} particles) up to 18 injected turns (8.2×10^{12} particles). The nominal Booster intensity is at around 4.5×10^{12}, so with almost twice this value, we considerably more halo particles to exist.

Figure 3.16 shows intensity curves up to 3000 turns for injection-intensity values from 2 turns injected to 18 turns injected, taken from the IPM. The sudden small drop in intensity at 600 turns is the result of the beam notcher, which was left operational during the study. The priority was to obtain samples at very high intensity, where significant beam loss was inevitable, and since daily limits exist on integrated beam losses, multiple samples in these high-intensity regimes were deemed too disruptive to normal control-room operations.

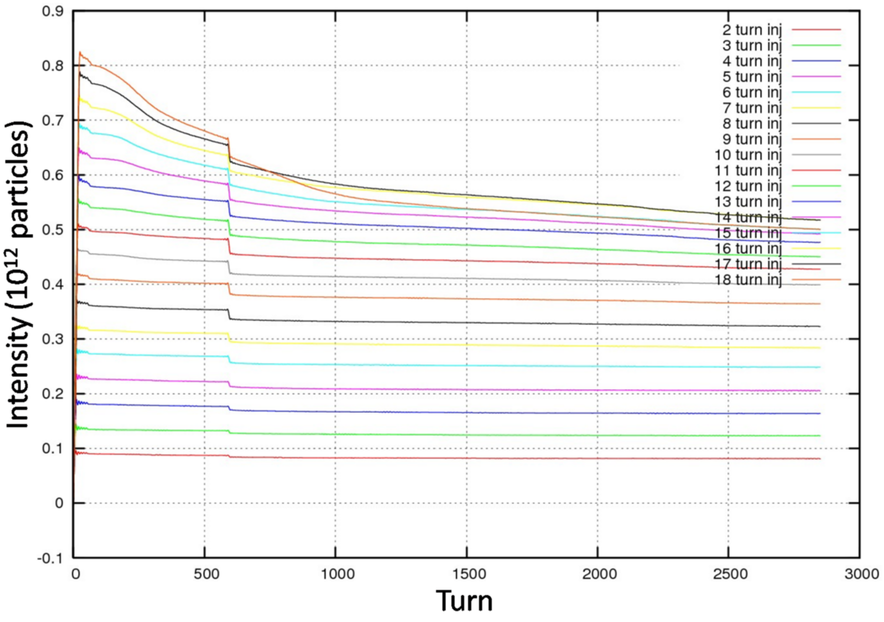

Figure 3.16. IPM Intensity Data from 9.5×10^{11} to 8.2×10^{12} Particles (Two to 18 Injected Turns). Coloring Scheme for the Various Intensity Curves is Provided in the Legend.

Losses during paraphasing and acceleration are seen to occur up to 300 turns for all intensities above seven injected turns. These become prominent at 12 injected turns, and dramatic by 15 injected turns. During the injection and paraphasing processes, the particles uncaptured by the RF systems remain unaccelerated. Since these are not carted along by the synchronous RF fields, they are quickly lost. These do not contribute to the halo and are not part of the IPM response. A localized beam loss, however, does tend to indicate a growth of the halo.

The corresponding RMS widths for the intensities in Figure 3.16 are shown in Figures 3.17 and 3.18. These have been filtered from raw IPM fits with a low-pass cutoff at 1⁄100 turns, with a sample size of 250 points. The oscillation in the first 125 turns is a result of this. Substantial beam growth is seen in the higher intensities, followed by a decrease in width after beam loss had occurred.

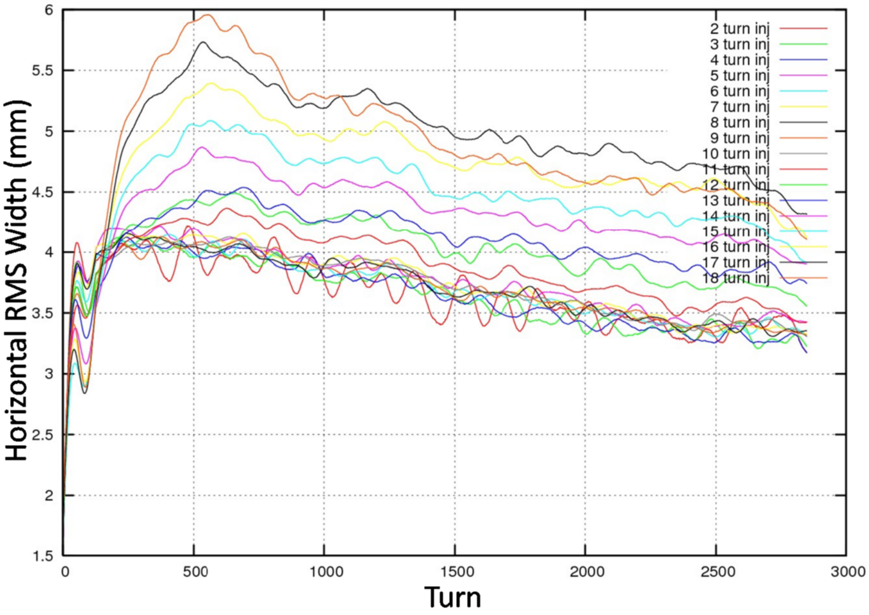

Figure 3.17. Horizontal RMS Width for Intensities from 9.5×10^{11} to 8.2×10^{12} Particles (Two to 18 injected turns). Coloring Scheme for Widths Corresponding to Different Intensities is Provided in the Legend.

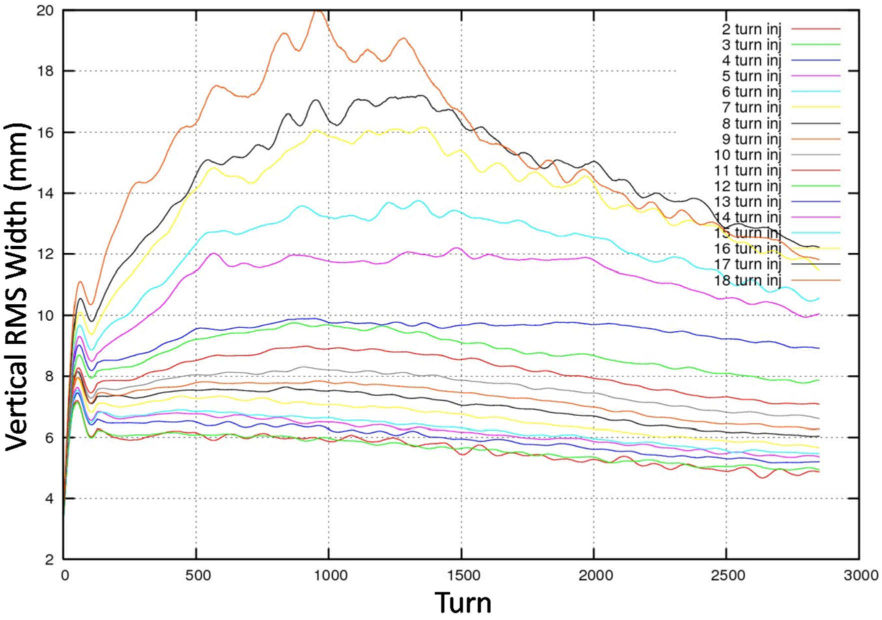

Figure 3.18. Vertical RMS Width for Intensities from 9.5×10^{11} to 8.2×10^{12} Particles (Two to 18 injected turns). Coloring Scheme for Widths Corresponding to Different Intensities is Provided in the Legend.

Figure 3.19 gives the ratio L⁄G of the fitted IPM profiles over 3000 turns for intensities of 5 injected turns and higher. Below this intensity the area of the linear component of the fit was quite small. As expected, the data show an increase in the amount of linear-area portion of the IPM fit for higher intensities.

The other factor influencing the shape of these curves is simply that the halo dissipates over time. For example, in the extreme case of 18 injected turns, L⁄G is nearly 0.5 at 1100 turns, but shrinks to 0.3 by 3000. With beam sizes approaching the size of the machine aperture, halo particles were most likely driven more rapidly into the vacuum-chamber boundaries, resulting in the observed decrease. Qualitatively it is evident that Presently it is not clear quantitatively how the ratio L⁄G corresponds exactly to the fraction of particles in the halo to that in the beam, since both terms are necessarily intertwined in the normalization from the particle count. Resolving this issue will require some independent calibration. Nonetheless, the method serves as a useful tool for the assessment of beam quality.

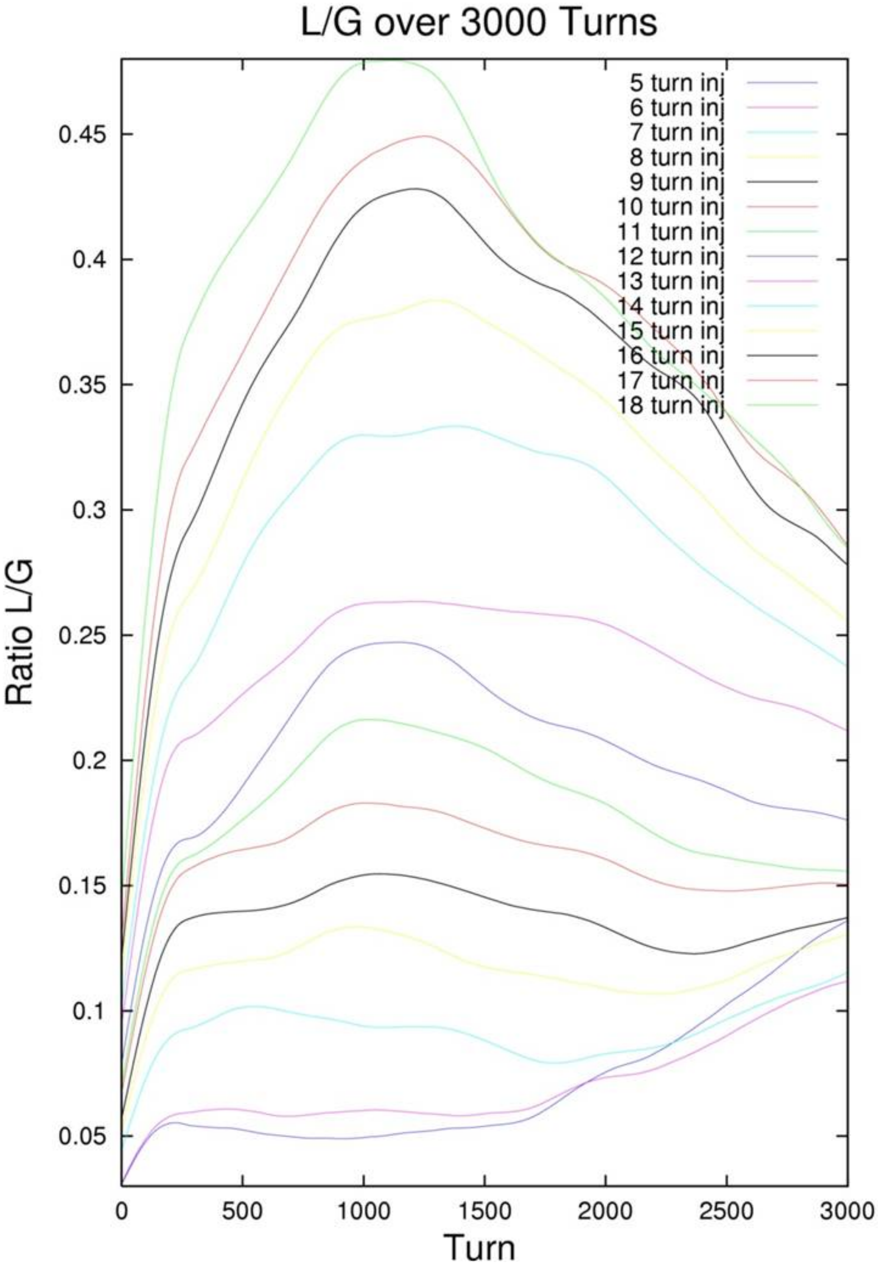

Figure 3.19 Ratio of Linear to Gaussian Area of IPM Fits (L/G) for Various Intensities from 9.5×10^{11} to 8.2×10^{12} Particles (Two to 18 injected turns) over 3000 Turns. Coloring Scheme for Different Intensities is Provided in the Legend.

CHAPTER 4

OVERVIEW OF THE THEORY OF TRANSVERSE WAKEFIELDS AND IMPEDANCES IN A PARTICLE BEAM WITH APPLICATION TO THE FERMILAB BOOSTER

4.1 Synopsis

Many of the collective effects associated with increasing particle density contribute directly to the limitations in intensity in a particle beam. Generally speaking, these can be divided into interactions within the beam (space charge) and the interaction between the beam and its surroundings (mainly impedances due to resistive wall and chamber geometries). The direct space-charge force within the beam is responsible for beam-size growth and tune spread. The impedance from the surroundings can cause a change in the energy, beam-oscillation growth, and tune shifts which in some cases can lead to certain instabilities. The purpose of this chapter is to describe the necessary theory used in the analysis of experimental results presented in Chapter 5, and also to some extent the data in Chapter 6.

In this Chapter the direct space-charge effects are compared to those of the surroundings, as per the analysis originally done by L.J. Laslett [73], treating the response from the vacuum chamber as a series of image charges and currents. It will be shown that while both phenomena are energy dependent, the tune shift from the direct space-charge decreases more rapidly with energy (γ^{-3}) than the surroundings (γ^{-1}). The contribution from space charge is significantly larger at the lower energies near injection.

The Laslett analysis is limited, however, in that the predictions assume perfectly conducting surroundings, and also no consideration of the changes in beam distribution due to the interactions with the vacuum chamber are given. Furthermore, in practice, magnets are comprised of a sequence of stacked steel laminations, and the magnetic properties of the material have an effect beyond just the existence of magnetic image currents. A more general analytical framework has been developed and detailed incorporating the solution to the Maxwell equations in cylindrical boundaries with finite conductivity [27, 76].

The forces on the particles arise from a vacuum-chamber response expressed in terms of so-called electromagnetic wake functions (a time-domain description) and the corresponding impedances (the corresponding frequency-domain description). As in the classical sense, this impedance is a complex quantity, consisting of a 'resistive' term and a 'reactive' one[24]. Work has been done in the Booster [42,78,112] to measure and predict this impedance and its effect on the beam at various energies. It has been shown that the resistive behavior of the material is responsible for oscillation growth-rates, while the reactive portion is responsible for the tune shift [90].

In addition to this accounting for the resistive wall with magnetic properties, further modification is also necessary when discussing surroundings of axially symmetric but non-cylindrical cross section [22, 59]. Specifically, for the nearly rectangular magnet geometries found in the Booster, a tune shift of opposite sign in the horizontal and vertical planes is expected from the analysis, in addition to a predicted defocusing shift in both planes due the wakefields associated with the oscillation of the beam as a whole.

To understand the effect of the surroundings on the beam, we start with an approximation of particle tune shifts due both to space charge as well as the vacuum-chamber boundary

---

[24] Physically, the real part of this impedance represents the resistive term and the imaginary part yields the reactive term, as it is in signal analysis.

in Section 4.2. The tune shift obtained by Laslett is given in Section 4.4. The tune-shift formulae obtained, as well as their modifications for the Booster geometry, are a special case of the more general (and elaborate) formalism involving the impedance of a resistive wall of finite thickness on a relativistic, bunched beam, given in Sections 4.6-4.8.

4.2 The Tune Shift Due to Space-Charge and Image Fields

While the effects of particle intensity on beam motion was considered since Kerst developed the betatron cyclotron[25], it was Laslett who first quantified how the transverse particle tunes are affected by forces not externally (i.e. intentionally) applied by the accelerator, arising both from the other particles in the beam itself and from the accelerator structure in which the beam is transported. The direct space-charge forces come from the interaction of particles on neighboring ones. Indirectly, the surroundings modify the free-space fields of the passing beam, allowing the electromagnetic energy to affect downstream particles. We first present a simple model of the intensity-dependent tune shifts due to the beam on itself and from its surroundings. The space-charge tune shift, due to the force on a particle from its neighbors in a cylindrical beam (i.e. one without longitudinal structure) will be given in Section 4.2.1, and the image-charge tune shift in Section 4.2.2. We spend some discussion on these simplified concepts to highlight comparable results from simulation. Image charges from the cylindrical pipe walls caused by the field of the passing beam are often a “usual suspect” for explaining tune shift under increasing intensity. These alone will be shown to be insufficient to explain measurements from the data presented in Chapter 5.

4.2.1 The Tune Shift due to Space Charge. The simplest transverse distribution of

---

[25] Hence the historical nomenclature of betatron oscillation and betatron tune.

particles is uniform, with a distinct beam edge at radius *a*. If we assume a particle in this uniform, relativistic, cylindrical beam is located a distance *r* from the center, the Lorentz force on this particle would be

$$F_r = \frac{2\lambda e^2}{a^2\gamma^2} r \tag{4.1}$$

where λe is the linear charge density. The advantage of this model is that the forces on the particles by the particles are linear. As was mentioned in Section 2.1.1.3, the Hill equation (2.5) describes most simply the single-particle dynamics in an accelerator and their perturbations in the presence of gradient errors. It can also be readily applied to the case of a single particle in this space-charge field of the beam. The corresponding tune shift, using this force in the Hill equation is

$$\Delta\nu_{sc} = \frac{\lambda r_0 R^2}{\nu_0 a^2 \beta^2 \gamma^3} \tag{4.2}$$

independent of the particle's transverse position, with r_0 being the classical (proton) radius. This result is obtained independent of the surroundings, either in a vacuum or in a closed accelerator structure.

Our aim is to compare this space-charge-specific result to the strength of the effect from the beam surroundings. One can estimate the effects of the conducting wall surrounding the beam by considering the omnipresent forces on the beam from 'image-charge' effects due to the collective beam motion within the chamber boundary.

The presence of the wall distorts the collective field of the beam, in turn modifying the space-charge forces experienced by the individual particles within the beam. One treatment of the effect of a conducting boundary is the familiar method of images. Instead of describing forces on a particle from a perturbed space-charge field due to the chamber boundary, one may consider the unperturbed space-charge field to which is added an image-charge contribution with the constraint that the (thin) conducting walls remain grounded everywhere. Obtaining this image-charge perturbation, one only needs to calculate the average force on the particle to obtain a result for the tune shift from the Hill equation.

4.2.2 Tune Shift Due to a Cylindrical Conducting Boundary. The following straightforward example shows how the method of images can be applied to obtain the fields in the presence of a grounded cylindrical beam-pipe. We start by solving the problem of an induced field on a grounded cylindrical shell from an elongated filament of charge. Starting with the configuration in Figure 4.1 for a point charge in a two-dimensional circular pipe,

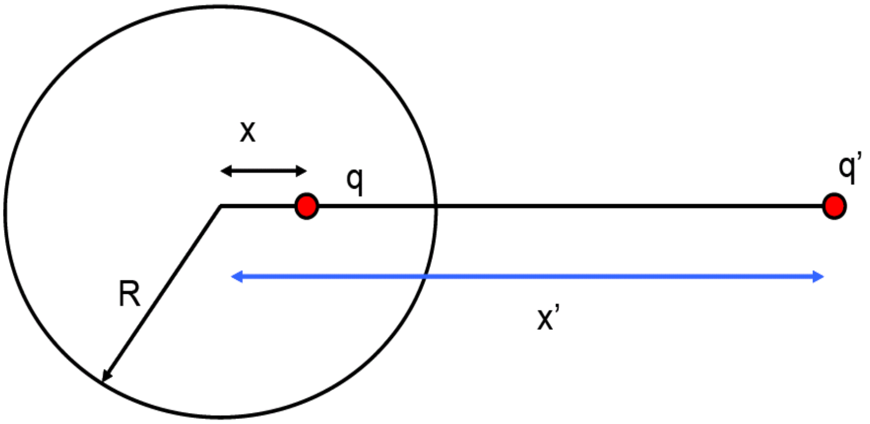

Figure 4.1. Image-Charge Configuration of a Point Charge in a Two-dimensional Circular Conducting Boundary

it is straightforward to show that

$$q' = -q\frac{R}{x}, \quad x' = \frac{R^2}{x} \tag{4.3}$$

And the field at q due to q' can then be expressed as

$$E = -q\left[\frac{1}{R/x - x/R}\right]\left[\frac{1}{R^2 - x^2}\right] \tag{4.4}$$

We now extend this to a uniform, transversely small beam bunch of length *L* and particle count *N* displaced by a distance x from the pipe axis (see Figure 4.2).

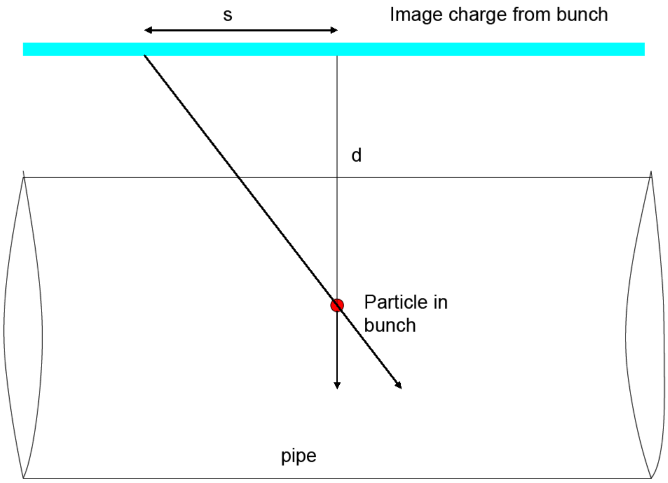

Figure 4.2. Image-Charge Configuration of an Individual Point Charge within a Long Charged-Particle Beam Bunch in a Cylindrical Conducting Shell

The field seen by a particle is a superposition of the fields of the image charges from the other point charges in adjacent infinitesimal 'slices.' The field seen by a particle in the longitudinal center of the bunch due to the image charge from the entire bunch is then given by

$$E = \frac{NeR}{R^2 - x^2}\frac{x}{\sqrt{1+\left[\frac{Lx}{2(R^2 - x^2)}\right]^2}} \tag{4.5}$$

We assume the bunch length is very much larger than the transverse dimensions, so that the image charges are created from a uniform, longitudinal field from the bunch, for *L*>>x*,* and L>>*a*, where *a* is the radius of the beam[26]. The force is then

$$F = eE = \frac{Ne^2 R}{R^2 - x^2} \frac{x}{\sqrt{1 + \left[\frac{Lx}{2(R^2 - x^2)}\right]^2}} \tag{4.6}$$

We estimate the contribution to the tune shift as follows.

From the Hill equation modified in the presence of a perturbation, (2.9), we stipulate once again that

$$\kappa^2 \ll \left(\frac{\nu_0}{R_{path}}\right)^2 \tag{4.7}$$

where R$_{\text{path}}$ is the orbit radius of the accelerator. In which case

$$|\Delta \nu| = \frac{F/x}{\gamma m \beta^2 c^2} \frac{R_{path}^2}{2\nu_0} \tag{4.8}$$

The tune shift on a particle bunch due to this image charge alone is then

$$|\Delta \nu| = \frac{N}{\gamma \beta^2} \frac{r_0 R_{path}^2}{2\nu_0} \frac{R}{R^2 - x^2} \frac{1}{\sqrt{1 + \left[\frac{Lx}{2(R^2 - x^2)}\right]^2}} \tag{4.9}$$

As with the previous image-charge case, the assumption of a uniform, hard-edged beam limits this to order-of-magnitude calculations. One noteworthy feature is the size of the tune shift relative to the case of this reactive pipe wall. The necessary parameters for evaluation of (4.2) and (4.9) are summarized in Table 4.1.

---

[26] The stipulation of a longitudinally large bunch is necessary because the superposition of fields given in (4.5) is only exact when all horizontal components vanish in the limit of an infinitely long bunch. In practice, this condition is always fulfilled for the Booster, where L/x~10^3.

Table 4.1. Beam and Machine Parameters for the Evaluation of Tune Shifts in (4.2) and (4.9)

Average Longitudinal density (λ)	1×10^{10}/m
Beam Radius (a)	5 mm
Number of particles per bunch (N)	5×10^{10}
Horizontal or Vertical Tune ($\nu_{x,y}$)	6.8
Total injection Energy (γmc^2)	1.34 GeV
Chamber Radius (R)[27]	4 cm
Orbit Radius (R_{path})	74 m
Typical Particle Oscillation (x)	~10 mm

The direct space-charge tune shift at injection, not considering the conducting wall, for a particle at the periphery of this uniform circular beam is around 3×10^{-1}. While for these typical Booster parameters, we obtain a tune shift of $3.3\text{x}10^{-4}$ for the wall effect, considerably smaller than the direct space-charge contribution near injection. This space-charge tune shift is in fact rather substantial. In practice values this large should be very inimical to beam stability. In Section 4.3 and 4.4.2 as well as in Chapter 6 we shall discuss these in more detail, and identify why it is of somewhat less concern and why such calculations exaggerate the value in any case. For now it is more useful as a comparative measure.

The calculations here are comparatively simple. We present them to compare the

---

[27] The sections of the Booster have differing shapes. Aside from the magnetic elements, the long and short drift sections have pipe diameters of 3.5" and 4.5" respectively.

analytical predictions to simulations using the same assumptions of a longitudinally long bunch with small transverse size in the presence of a conducting wall. Figures 4.3 and 4.4 provide simulation results for the effect of the presence of the conducting boundary in a cylindrical chamber for a small, unbunched, Gaussian beam of 5 mm in radius[28].

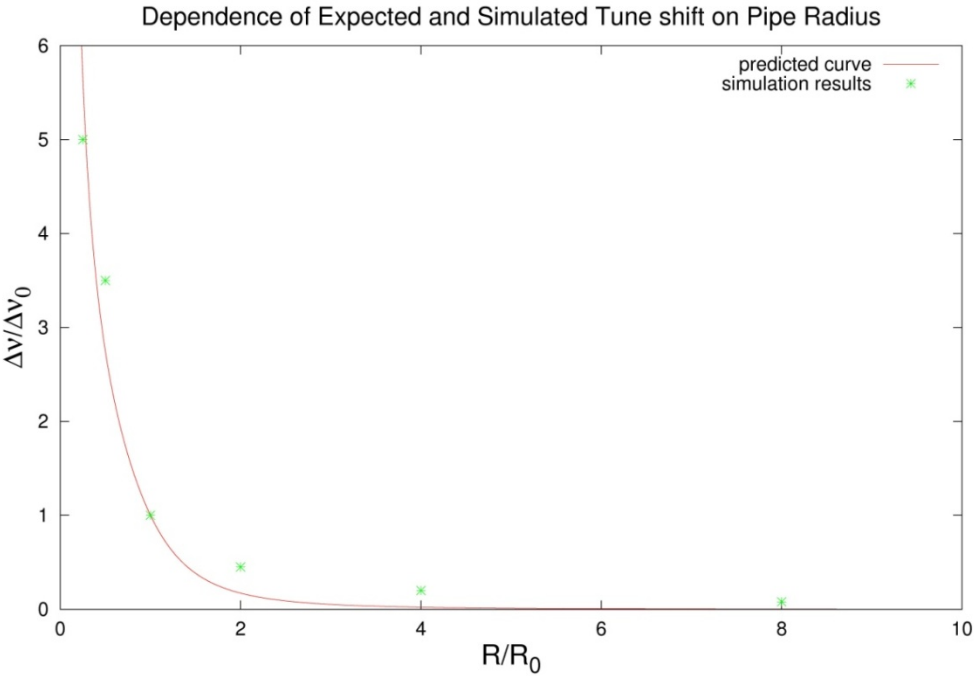

Figure 4.3. Dependence of Tune Shift on Chamber Radius for a 350mA Beam from Simulated (green) and Expected (red) Values Corresponding to (4.9).

The closed-boundary conditions with a grounded conducting wall provide the necessary image-charge effects for this. Figure 4.3 shows the tune shift dependence on chamber radius for a beam current of 350 mA (5×10^{12} particles), executing small oscillations in a circular conducting pipe ($R_0 = 4$ cm).

---

[28] For small enough beam relative to the pipe geometry, the distribution has negligible effect on the image charges.

Figure 4.4 shows the tune-shift dependence on beam intensity due to the pipe wall for a beam with intensity ranging from 0 to I = 5×10^{12} (I$_0$ = 5×10^{11} particles, or 35 mA) in a cylindrical chamber with a radius of 4cm. In both figures, Δν$_0$ is 1×10^{-3}. Reasonable qualitative agreement is seen in both cases, though quantitatively the simulaition result is larger by a factor of three compared to (4.9).

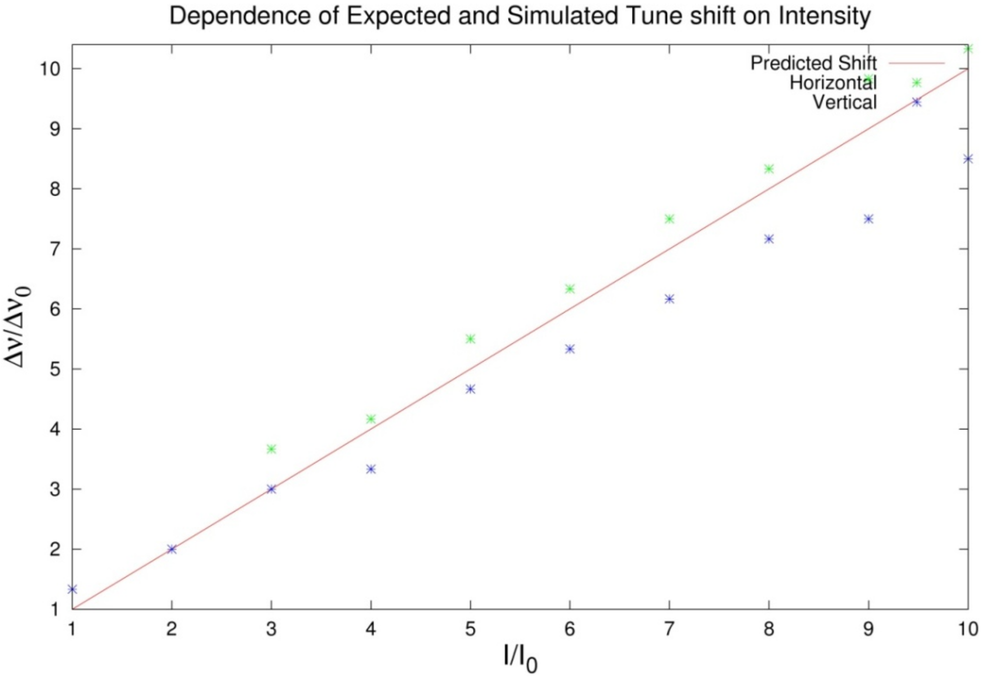

Figure 4.4. Dependence of Tune Shift on Intensity for a Small Beam in a 4-cm Cylindrical Chamber from Simulated (green, blue) and Expected (red) Values Corresponding to (4.9).

Part of this discrepancy is likely that the effect on a single particle differs somewhat from that of the beam as a whole. The calcuation of (4.9) is for the effect on a single particle in a rigid beam. The simulation obtains the tune by performing a Fourier transform of the centroid motion of a nonrigid distribution of particles. Since the centroid tune is plotted in Fig 4.4, there is no direct space charge contribution in this result, only the effect from the conducting boundary. Typically, when the effect of the motion on the beam centroid is what was observed in these simulations, it is usually larger by about a factor of three (for the case of electric image charges at least) when compared to the single-particle behavior.

Although the geometry of the previous example was simplified, it demonstrates the potential effect of beam-pipe walls on the betatron motion of the beam. Laslett took the analysis further, generalizing to the case of a beam with an elliptical cross-section, in a structure lacking cylindrical symmetry, and including the effect of magnetic pole faces. In the following section we present a discussion of this Laslett tune shift. In section 4.4 we shall demonstrate that the more involved analysis done by Laslett, based on the same principles, does not yield significantly different qualitative results (though the image effect is somewhat larger for reasons that will be clear). These therefore serve as a useful starting point for quantifying wall effects as well as the direct space charge.

4.3 Coherent and Incoherent Effects on a Beam

The shift of the tune of a single particle in a beam was discussed in Section 2.1.1.3, where it was quantified by (2.13). In Section 4.2 this was applied to the case of a transversely small beam in a grounded, cylindrical conducting pipe, and a particle on the edge of a uniform circular beam. However, what is typically measured in an accelerator is the average tune shift of the particle distribution, without detailed information at the individual particle level.

Forces arising from the interaction of a beam with the surrounding vacuum chamber (i.e. wakefields) can affect the ensemble of particles as a whole in such a way that the centroid motion of the beam is changed. All particles may be affected uniformly or nonuniformly, with the net effect of shifting this centroid motion. A centroid shift is considered a coherent effect. Other forces, such as those within the beam (e.g. space charge) affect individual particles in a completely position-dependent way. These do not affect the coherent motion of the beam (i.e. change the motion of the centroid) and are considered to be purely incoherent. Such internal forces do, however, change the distribution of transverse oscillation frequencies within the bunch, so while they do not modify the centroid tune, the spread of the particle tunes is affected[29]. External forces may change this tune spread as well, of course, if the effect is strongly position-dependent for individual particles. While this represents an incoherent behavior due to these external effects, to the extent that the centroid motion is on average changed because of this external force, the effect is considered a coherent phenomenon.

Instrumentation such as beam-position monitors are capable of observing the centroid motion and the collective effects on it, rather than the change in the motion of individual particles. So while single-particle effects such as space charge can be substantial for some particles and lead to some beam loss, this effect may not readily be measured with available diagnostics or instrumentation. Studies have been performed to determine experimentally the dependence of the betatron tunes on beam intensity. In Chapters 5 and 6 we shall detail measurements quantifying both the coherent and incoherent phenomena addressed here.

4.4 The Laslett Analysis

While the influence of space-charge on the betatron tune imposes intensity limits

---

[29] A familiar analogy in classical physics would be problem of the rocket exploding in mid-air.

on injected particle beams, the $1/\gamma^2$ magnetic cancellation of the space-charge force under high energy is a fortunate effect in that a higher injection energy assists in mitigating some of the effects associated with higher intensity. Since the susceptibility of the beam to perturbative forces is inversely proportional to $\beta\gamma$, maximal allowable beam intensity limited only by space-charge self-forces[30] scales as $\beta^2\gamma^3$. However, we note that other intensity-related effects may impose further intensity limitations. In particular we consider the vacuum-chamber response from a passing beam. For a perfectly conducting chamber acting on a passing beam, this amounts to an induced image-charge effect on the conducting surface, as well as image currents on the magnetic materials, resulting in perturbing electric and magnetic fields that do not cancel with increasing energy.

Though the manifestation of space-charge forces on individual particles in sufficiently intense beams was discussed by Kerst [70] and Blewett [14] in the 1940's, the inclusion of the vacuum-chamber response was first investigated by L.J. Laslett, who provided a formal treatment combining these effects [74]. The analysis details and quantifies both the combined incoherent effect of these self-forces on individual particles as well as a similar image-field perturbation on a beam centroid undergoing coherent transverse oscillations. The Laslett tune shift encapsulates the effects of forces on the beam from itself and the surroundings and extends it more precisely to other geometries, as well as accounting for the presence of magnetic material (a staple in all accelerator designs). A summary of the results is given as follows.

---

[30] Assuming we consider only the effect on a single particle and ignore other collective phenomena for the moment (e.g. Landau damping, etc.)

4.4.1 Equations obtained by Laslett.

Laslett treated the case of a uniform transversely elliptical beam with semi-major and semi-minor axes a and b, as first presented by Teng [120]. We note that care must be taken when dealing with the beam distribution. For a uniform, coasting beam, the linear particle density is simply the total number of particles Ξ divided by the accelerator circumference $2\pi R_{path}$ ($\Xi/2\pi R_{path}$). For a longitudinally bunched beam, one must also take into account the variation in current density of the passing particles, where peak current densities exacerbate this response. This can be handled by a "bunching factor" given by the ratio of the average to maximum linear charge density of the distribution. For the current analysis, we shall use this transversely uniform elliptical beam with longitudinal bunching factor B.[31] In this case the total number of particles can then be expressed as $\Xi = MN$ where M is the number of bunches and N is the number of particles per bunch.

We consider a beam with reasonably small transverse dimensions relative to the pipe radius (such that the image fields can be adequately obtained through approximation of point charge), in which there is a test particle undergoing small displacements y from the beam centroid. The analysis includes several effects on the motion of a particle - the image-charge electric field in the metallic chamber due to the passing beam (similar to what was previously derived), the induced magnetic fields produced in the magnets by an image current from the passing beam, and the space-charge fields from the surrounding particles subject to the $1/\gamma^2$ magnetic cancellation. In such case it was shown that the tune shift can be expressed as

---

[31] A full treatment would include additionally radial and azimuthal bunching. However, the analysis is not only considerably more difficult its effect is considered minimal compared to the precision of our measuring capability in the Booster.

$$\nu_0^2 - \nu^2 = \frac{2}{\pi B}\frac{MNr_0R}{b(a+b)}\Gamma\beta^2\gamma^3 \tag{4.10}$$

where Γ is a geometric factor accounting for the shape of the beam chamber given by

$$\Gamma = 1 + \frac{b(a+b)}{h^2}\left[\varepsilon_1\left(1+B\beta^2\gamma^2\right)+\varepsilon_2 B\beta^2\gamma^2\left(\frac{h^2}{g^2}\right)\right] \tag{4.11}$$

The quantities h and g are the semi-apertures (radii) of the vacuum chamber and magnet gap. ε_1 and ε_2 are "image-force coefficients," i.e. characterizations for various geometries. β,γ, and r_0 have their usual meanings from before. In the case of a plane-parallel boundary,

$$\varepsilon_1 = \frac{\pi^2}{48} \qquad \varepsilon_2 = \frac{\pi^2}{24} \tag{4.12}$$

A more convenient representation is given by

$$\nu_0^2 - \nu^2 = \frac{2}{\pi}\frac{MNr_0R}{h^2}\left[\varepsilon_1\left(1+\frac{1}{B\left(\gamma^2-1\right)}\right)+\varepsilon_2\frac{h^2}{g^2}+\frac{1}{B\left(\gamma^2-1\right)}\frac{h^2}{b(a+b)}\right]\gamma \tag{4.13}$$

At low energy (or for large apertures), single-particle tune shifts are more substantial than tune shift of the beam centroid, with intensities depending on $\beta^2\gamma^3$ while at high energy collective stability is the dominant intensity-limiting factor with the major behavior depending on γ. The importance of the aperture dimensions at high energy is as much a consequence of relativity as the magnetic cancellation of the self-fields. The field of a passing particle exhibits an angular spread on the order of 1/γ. For stationary charges the field is spherical and for ultrarelativistic ones it is pancake-shaped in the frame of the observer (flattened in direction of the motion). Since the total field energy remains constant for the same number of particles, the energy-density distribution changes with increasing energy (as observed in the laboratory frame). The image-charge response is thus more pronounced in the relativistic case, so that relativistic particles affect nearby trailing particles more substantially so long as the aperture is small enough.

Our previous calculations can now be refined by the Laslett framework. In Section 4.5 we shall apply these formulae to assess the relative importance of the space-charge and image-charge/current terms using Laslett coefficients more closely resembling the Booster geometry. We expect, as before, for energies near injection that the space-charge tune shift will dominate.

4.4.2 The Laslett Shift for Coherent Motion. It must be stressed that the Laslett tune shift in (4.13) is a single-particle effect, and must be applied as such to an individual particle within the beam. Often, for the most part due to measuring limitations we are interested more in effect on the beam centroid, for which this result is not applicable since it must exclude the effect of the mutual interaction of individual particles. A simple-minded approach in a calculation of the coherent tune shift would be simply to ignore the direct space-charge term, however, the averaging effect of the incoherent motion also changes the values of the coherent coefficients used in the calculation of the tune shift [75]. In that case, the analysis leads to the following.

$$\nu_0^2 - \nu^2 = \frac{2}{\pi}\frac{MNr_0R}{h^2}\left[\xi_1\left(1+\frac{1}{B\left(\gamma^2-1\right)}\right)+\xi_2\frac{h^2}{g^2}\right]\gamma \tag{4.14}$$

where ξ_1 and ξ_2 are the coefficients (in general different from ε_1 and ε_2) associated with this coherent beam-centroid motion. For the parallel-plate case as before, the values are

$$\xi_1 = \frac{\pi^2}{16} \qquad \xi_2 = \frac{\pi^2}{16} \tag{4.15}$$

The 'electric' coefficient ξ_1 is three times larger than ε_1 and the 'magnetic' coefficient ξ_2 is three-halves ε_2. The effect due to the internal fields present in the single-particle case is not applicable, since forces within the beam cannot directly affect the coherent motion. We shall differentiate between the two results by calling them the incoherent and coherent Laslett tune shifts. Both will be of use.

The reason for the larger values of the ξ_1, ξ_2 over ε_1, ε_2 can be explained as follows. The image fields are created by the presence of the entire beam. A single particle experiences this based on its position and charge. The effect on the centroid is the weighted average of the response of all the particles collectively to the image field. This response is thus somewhat larger. While the analysis leading to the exact evaluation of the parameters ε_1 and ε_2, as well as ξ_1 and ξ_2, is often lengthy for different structures, the shape of the chamber, to within an order of magnitude, has, in general, only a small effect on their numerical values.

4.5 Application to the Booster

We now seek to formally quantify the relative importance of the incoherent Laslett terms in the FNAL Booster near injection. This provides a basis for the discussion of the data presented in Chapter 6, in which the incoherent shift of the particle tunes are quantified. Since the betatron tunes in the Booster are around 6.8, and tune shifts rarely exceed 0.5 in any case for any machine, we can linearize (4.14) to get

$$\Delta\nu_{x,y} = -\frac{r_0 R}{\nu_0\beta^2\gamma}\frac{MN}{2\pi}\left[\frac{1}{\gamma^2}\left(\frac{1}{a^2}\mp\frac{\pi^2}{24h^2}\right)\frac{1}{B}\mp\beta^2\left(\frac{\pi^2}{24h^2}+\frac{\pi^2}{12g^2}\right)\right] \tag{4.16}$$

where R and a are the accelerator and beam radii respectively. Since our goal is the comparison of the importance of the space-charge fields to those on the chamber boundaries, we further assume, for simplicity, a circular, bunched beam. The bunching factor can be calculated from

$$B = \frac{\lambda_{avg}}{\lambda_{peak}} = \frac{M\sigma_z}{\sqrt{2\pi}R} \tag{4.17}$$

where σ_z is the longitudinal Gaussian bunch width. For the Booster it is around 0.5. The tune shift then can be written as

$$\Delta\nu_{x,y} = -\frac{r_0 R}{\nu_0\beta^2\gamma}\frac{MN}{2\pi}\left[\frac{1}{\gamma^2 a^2 B} \mp \left(\left(\frac{1}{\gamma^2 B} + \beta^2\right)\frac{\pi^2}{24h^2} + \frac{\pi^2\beta^2}{12g^2}\right)\right] \tag{4.18}$$

Or

$$\Delta\nu_{x,y} = \frac{r_0 R}{\nu_0\beta^2\gamma}\frac{MN}{2\pi}\left[K_{sc} \mp K_{wall}\right] \tag{4.19}$$

for the horizontal and vertical motions, respectively.

With a particle kinetic energy of 400 MeV, values of the relativistic parameters β and γ are 0.71 and 1.4, respectively. A few further simplifying assumptions are in order. We treat the ring as a set of parallel plates with half apertures around 3cm, with magnetic currents having an effective depth of 4 cm (60% of the ring is comprised of dipole magnets with this approximate shape and size, and the remaining pipe has this approximate radius, so the assumption is valid). A typical average beam radius for 5×10^{12} particles has been measured to be around 5mm, with the bunch being around 1 m long. Then

$$\frac{K_{sc}}{K_{wall}} \sim 50 \tag{4.20}$$

At injection with a kinetic energy of 400 MeV, evidently the direct space charge dominates (98% of the tune shift). The expected single-particle shifts due to the wall and the internal fields are around 1.3×10^{-2} and 6×10^{-1} respectively. For good measure, the corresponding coherent tune shift calculated from (4.14) is 5×10^{-2}, around four times the incoherent image-charge contribution.

This analytic formula was the one applied in Chapter 2 (Figure 2.6) as a benchmarking for the accelerator simulation tool, Synergia, which has been used periodically to complement our measurements. One limitation of the above Laslett analysis is that the result comes from the assumption of image charges and currents on perfectly conducting boundaries acting on particles causing them. While a defocusing effect on the transverse oscillations is indeed present, the picture is not complete in the case of relativistic beams surrounded by resistive (or rather, imperfectly conducting) walls, for which the lagging chamber response of a passing charge affects trailing particles of the beam in a different (and more complicated) way. We shall discuss these phenomena in subsequent sections, after which their correspondence to the Laslett analysis will be discussed in the limiting case. Despite this shortcoming, to first order the Laslett tune shift usually provides an adequate and relatively complete measure of the relative importance of the effect of the surrounding particles in the beam and that of the chamber boundaries for a particular energy. We shall further utilize the Laslett tune shift in Chapter 6 to corroborate a measurement of the space-charge tune shift, obtained indirectly through a beam-extinction measurement occurring under resonant conditions.

4.6 Inclusion of a Boundary with Finite Conductivity

Any real material comprising the vacuum chamber of an accelerator has finite conductivity. For relativistic particle beams the effect from this can be significant. Unlike in the perfectly-conducting case, the assumption of instantaneous feedback from the reactive pipe-wall field yielding a steady-state response is no longer valid in the relativistic regime. The field from leading particles in the bunch leaves an electromagnetic “wake” affecting trailing particles, whose properties depend on the resistivity of the material as well as the energy of the beam (the more relativistic the leading particle, the further back the field will affect trailing particles). The previously discussed image-charge (i.e. Laslett) analysis in this case is insufficient. In this section we discuss the concept of this resistive-wall wakefield and the corresponding impedance, its equivalent frequency-domain counterpart. An overview of the work leading to the classic time-domain wakefield equations is first provided, after which we detail the analysis leading to the case of a relativistic beam of arbitrary distribution in a circular cylindrical chamber.

The addition of finite conductivity to the pipe wall was first discussed by Neil and Sessler [90], who addressed its effect on the longitudinal beam dynamics, and, in collaboration with Laslett, it was shortly thereafter extended to the transverse case [76]. In the presence of finite-conducting walls, it was found by Neil *et al* that a beam with angular revolution frequency ω_0, having transverse oscillations with tune ν, generates fields of frequency $\omega = (n\pm\nu)\omega_0$, where n is an integer. A component of the pipe-wall response to these fields lies in phase with the transverse beam velocity, potentially driving betatron amplitude growth in the absence of sufficient transverse (and longitudinal) tune spread. The characteristic time of the oscillation growth was found to scale as $\sqrt{\sigma}/N$.

The important modification was this resistive component, creating an in-phase driving term responsible for instability growth. The nonresistive (i.e. Laslett) component yielded a 90° out-of-phase term giving the familiar tune shift. Development of the dispersion relations leading to the instability growth time were extended by Zotter [136] to various geometries (including laminated ones), and more recently by Lebedev and Burov [19, 20] for rectangular and cylindrical geometries of arbitrary thickness and including stacked or concentrically arranged materials with different electromagnetic properties.

The equations pertaining to the particle wakefields as self-consistent[32] perturbations on the beam were later derived by Laslett and Sessler [72], and subsequently the forces on the particles of the beam by Robinson [104] and Courant [38].

What follows in Sections 4.6.1-4.6.3 is a summary of the concepts leading to the resistive-wall wakefield equations for a relativistic beam in a circularly cylindrical chamber. A rather complete analysis is provided by Chao [27]. The application to the Booster will require special consideration because of its decidedly noncircular geometry, which will be discussed in Section 4.7.

4.6.1 Basic Formalism Describing Wakefield Phenomena. As was previously mentioned, in the transition from perfectly to imperfectly conducting walls, the location of a leading and trailing particle becomes important as the wall absorbs field energy from the leading particles and places it on the trailing ones. In general the field pattern stored in the chamber can be quite complicated, but usually the particle-oscillation wavelength of a relativistic beam is very much larger than the structure disturbing its motion, so our interest lies more in an integrated effect than the details of a local disturbance on the beam.

4.6.1.1 Wakefields in a Circular Chamber. Starting with the case of a very relativistic beam ($\gamma \to \infty$), the average force on the beam (or a particle) over the length L of some perturbing structure is given by

$$\frac{1}{L}\int_{-L/2}^{L/2} f ds = \bar{f} \tag{4.21}$$

Ultimately, these forces are obtained by solving for the time-dependent electromagnetic fields (i.e the Maxwell equations) produced by the leading particles in this axially sym-

---

[32] See section 1.3.2 for a definition of self-consistency.

metric geometry. Leading particles, however, may be distributed transversely in complicated ways.

As is commonly done in electrodynamics, these distributions can be decomposed into multipole moments, where the first terms are often dominant and subsequent ones negligible. The distribution can be described as a superposition of moments I_m, where the mth moment with net charge q and radius a, given by $I_m = qa^m$. The integrated forces[33] through this structure can then be obtained by

$$\int_{-L/2}^{L/2} ds\vec{F} = -\vec{\nabla} V \tag{4.22}$$

where for the resistive circularly symmetric structure V is a field-generating function given by

$$V = eI_m W_m(z) r^m \cos(m\theta) \tag{4.23}$$

W_m in the right-hand side is the so-called wake function – the strength of the response of the surroundings to a (longitudinally) δ-function beam with a pure mth-moment transverse distribution. The cosine term conveniently exploits the azimuthal symmetry of the chamber, i.e. for an mth-moment distribution the effect changes sign m times)[34]. In the case of a dipole oscillation (m = 1), the force would be positive on one side of the plane and negative on the other, resulting in a completely defocusing effect in that plane.

In this wake function is encapsulated the information regarding the response of

---

[33] Sometimes called an 'integrated impulse,' except that the longitudinal coordinate typically plays the role of time in accelerator pedagogy, so the units in this case are the same as that of energy, not momentum.

[34] In the ultrarelativistic case, the shape and size of the distribution play no role in the production of the wake [102], so it does not matter how the sign is varied, so long as the proper periodicity is maintained. Trigonometric functions are the most suitable choice in a circular chamber.

the cylindrical chamber to this particular oscillation of the beam. The force on the beam, like many quantities, is usually separated into a transverse and longitudinal part. Then the transverse and longitudinal integrated forces would be given by

$$\int_{-L/2}^{L/2} ds\vec{F}_{\perp} = -eI_m W_{m,\perp}(z) m r^{m-1}(\hat{r}\cos m\theta - \hat{\theta}\sin m\theta) \tag{4.24}$$

$$\int_{-L/2}^{L/2} ds\vec{F}_{\parallel} = -eI_m W_{m,\parallel}(z) r^{m}\hat{s}\cos m\theta \tag{4.25}$$

where $W_{m,\perp}$ is the transverse wake and $W_{m,\parallel}$ the longitudinal wake. Since we focus our attention mostly on the transverse dynamics, we are interested in the transverse wake. A connection, however, first presented by Panofsky and Wentzel, exists between the longitudinal and transverse wake forces given by

$$\nabla_{\perp}\int_{-L/2}^{L/2} ds\left|\vec{F}_{\parallel}\right| = \frac{\partial}{\partial s}\int_{-L/2}^{L/2} ds\left|\vec{F}_{\perp}\right| \tag{4.26}$$

That is, the transverse gradient of the longitudinal wake is the longitudinal derivative of the transverse wake. The connection between them will be used in Section 4.7, when the cylindrical symmetry is removed. In the case of a cylindrical pipe of radius R, length L, and material conductivity σ the transverse wake function is [33]

$$W_m(z) = -\frac{2}{\pi R^{2m+1}(1+\delta_{m0})}\sqrt{\frac{c}{\sigma}}\frac{1}{\sqrt{|z|}}L \tag{4.27}$$

Despite the need to modify the theory for the Booster's rectangular geometry, much of the Booster (40%) is round pipe, so (4.27) will be useful nonetheless.

4.6.2 Impedance - the Frequency-Domain Description. In using simulation tools, wakefield 'kicks' in the time domain are frequently applied to the beam to study the resulting dynamics. However, often it is more convenient to work with a frequency domain representation, particularly in analyzing experimental measurements of beam response, where signal analyzers are commonly used. An added utility of this wakefield description lies in its direct correspondence with the impedance, first introduced by Vaccaro and Sessler [111]. In particular,

$$Z_m^{\perp}(\omega) = i\int_{-\infty}^{\infty} \frac{dz}{c} e^{-i\omega z/c} W_m(z) \tag{4.28}$$

$$Z_m^{\parallel}(\omega) = i\int_{-\infty}^{\infty} \frac{dz}{c} e^{-i\omega z/c} W_m'(z) \tag{4.29}$$

which are the Fourier transforms of the wake functions[35]. This allows for a frequency-domain or time-domain description of the problem, whichever may be more suitable or convenient to the problem at hand.

Impedances arise from a multitude of sources - conceivably from every device comprising the accelerator body. Devices such RF cavities or diagnostic implements, coupling units such as vacuum-chamber bellows, and magnetic correction elements have an impedance. Careful design of an accelerator is required to minimize the cumulative effect of these elements [34]. In Section 4.7 both time-domain (wakefield) and frequency-domain (impedance) approaches will be used interchangeably to complete the analysis.

4.6.3 Effects Near and Far from the Leading Particle. Even in the rather simple axisymmetric geometry discussed previously, the fields comprising the wake function are quite complicated functions of z, and meaningful results are best obtained for approximations within various ranges of validity [30]. The exact expressions for the fields of a passing beam in a cylindrical resistive chamber were first developed by K. Bane [13].

---

[35] "There is a theorem stating when you have only a partial knowledge of the solution to a differential equation and do not know what to do next, make a Fourier transformation. This theorem is one reason why impedance is such a useful quantity."[45]

These are provided for reference in Appendix A.

The effect (both qualitatively and quantitatively) on trailing particles very near to the leading particles is substantially different from that from particles in, say, the subsequent bunch. Of course, 'near' and 'far' must be less arbitrarily defined. Generally, these depend on the dimensions of the vacuum chamber, not just on its diameter but also on the thickness of the material. The analysis is similar to that of fields in resistive waveguides.

4.6.3.1 The Low-Frequency Cutoff. High-frequency field components have a strong effect over a small time (equivalently, small range for passing particles) because their penetration into the material (i.e. skin depth) is inversely dependent on their frequency, while lower-frequency components (i.e. fields created over longer times) penetrate more deeply, affecting passing particles over a longer time (range).

A further cutoff, however, exists for a pipe of finite thickness in which the skin depth of low-frequency fields is comparable in size. In this case significant penetration (leaking) of the field outside the chamber occurs, preventing it from affecting the trailing beam after some very long range. "Far but not too far" will then refer to the case where the skin depth of the field from the leading particle(s) is much shorter than both the pipe radius and/or the thickness of the material comprising it, whichever is smaller. Usually, the upper limit on this region of interest is rather large, on the order of 10^5 to 10^7 meters for most accelerators. "Near but not too near" conversely, is less intuitive, and will be dealt with in the subsequent section. A typical dimensionless scaling factor χ quantifying these limits is defined by

$$\chi \equiv \frac{c}{4\pi\sigma R} \tag{4.30}$$

where R is the chamber radius and σ the conductivity. It can be shown [30] that for the resistive wall the lower and upper limits of this far-field region are given by the condition

$$R/\chi \gg |z| \gg \chi^{1/3} R \tag{4.31}$$

For the Booster, we consider a pipe with a 2.5-cm radius composed of steel, for which $\chi \approx 7\times10^{-8}$. The region of validity of this approximation is then between 0.1 mm and 3×10^{5} m, or for roughly 630 turns of the Booster cycle.

4.6.3.2 The High-Frequency Cutoff. It is also necessary to consider the near-field effects on trailing particles, i.e. where $|z| \ll \chi^{1/3} R$, very close to the leading particle. The wake-generating fields in this region are given in (A3-A4) in the appendix, but in the limit of zero distance behind the leading particle (z→0) we obtain

$$E_s \approx -\frac{4q}{R^2} \tag{4.32}$$

$$E_r = B_\theta \approx \frac{2q}{R}\left[\frac{R}{r} - \frac{r}{R}\right]\delta(z) \tag{4.33}$$

where r is the beam radial coordinate and q is the charge of the leading particle. In principle, this field for particles immediately behind the beam is both nonvanishing and potentially nonnegligible. However, so far, the assumption has been $\gamma\rightarrow\infty$. When this assumption is removed, in reality an upper limit on possible frequency component of the wakefield exists whose value depends on the relativisticity of the beam. We explain the physics of this as follows.

The number of oscillations per unit longitudinal distance depends on the angular spread of the pancake-shaped leading-particle field in that for a given number of oscillations associated with the field, the smaller the spread, the larger the number of waves packed into the longitudinal distance. This spread is proportional to $1/\gamma$. Hence a cutoff exists where $\omega \sim \gamma c / R$, or in other words, $\gamma \gg 1/\chi^{1/3}$. Or in another way, a pancake-shaped field represents a δ-function response in the time domain, which comprises all values in the frequency domain with equal weight. A field with an angular spread has a finite time width, and its frequency content rolls off after some value depending on this spread. In the Booster, this condition is satisfied when γ is much larger than 250. Since γ is 1.4 at injection and 9.6 at extraction this particular condition is never satisfied. However, the possibility of short-range wakes of some type may still be of concern.

Beam dynamics in the high-frequency regime is currently of interest, since it is in this region where instabilities limiting intensity are under investigation. Different authors have differing suggestions on the value of this and other frequency cutoffs [85]. In any case we focus on the regime with regard to our measurements, which are sufficiently far away from these high-frequency effects in any case.

4.6.4. The Force on a Particle due to a Dipole Wakefield. Ultimately the issue at hand is to quantify how these wakefields affect the trailing beam. The wake functions can be used to generate the wake potentials, which then describe the forces on the beam. The wake (vector) potential was given in (4.22-23).

We are interested in the m = 1 (dipole) wake, typically considered a dominant term for a beam undergoing resistive wall oscillations about the pipe axis [78]. For a beam bunch of charge q, whose average centroid displacement is <x>,<y>, the transverse wake "potentials" can then be written as

$$\int_{-L/2}^{L/2} ds\vec{F}_x = -eq\langle x\rangle W_1(z)\hat{x} \tag{4.34}$$

$$\int_{-L/2}^{L/2} ds\vec{F}_y = -eq\langle y\rangle W_1(z)\hat{y} \tag{4.35}$$

To perform an equivalent analysis as with the image-charge effects as done in the Laslett case, we must estimate the force on a particle in the beam bunch due to the leading-particle wakes. We assume the force on the bunch due to the pipe wall is slowly varying relative to the structure length L such that

$$\frac{1}{L}\int_{-L/2}^{L/2} ds\vec{F} \approx \bar{F} \tag{4.36}$$

From (4.27), the dipole wakefield is given by

$$W_1(z) = -\frac{2}{\pi R^3}\sqrt{\frac{c}{\sigma}}\frac{1}{\sqrt{|z|}}L \tag{4.37}$$

We assume, for the moment, a bunch of length L_0 with N_0 particles and with uniform longitudinal density of λ. In this case, the dipole force on a particle from the particles in front of it is, in either plane,

$$-\frac{2e^2\langle x,y\rangle}{\pi R^3}N_0\sqrt{\frac{c}{\sigma}}\left[\frac{2}{\sqrt{|z-L_0|}+\sqrt{|z|}}\right] \quad z \ge L_0 \tag{4.38}$$

and

$$-\frac{2e^2\langle x,y\rangle}{\pi R^3}N_0\sqrt{\frac{c}{\sigma}}\left[\frac{2\sqrt{z}}{L_0}\right] \quad z \le L_0 \tag{4.39}$$

outside and inside the bunch (assuming not too near the leading particle as discussed in Section 4.6.3.2). For $z \gg L_0$, the result reduces to

$$-\frac{2e^2\langle x,y\rangle}{\pi R^3}N_0\sqrt{\frac{c}{\sigma}}\frac{1}{\sqrt{|z|}} \tag{4.40}$$

where the bunch acts like a single particle of charge N_0e to the trailing particles far away. For an unbunched beam in a circular accelerator, we run into the problem of having a total particle density of $\Xi/2\pi R_{path}$, but with a test particle feeling a force accumulating as $\sqrt{z}$. In principle this would diverge, but as mentioned in section 4.6.3.1, a large-distance cutoff exists, usually because of the finite thickness of the pipe, limiting the accumulation effect. This phenomenon will be detailed more completely in Section 4.7 when the modification from the rectangular magnet geometry is considered.

We wish to quantify the tune shift caused by this bunch on a trailing particle (or bunch if we assume a single-particle bunch of charge N_0e and mass N_0m_p). Away from the bunch the tune shift from (2.13) is

$$\Delta\nu_{x,y} = \frac{N_0 r_p}{\gamma\beta^2} \frac{\langle x, y\rangle_{lead}}{\langle x, y\rangle_{trail}} \frac{R_{path}^2}{\pi R^3} \sqrt{\frac{c}{\sigma}} \frac{1}{\sqrt{z}} \frac{1}{\nu_0} \tag{4.41}$$

In general, the wake depends on the positions of the leading and trailing particles. We assume, for the moment, a behavior of a rigid bunch, where the motion of the trailing and leading components is in phase, i.e.

$$\frac{\langle x_{lead}, y_{lead}\rangle}{\langle x_{trail}, y_{trail}\rangle} = 1 \tag{4.42}$$

Also, we consider the effect at the edge of the bunch, where the contribution from the leading particles is maximized. We then obtain a dipole tune shift given by

$$\Delta\nu_{x,y} = \frac{N_0 r_p}{\gamma\beta^2} \frac{R_{path}^2}{\pi R^3} \sqrt{\frac{c}{\sigma}} \frac{2}{\sqrt{L_0}} \frac{1}{\nu_0} \tag{4.43}$$

In order to perform a calculation, the frequency dependence of the conductivity must be discussed, as follows.

4.6.5. The Frequency Dependence of the Conductivity. The electrical conductivity of a material is frequency-dependent, and in general complex. A typical model of it is given by [56]

$$\sigma = \frac{\rho_c e^2}{m_e} \frac{1}{\gamma_{damp}^2 + \omega^2} \left[\gamma_{damp} + i\omega\right] \tag{4.44}$$

where ρ_c and is the particle density of the conducting material and m_e is the mass of the free electron moving in the conductor for each particle. γ_{damp} is a characteristic phenomenological damping factor associated with the ability (or rather, inability) of the material to conduct, due to collisions, radiative effects, etc, and is given by the zero-frequency limit of

$$\gamma_{damp} = \frac{\rho_c e^2}{m_e \sigma_0} = \frac{\rho_c r_e c^2}{\sigma_0} \tag{4.45}$$

where r_e is the classical electron radius. Then (4.44) may be written as

$$\sigma = \sigma_0 \frac{\gamma_{damp}}{\gamma_{damp}^2 + \omega^2}\left[\gamma_{damp} + i\omega\right] \tag{4.46}$$

Physically, this suggests that materials which are good conductors at low frequencies are not very resilient to a frequency increase, and become resistive rather quickly. Poor conductors, by contrast, were never very good at conducting to begin with but their conductivity does not decrease as significantly under the same range in frequency increase. For the case of the steel Booster structures, the data in Table 4.2 yield a value of $\gamma_{damp} = 1.6\times10^{15}$/s.

Table 4.2. Characteristics of Steel for the Evaluation of γ_{damp}

Mass Density	~8 g/cm3
Conductivity (σ_0)	$1.3\times10^{16}\ s^{-1}$
Atomic Mass (iron)	55.85 amu
Particle density of steel (ρ_c)	$8.4\times10^{22}/cm^3$
Classical Electron Radius (r_e)	2.818×10^{-13} cm

The real (red curve) and imaginary (green curve) parts of σ are also plotted as a function of frequency up to $\omega = \gamma_{\mathrm{damp}}$ in Figure 4.5. We see that the real part of the conductivity retains around 90% of its value for up to $\omega = \gamma_{\mathrm{damp}}/4$, or for the case of steel, up to $3\times10^{15}\ \mathrm{s}^{-1}$.

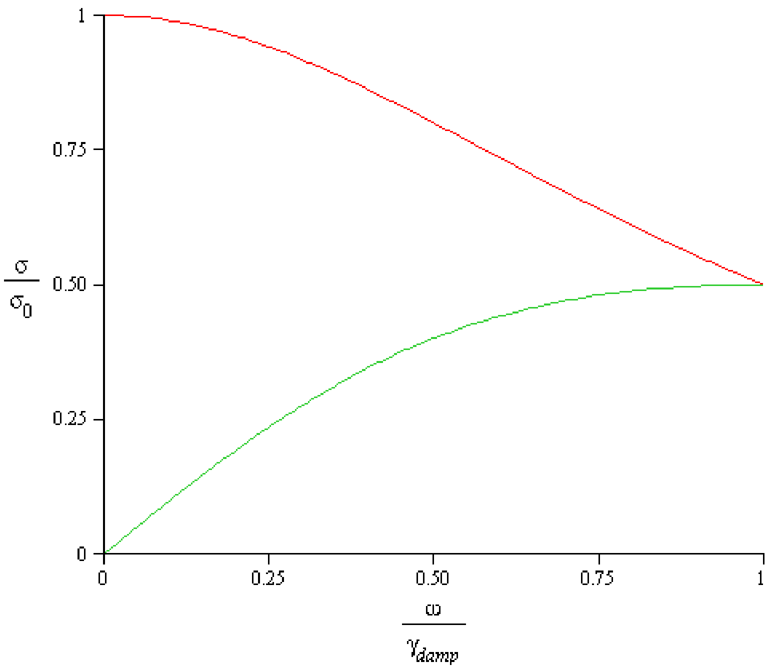

Figure 4.5. Frequency Dependence Real (red) and Imaginary (green) Parts of Conductivity Relative to Zero-Frequency Limit

Resistive-wall effects are considered broadband impedances, in that the response to a driving term is not very substantial but is similar across a very large range of frequencies. The driving frequencies of the passing beam can be decomposed into harmonics of the sidebands of the revolution frequency [114], that is

$$f = n(1 \pm \nu_f) f_{rev} \tag{4.47}$$

where ν_f is the fractional part of the betatron tune,[36] f_{rev} is the revolution frequency, and n is an integer. The strength of these harmonics diminish with increasing n, on the order of

$$P_n = \mathrm{J}_n\left(\omega_{rev}\tau_{\nu_f}\right) \tag{4.48}$$

where P_n is the power amplitude of the nth harmonic, J_n is the nth-order Bessel function, ω_{rev} is the angular revolution frequency, and $\tau_{\nu f}$ is the characteristic time amplitude of the fractional part of the betatron tune.

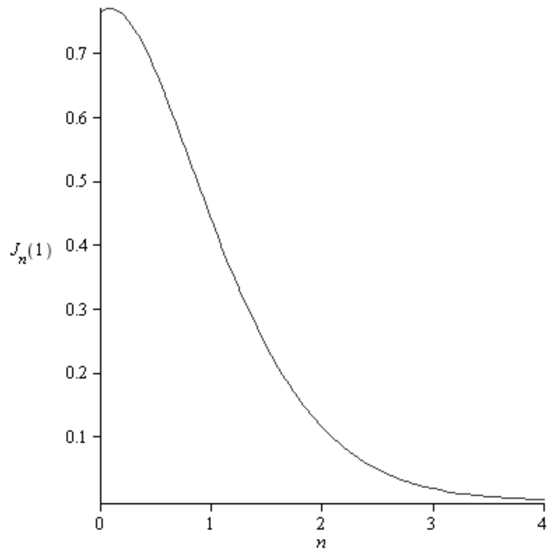

Figure 4.6. Dependence of Bessel Function on Index Value with an Argument of Unity

The argument $\omega_{rev}\tau_{\nu f} \sim 1$, so from Figure 4.6 we see that by n = 3 the power has dropped below 10% of the fundamental. The revolution frequency in the Booster is on the order of 500 kHz, thus strong frequency content from the passing beam does not exceed the range of 10 MHz, nine orders of magnitude below the threshold where the fre-

---

[36] This was done in particular for longitudinal motion but the analysis is analogous for the transverse case where the synchrotron tune is replaced by the fractional part of the betatron tune.

quency dependence of the conductivity becomes important. We therefore shall use the zero-frequency conductivity σ_0 in all our calculations.

4.6.6. Calculated Tune Shift and Possible Augmenting Accumulation Effects. The parameters necessary to evaluate (4.43) for a round, steel pipe in the Booster are given in Table 4.3.

Table 4.3. Booster Parameters for the Evaluation of (4.43)

Particle density (ρ_c)	$8.4\times10^{22}/\text{cm}^3$
Conductivity of Steel (σ_0)	$1.3\times10^{16}\ \text{s}^{-1}$
Number of particles per bunch (N_0)	5×10^{10}
Horizontal or Vertical Tune ($\nu_{x,y}$)	6.8
$\gamma\beta^2$	0.70
Chamber Radius (R)	4 cm
Orbit Radius (R_{path})	74 m
Classical Proton Radius (r_p)	1.535×10^{-18} m

Given these parameters, the tune shift from one bunch affecting a trailing particle is predicted to be 1.3×10^{-4}. This value is seemingly negligible compared to the previous calculations. However, this does not take into account the cumulative effect of passing bunches. The force causing this tune shift is scales as $z^{-1/2}$. Thus subsequent passing bunches could add to the wake before the previous one diminished completely. This would continue until eventually a steady-state value would be reached. For many passing bunches, the effect would be augmented as follows.

$$\Delta\nu = [\Delta\nu]_0 \sum_{n=1}^{N_C} \frac{1}{\sqrt{n}} \frac{\langle x_{lead}, y_{lead} \rangle_n}{\langle x_{trail}, y_{trail} \rangle_n} \tag{4.49}$$

N_c is the numerical cutoff, either for the regime given by (4.30) or a value dependent on the thickness of the pipe. The effect of the pipe thickness will be discussed in detail in Section 4.7.3. Also, the effect depends in principle on the average transverse positions of both the leading and trailing particles (or bunch centroid, as the case may be). While the accumulation of wakes from passing bunches may be rather large, in the worst case by a factor of 500 for the cutoff in Section 4.6.3.1, in almost all circumstances the average particle positions would average to zero. We expect, then, on average, for a cylindrical steel pipe the effect on the centroid tune would remain rather small[37].

However, the Booster is not comprised completely of round steel pipes, but of nearly rectangular magnets in 60% of its circumference. Such cumulative properties as discussed here will be shown to be important if the average effects do not cancel. In the next section we discuss the modification of this formalism to make it applicable to the Booster's geometry. The main difference is that in the absence of the pure axisymmetric geometry, the $\cos m\theta$ and $\sin m\theta$ patterns present in (4.24-27) for the multipole mth-order wakes no longer yield eigenmodes and the different m's couple. The analysis thus becomes more complicated, and depend both on the positions of the particles driving the wakefield as well as those trailing them. We must resort to a more general formalism taking these cases of lower symmetry into account, at least for the case of rectangular symmetry.

---

[37] The effect on the growth rate and on particles very near the disturbance is not discussed in this work. In principle these may still be large in these circumstances.

4.7 Wakefield Behavior in Structures of Lower Symmetry

As mentioned previously, the wakefields, classified by mth-order multipole moments of the beam distribution, were developed under the condition of cylindrical symmetry and for an ultrarelativistic beam. In the case of less symmetric structures a more general treatment is required.

4.7.1 Synopsis. We present the concept of a generalized impedance, first introduced by Sacherer and Nassibian [89], and applied to relevant geometries by Heifets, Wagner, and Zotter [59]. The formal steps to obtaining a general expression for the transverse wakes is outlined, after which the particular case of rectangular symmetry is investigated. The corresponding wakefield produced by the dipole motion of the beam is discussed.

A summary of the analysis by Chao, Zotter, and Heifets [22] is presented, wherein the effect of additional quadrupole term for a dipole-distributed beam due to these noncircular chamber geometries is developed and shown, unlike its dipole counterpart, to have an additive cumulative effect on the motion of the beam in a circular accelerator. The tune shift due to this multi-turn wakefield accumulation is then given and adapted to the Booster. Ultimately this equation will be of paramount importance in explaining the measurements in the following chapter.

4.7.2 A Summary of Generalized Impedances for Noncircular Cross Sections. The presentation of the wakefield equations in the previous section assumed a very relativistic beam in a cylindrical vacuum chamber with particle-oscillation wavelength much longer than any wake impulse caused by chamber variation. Since 60% of the Booster lattice is comprised of dipole magnets with somewhat rectangular geometries, as discussed previously, the mth-order wakes corresponding to the mth-moment beam distributions in a cylinder, are no longer independent, and will couple. Of primary importance is the addition of a quadrupole contribution to a beam executing dipole motion. To handle this analytically for more arbitrary structures, we utilize the concept of a generalized impedance [89], a quantity depending both on the coordinates of the leading particle (r_0,φ_0) as well as that of a trailing particle (r,φ). The term "generalized" refers to the dependence on both the leading and trailing particles, more so than just geometry of lower symmetry.

While in the case of purely circular cross sections, dipole, quadrupole, etc, wakefields are the result of oscillations within the distribution, for lower symmetry, the structure can produce strong higher-order wakefields even for a beam for any type of oscillation (dipole, quadrupole, etc). We summarize the analysis [59], focusing on the results leading to the quadrupole wakefields created by rectangular geometries. Starting with this impedance, the only assumption, specifically, is that of causality, i.e.

$$Z(\omega,r,\varphi,r_0,\varphi_0)=Z^*(-\omega,r,\varphi,r_0,\varphi_0) \tag{4.50}$$

The formal details are given in Appendix B. The idea behind it is as follows.

A longitudinal electric field synchronous with the particle motion produces a longitudinal impedance to the beam. The impedance can be expanded in terms of multipole moments in both r and r_0, where the expansion coefficients are proportional to the frequency content of the field from passing beam. That is,

$$\begin{aligned} Z_{\|}\left(\omega,\vec{r},\vec{r}_0\right)=\sum_{m=1}^{\infty}\sum_{k=0}^{\infty}\Big\{&\left[\alpha_{mk}\left(\omega\right)r_{0+}^{k}+\beta_{mk}\left(\omega\right)r_{0-}^{k}\right]r_{+}^{m}+\ldots\\ &\ldots+\left[\alpha_{mk}^{*}\left(-\omega\right)r_{0-}^{k}+\beta_{mk}^{*}\left(-\omega\right)r_{0+}^{k}\right]r_{-}^{m}\Big\}\end{aligned} \tag{4.51}$$

where the quantities r_+ and r_- are the complex rectangular superpositions x±iy. From the longitudinal impedance we obtain the longitudinal wake function, which is related to the transverse wake by the Panofsky-Wentzel theorem. In terms of the generalized wake functions, this may be written as

$$\nabla_{\perp} W_{\parallel}\left(\vec{r},\vec{r}_0,s\right)=\frac{\partial}{\partial s}W_{\perp}\left(\vec{r},\vec{r}_0,s\right) \tag{4.52}$$

and the corresponding wakefields can be obtained. These results can be expressed as

$$\begin{aligned} W_x(s)=\sum_{m=1}^{\infty}\sum_{k=0}^{\infty} m\Big\{\Big[a_{mk}(s)r_{0+}^{k}+b_{mk}(s)r_{0-}^{k}\Big]r_{+}^{m-1}+\ldots \\ \ldots+\Big[a_{mk}^{*}(s)r_{0-}^{k}+b_{mk}^{*}(s)r_{0+}^{k}\Big]r_{-}^{m-1}\Big\} \end{aligned} \tag{4.53}$$

$$\begin{aligned} W_y(s)=\sum_{m=1}^{\infty}\sum_{k=0}^{\infty} im\Big\{\Big[a_{mk}(s)r_{0+}^{k}+b_{mk}(s)r_{0-}^{k}\Big]r_{+}^{m-1}-\ldots \\ \ldots-\Big[a_{mk}^{*}(s)r_{0-}^{k}+b_{mk}^{*}(s)r_{0+}^{k}\Big]r_{-}^{m-1}\Big\} \end{aligned} \tag{4.54}$$

where

$$\frac{\partial a_{mk}(s)}{\partial s}=-\alpha_{mk}(s),\quad \frac{\partial b_{mk}(s)}{\partial s}=-\beta_{mk}(s) \tag{4.55}$$

are another set of expansion coefficients. We have suppressed the dependence of $W_{x,y}$ on r and r_0 to simplify the notation. One caveat is in order regarding this theorem. This analysis considers all contributions of every order to the impedance, and does not (in fact, in general cannot) separate them distinctly into the multipole moments as was done in Section 4.6. This impedance was obtained directly from the integration of the synchronous feedback field from boundary of the vacuum chamber, whatever its geometry may be. The 'multipole' behavior is then characterized by the expansion coefficients of the double sum in (4.51), and correspondingly (4.53-54), specifically tied to products of powers of r and r_0. The symmetry of the structure (or lack thereof) then determines the important contributions (e.g. dipole, quadrupole, etc), in addition to the moments of the beam distribution. In short, the leading-particle coordinates correspond to the distribution moments and the trailing-particle coordinates account for the structure harmonics of the chamber geometry. Thus with the exception of simple geometries, these modes will remain intertwined.

Also, in the analysis in Section 4.6, the multipole wake functions were developed as part of the wake-potential-generating function (4.23) which in turn, ultimately encapsulates the resulting wake forces as functions of m. For the convenient case of cylindrical symmetry, these can be written in terms of separable powers of the single variable r (leading particle). Hence V scales explicitly as r^m, such that the dimensions of the wake function scale commensurately as r^{-m} if dimensions of the wake potential are to be consistent. Under this convention, the Panofsky-Wentzel theorem equates the transverse gradient of the longitudinal wake potential to the longitudinal derivative of the transverse wake potential, and is more commonly used. For (4.52), where W is the generalized wake function, the relation is more general.

In the following section we apply (4.53-54) to the special case of the Booster, whose magnet geometry is approximately rectangular. From these wakes, we then present formulae for the tune shift under these conditions.

4.7.3 Application of the Generalized Wakefields to the Booster Magnets.

Applying the above results to the rectangular (or parallel-plate) case, the transverse wakes produced in this manner reduce to the following.

$$W_x(s) = a_0 x_0 + ax \tag{4.56}$$

$$W_y(s) = -\bar{a}_0 y_0 - ay \tag{4.57}$$

(x_0,y_0) are the driving-particle and (x,y) the trailing particle coordinates, respectively. Both fields yield the coefficient a, while the coefficients a_0 and $\bar{a}_0$ are inter-related but not identical. Regardless of their exact values, the interesting features of these equations are that the wakefields for this geometry have separate, substantial contributions from the driving particle (dipolar component) and the trailing particle (quadrupolar component), and this quadrupole component affects both planes equally, for the same trailing-particle displacement.

These effects have been explored in particular by Chao, Zotter, and Heifets [22] who were studying the effect in the roughly octagonal chambers of the CERN PSR. It was shown that laterally symmetric but noncircular geometries produced higher-than-mth-order contributions to the wakefields for mth-moment beam distributions. The work by Heifets, Wagner, and Zotter [59] has provided the necessary groundwork for this modification.

In addition, a somewhat unintuitive feature of (4.56-57) shows that the quadrupolar contribution, is independent of the driving term, with a purely real coefficient equal in both planes (though opposite in sign). The dipole wake over many terms averages to zero, since the oscillation of the particles about the center of the chamber produces both positive and negative forces, as was alluded to in the analysis leading to (4.49), so its cumulative effect may seldom be of concern. The quadrupole term, by contrast, produces a force which is strictly additive and may lead to a substantial effect over many turns if the lingering wakefield from successive turns in the accelerator accumulates sufficiently turn-by-turn. The effect can be surprisingly large compared to the classical wakefield analysis in cylindrical symmetry. In what follows a similar analysis applied to the case of the parallel-plate-like geometry of the Booster magnets is detailed, the results of which will later be used to explain experimental results.

4.7.3.1 Wakefields Including the Skin Effect. It has been shown [90] that for frequency-dependent fields in the resistive wall, so long as the wall thickness is larger than the skin depth for frequencies of interest, the resistive and reactive portions are equal, and the wakefield formalism holds for all distances given by (4.31). The transverse resistive-wall wake function for a distance z behind a dipole-charge can be expressed in these terms as

$$W(z) = -\frac{4\delta_0}{b^3}\sqrt{\frac{C}{z}} \tag{4.58}$$

where

$$\delta_0 = \sqrt{\frac{c^2}{2\pi\mu\omega_0\sigma_0}} \tag{4.59}$$

is the skin depth of the material at the revolution frequency $\omega_0 = \beta c/R_{path}$ and C and R_{path} are the machine circumference and radius, respectively. For magnetic materials, μ is the relative permeability of the substance (usually set to unity otherwise). In Chapter 5 this will be of importance when the magnetic laminations are considered. For now it is ignored (i.e. equal to unity). The factor *b* corresponds either to the pipe radius or the half-width of parallel plates, depending on geometry.

4.7.3.2 The Complex Mode-Frequency and its Dependence on Impedance. We assume a train of bunches whose internal structure can be represented sufficiently by a pair of macroparticles, i.e. one particle in front (driving) and one particle in back (trailing). For this type of bunch, a model in which the perturbation comes from the collective wake forces from all leading particles can be composed, as was first done by Courant and Sessler [40]. Unlike the Hill-equation formalism, however, the modes of oscillation from these collective effects are complex in general. In the same way that the impedance is a complex quantity encapsulating both the growth rate and tune shift, the complex mode-frequency Ω, dependent on this impedance can also be defined analogously.

In terms of the wake W or the corresponding impedance Z, for a single particle in the ring [25, 52],

$$\Omega^2 - \omega_\beta^2 \propto \sum_{k=1}^{\infty} e^{2\pi ik\Omega/\omega_0} W_1\left(-kC\right) \tag{4.60}$$

or

$$\Omega^2 - \omega_\beta^2 \propto \frac{\omega_0}{2\pi i} \sum_{p=-\infty}^{\infty} Z_1^{\perp}\left(p\omega_0 + \Omega\right) \tag{4.61}$$

where ω_β is the corresponding betatron mode frequency (specifically, ω_β/ω_0 is the betatron normal-mode tune). The mode-frequency shift $\Delta\Omega$ and the growth rate τ^{-1} can then be obtained from

$$\Delta\Omega = \mathrm{Re}\left(\Omega - \omega_\beta\right) \tag{4.62}$$

$$\tau^{-1} = \mathrm{Im}\left(\Omega - \omega_\beta\right) \tag{4.63}$$

and the tune shift, for good measure, is

$$\Delta\nu = \left(\Omega - \omega_\beta\right)/\omega_0 \tag{4.64}$$

We note the factor if *i* in (4.62-63) reverses the convention where the growth rate is the real part and the tune shift is imaginary part of the impedance.

4.7.3.3 The Quadrupole-Wake Effect on the Complex Mode Frequency. The extension of this to multiple bunches can be found elsewhere [26], but it can be shown that the general mode-frequency shifts of a beam due to a dipole wakefield of this type in a circular chamber for multiple, evenly spaced bunches are given by [23]

$$\Delta\Omega_x = -\frac{6\sqrt{2}}{\pi^2\omega_x}\Gamma\left[g(\nu_x) + if(\nu_x)\right] \tag{4.65}$$

$$\Delta\Omega_y = -\frac{6\sqrt{2}}{\pi^2\omega_y}\Gamma\left[g(\nu_y) + if(\nu_y)\right] \tag{4.66}$$

where ω_x, ω_y are the (angular) horizontal and vertical betatron oscillation frequencies, ν_x, ν_y the horizontal and vertical tunes, and

$$\Gamma = \frac{\pi}{6}\frac{\Xi r_p c^2}{\gamma b^3}\left[\frac{\delta_0}{2R_{path}}\right] \tag{4.67}$$

with Ξ the number of particles in the beam, and r_p the classical proton radius, and γ the Lorentz boost. If we let S_b be the bunch spacing, the functions g and f are the imaginary parts of the double sum, given by

$$g(\nu) + if(\nu) = \frac{1}{n_b}\sum_{m=1}^{n_b}\sum_{k=1}^{\infty}\sqrt{\frac{2}{k+\frac{mS_b}{C}}}\exp\left(2\pi i\nu\left[k+\left(mS_b/C\right)\right]\right) \tag{4.68}$$

g(ν) corresponds to the frequency shift as in (4.62) and f(ν) gives the growth rate as in (4.63). Traversing from a circular to a parallel-plate (or rectangular) geometry, the mode frequency shifts, aside from a different coefficient, contain an extra additive term, given by

$$\Delta\Omega_x = -\frac{\Gamma}{2\sqrt{2}\omega_x}\left[g(\nu_x) + if(\nu_x) + \frac{L}{C}\sqrt{2}h\right] \tag{4.69}$$

$$\Delta\Omega_y = -\frac{\Gamma}{2\sqrt{2}\omega_y}\left[2g(\nu_y) + 2if(\nu_y) - \frac{L}{C}\sqrt{2}h\right] \tag{4.70}$$

where h is the modification for quadrupolar wakes given by

$$h = \frac{1}{n_b}\sum_{m=1}^{n_b}\sum_{k=0}^{\infty}\sqrt{\frac{1}{k+\frac{mS_b}{C}}} \tag{4.71}$$

The lingering of the wakefield over successive turns is a result of the symmetry of the chamber, as discussed in the analysis leading to (4.56-57). While the oscillatory behavior of the dipole terms tends to cancel them off turn by turn, the quadrupolar wakes in the presence of this geometry are, as before, strictly additive. As-is, the series is divergent, but this would only be true for an infinitely thick chamber, in which all wakefield frequencies for every integer value of k behave in this manner. In any structure of finite thickness Θ, the low-frequency (large-valued k) field penetrates the material, modifying the behavior of the wake function for large distances (times). The modification for a cylindrical chamber has been done analytically [53, 94], but it has been shown that numerically [24] the effect of the finite wall is similar for the rectangular case. In particular,

$$W_{\perp}(z) = -\frac{4\delta_0}{b^3}\frac{L}{C}\left[\sqrt{\frac{C}{z}}\right] \tag{4.72}$$

for small z, and

$$W_{\perp}(z) = -\frac{4\delta_0}{b^3}\frac{L}{C}\left[\pi\frac{\delta_0}{\Theta}\exp\left(-\frac{\pi\delta_0^2 z}{\hat{r}b\Theta C}\right)\right] \tag{4.73}$$

for large z, where the transition occurs for the value of z where (4.72-73) are equal. The factor $\hat{r}$ is a geometric factor associated with the thickness of the chamber. It was shown by Zotter [137] that, for the case of a circular pipe, this is given by

$$\hat{\mathrm{r}}_{\mathrm{pc}} = 1 - \frac{\mathrm{b}^2}{\text{þ}^2} \tag{4.74}$$

$$\hat{\mathrm{r}}_{\mathrm{pm}} = 1 + \frac{\mathrm{b}^2}{\text{þ}^2} \tag{4.75}$$

for a perfect conductor and a perfect magnet, respectively. We shall refer to these as "Zotter Ratios" from now on. The quantity þ represents a distance outside the chamber boundary through which the fields have penetrated, that is, where

$$\text{þ} \geq b + \Theta \tag{4.76}$$

The Zotter ratio suggests that thin conductors leak their fields much more rapidly than thick ones, while thin magnets tend to hold on to them somewhat longer, by as much as a factor of 2. The behavior of the magnetic case is somewhat unintuitive[38] but arises from the fact that while the tangential electric field vanishes at the conducting surface, it is the normal component of the magnetic field that vanishes at this boundary [135].

4.7.4 Tune Shift in the Presence of a Rectangular Boundary of Finite Thickness. In either case, for sufficiently long time, the changing behavior of the wakefields in (4.72-73) amounts to the effect of splitting the series in (4.71) into a truncated sum for short-range wakes and an integral for long-range wakes. The truncation occurs for $\mathrm{k}=\hat{\mathrm{k}}$ where

$$\hat{k} = \frac{\Theta^2}{\pi^2 \delta_0^2} \tag{4.77}$$

$\hat{\mathrm{k}}$ is then representative of the relative time required for the field penetration through the chamber of thickness Θ. Then (4.71) becomes

$$h = \frac{1}{n_b} \sum_{m=1}^{n_b} \sum_{k=0}^{\hat{k}-1} \sqrt{\frac{1}{k + \frac{mS_b}{C}}} + \pi \frac{\delta_0}{\Theta} \int_{\hat{k}}^{\infty} dk \exp\left(-\frac{\pi \delta_0^2 z}{\hat{\mathrm{r}} b \Theta C} \right) \tag{4.78}$$

For b>>Θ the second term dominates and then

$$h \approx \frac{\hat{r} b}{\delta_0} \tag{4.79}$$

However, this is not precisely the case in the Booster magnets, where the thickness vertically of the magnets is around twice the gap size [130]. In this case, the first term contributes nonnegligibly and we may write instead

$$h \approx \frac{\hat{r} b + 2\Theta / \pi}{\delta_0} \tag{4.80}$$

---

[38] At least to the author of this work

The contribution to the tune shift from this quadrupole term can then be obtained by inserting (4.69-71) into (4.64), where the oscillatory nature of the dipole term (4.68) has been assumed to average to zero. The result is as follows.

$$\Delta\nu_{x,y} = \pm\frac{1}{48}\frac{\hat{r}\Xi r_0 L}{\gamma b^2 \nu_{x,y}}\left[1+\frac{2\Theta}{\pi\hat{r}b}\right] \tag{4.81}$$

However, for completeness, the rectangular cross section, not just the vertical parallel plates must be considered. Let $\hat{r}$, b, Θ correspond to the flat boundaries in the vertical plane and $\hat{r}$',b',Θ' to the ones in the horizontal. In this case, then, (4.81) can be extended to include both planes.

$$\Delta\nu_{x,y} = \pm\frac{1}{48}\frac{\Xi r_p L}{\gamma \nu_{x,y}}\left\{\frac{\hat{r}}{b^2}\left[1+\frac{\Theta}{\pi\hat{r}b}\right]-\frac{\hat{r}'}{b'^2}\left[1+\frac{\Theta'}{\pi\hat{r}'b'}\right]\right\} \tag{4.82}$$

We see that (4.81-82) are independent of the skin depth, δ_0. The value of δ_0 determines how quickly the wakes accumulate to their steady-state value, but ultimately it is the thickness of the chamber walls which determines the size of the effect. It is important, however, that the thickness not be too small such that the accumulation occurs rapidly enough that the long-range behavior of the wakefields is not reached (i.e. the time for field leakage must not occur for distances very close to the driving particles). In the case of the Booster, the magnets are several inches thick, so this condition is satisfied.

We estimate this effect in the Booster in what follows, but the assumptions so far leading to the values we shall obtain below are somewhat naïve. A further complication exists because of the laminations from which the magnets are constructed, which modify the behavior of the wakes due to the greatly enhanced surface area such laminations provide. Nonetheless, for now we proceed with a value for (4.82) as a point of comparison. In Table 4.4 the relevant parameters for evaluation of (4.82) are displayed.

Table 4.4. Booster Parameters for the Evaluation of (4.82)

Beam Intensity (Ξ)	5×10^{12}
Lorentz Factor (γ)	1.4
Magnet Half-Apertures (b, b')	2.5 cm, 17 cm (average)
Horizontal or Vertical Tune ($\nu_{x,y}$)	6.8
Magnet Thickness (Θ, Θ')	13 cm, 5.7 cm
'Zotter Ratio' ($\hat{r}, \hat{r}'$)[39]	1, 9.9
Orbit Circumference (C)	471 m
Magnet Fraction (L⁄C)	0.60
Classical Proton Radius (r_p)	1.535×10^{-18} m

From these values we obtain a tune shift of 1.9×10^{-2} for this given intensity (typically about 10 turns of injected beam). This value is similar in magnitude to the ones obtained from the Laslett analysis in Section 4.5. A more useful quantity for our purposes, however, is the so-called 'tune slope,' or the change in tune with intensity. Since (4.82) is linear with intensity Ξ, we obtain

$$\frac{d\nu_{x,y}}{d\Xi} = \pm\frac{1}{48}\frac{r_p L}{\gamma\nu_{x,y}}\left\{\frac{\hat{r}}{b^2}\left[1+\frac{\Theta}{\pi\hat{r}b}\right]-\frac{\hat{r}'}{b'^2}\left[1+\frac{\Theta'}{\pi\hat{r}'b'}\right]\right\} \tag{4.83}$$

For these same parameters in Table 4.4 we obtain a value of $0.004/10^{12}$.

Once again, without accounting for the magnet laminations these values are to be taken with some suspicion and require further explanation. In Chapter 5 these results will

---

[39] These are taken at the outside edge of the chamber.

be compared to tune-shift measurements investigating the relative amounts of dipole and quadrupole impedances present in the Booster cycle near injection, in which context the lamination effect will be more fully discussed.

CHAPTER 5

EXPERIMENTAL DETERMINATION OF THE INTENSITY-DEPENDENT EFFECTS OF THE CUMULATIVE LONG-RANGE WAKE FORCES ON THE PARTICLE TUNES CONSIDERING THE BOOSTER GEOMETRY

5.1 Synopsis

In Chapter 4 the tune shifts due to resistive-wall wakefields in noncircular geometries were introduced. A dipole and a quadrupole term due to the rectangular geometry in the Booster were expected, leading to tune shifts of opposite sign in the two transverse planes, or at the very least, a pair of negative tune shifts, one of which has a positive contribution from a quadrupole wakefield. In Sections 5.2 and 5.3 we present the measurements made to quantify the tune shift predicted from (4.82).

An early study with the beam parameters near a coupling resonance, i.e. a location in tune space where the fractional parts of the vertical and horizontal tunes (ν_y and ν_x) are minimally separated, was performed to quantify the possible effect of intensity on coupling strength.[40] It was observed that, for transverse mode frequencies measured on a signal analyzer, a frequency increase with intensity was observed for one mode and a decrease for the other. The change was not symmetric, with the increase in one mode considerably smaller than the decrease in the other. The total separation, however, was found to be linear with intensity. Originally, the splitting of these modes was thought to be due to the combination of a quadrupole and a dipole wakefield phenomenon for rectangular

---

[40] The nomenclature may be somewhat misleading. Coupling refers to the extent to which the motion in one transverse plane is affects the motion in the other. A coupling resonance is a location in tune space where the effects caused by a finite coupling strength is maximized.

structures as analyzed by Chao et al. [23] and as discussed in Section 4.7. However, the measurement was carried out near such a coupling resonance. The interpretation of the results as a wakefield phenomenon was somewhat suspect since the dynamics of betatron motion is sensitive to other effects in this region of tune space, most importantly the coupling between the transverse planes. Also, the measured normal modes near this resonance are a superposition of the betatron tunes, for which any effects changing the tunes cannot be disentangled without *a priori* knowledge of the natural coupling of the machine [113]. The extent to which proximity to this resonance was important in the dynamics was not apparent. In order to isolate wakefield effects from those due to transverse coupling, a second study to determine the dependence of the betatron tunes on beam intensity was made with the horizontal and vertical tunes well separated.

Results were qualitatively the same, in that a positive tune slope was observed in one plane and a negative slope in the other, with the negative being larger in magnitude than the positive. Quantitatively it was observed that the sum of the magnitudes of the tune slopes in the more recent study was roughly equal to the change in the normal-mode separation versus intensity in the earlier study. The distributions were not significantly different in either case, with the increasing mode having a slightly larger slope in the first study than in the second. The redistribution of the horizontal and vertical wakefield effects caused by the proximity to the resonance with some coupling between the transverse planes was found to be of little importance. These studies are presented below, beginning with the more recent one in Section 5.2. The older study with the beam in the more coupled configuration is detailed in Section 5.3. In Section 5.4 we discuss the problem of the magnet laminations and the possible effects on the results.

5.1.1 Measuring the Betatron Tunes and the Problem of Coupling.

Obtaining the betatron tunes is usually done via a Fourier transform of the position signals from the BPM plates. Often a magnetic or electrostatic device (referred to as a 'kicker' or 'pinger') is needed to enhance the amplitude of beam motion in order to obtain a clear signal of the frequency content in both planes. In an ideal, uncoupled system, the horizontal and vertical betatron frequencies act independently, usually by careful design. In practice, the alignment of elements in an accelerator is never perfect, and motion ostensibly in one transverse direction has a component present in the other. The total effect of these random misalignments leads to a redistribution of the motion in one transverse direction into that of the other. Correction elements, in particular skew-quadrupole magnets, may be utilized to compensate for this, but since correction elements cannot be continuously distributed around the lattice,[41] other effects, related, for example, to intensity and nonlinear optics, make a complete cancellation of coupling-errors by a finite number of correctors a difficult task. In practice, some "natural coupling" then tends to exist. When measuring the transverse oscillation frequencies (i.e. the betatron tunes), what are really observed on a signal analyzer are the so-called normal-mode tunes, where

$$\omega_{\pm}^2 = \frac{1}{2}\left[\nu_h^2 + \nu_v^2 \pm \sqrt{\left(\nu_h^2 - \nu_v^2\right)^2 + 4q_c^4}\,\right] \tag{5.1}$$

$\omega_\pm$ are the upper and lower mode frequencies and ν_h, ν_v are the uncoupled horizontal and vertical tunes.[42] The coupling strength q_c affects the size of the separation of these modes, and how strongly independent horizontal and vertical tunes will be intertwined in these

---

[41] With current technology, anyway.

[42] Horizontal and Vertical are in this case, arbitrary. One may of course swap the labels with no change in the physics.

normal modes. It is thus important to quantify how well one can resolve these tunes from the measurement of the normal modes, given their proximity to each other and the strength of the coupling.

We consider the two limiting cases, namely where the separation of the uncoupled frequencies is either much larger or smaller than the coupling parameter (specifically where $\left|\nu_h^2 - \nu_v^2\right| \gg q_c^2$ or $\left|\nu_h^2 - \nu_v^2\right| \ll q_c^2$). In this case we find, for small and large separation, respectively,

$$\omega_\pm^2 = \left[\frac{\nu_h + \nu_v}{2}\right]^2 + \left[\frac{\nu_h - \nu_v}{2}\right]^2 \pm q_c^2 \tag{5.2}$$

$$\omega_\pm^2 = \begin{bmatrix}\nu_h \\ \nu_v\end{bmatrix}^2 \pm \frac{q_c^4}{\left|\nu_h^2 - \nu_v^2\right|} \tag{5.3}$$

We see that for large frequency separation (5.3) the coupling has little effect on the modes, and the error scales as the square root of the inverse of the squared frequency difference.

Very near the "degenerate" case, where $\nu_h \approx \nu_v = \nu_0$, the two oscillation frequencies become irresolvable from a power-spectrum measurement of these normal modes, and the coupling term is of paramount importance. However, one can verify where the tunes are practically equal. For complete degeneracy the modes reduce to

$$\omega_\pm^2 = \nu_0^2 \pm q_c^2 \tag{5.4}$$

This represents the smallest separation between the normal modes given a particular value of q_c, and its measurement is straightforward. An increase in coupling strength thus leads to an increase in the separation of these modes.

The effect of coupling is then most dramatic near the so-called coupling resonance, where the difference of the fractional part of the betatron tunes vanishes,[43] as in the degenerate case of (5.4). In this regime the normal modes of oscillation, not the independent betatron tunes, completely characterize the motion, and are separated only by the strength of the coupling at this resonance, so long as the coupling is strong enough. Section 5.3 will detail a study under this condition, but in the study described in Section 5.2 it was imperative that the tunes be separated sufficiently such that (5.3) was satisfied.

5.2 Measurement of the Intensity-Dependent Tune Shift in a Lattice with Well-Separated Tunes

The purpose of the study described here was to investigate the existence of a quadrupole-like impedance due to the roughly rectangular magnet geometries in the Booster, in which the tunes in the horizontal and vertical planes would be affected in an opposite sense by these structures, in addition to the familiar dipole wakefield that defocuses in both planes.

5.2.1 Timeline Configuration and Booster Lattice Modification. The control-room event timeline was adjusted to include roughly two Booster study cycle events ($17[44]) per minute, to perform the measurements. Correction quadrupole circuits were varied by changing power-supply currents from nominal values to 3 A of increase in the QL circuits and 1 A in the QS circuits over the first 15 ms of the cycle. This was done to substantially increase the separation between the horizontal and the vertical tunes such that the condition (5.3) was valid. Predicted tune behavior for values of the quadrupole set-

---

[43] This difference resonance is a special case of a class of parametric resonances in an accelerator where the sum or difference of the betatron tunes is some rational number, the integer being the most pronounced.

[44] MCR timeline events are enumerated in hexadecimal format, with a "$" preceding them

tings were obtained with a procedure described by Y. Alexahin, the methods of which are detailed elsewhere [1]. Figure 5.1 taken from the ACNET console shows the change in current for one of the QS (green curve) and one of the QLs (red curve). Resulting tunes were 6.9 in the vertical plane and 6.7 in the horizontal plane when measured near injection. The blue and yellow curves correspond to skew-quadrupole circuits, which were not changed during this study.

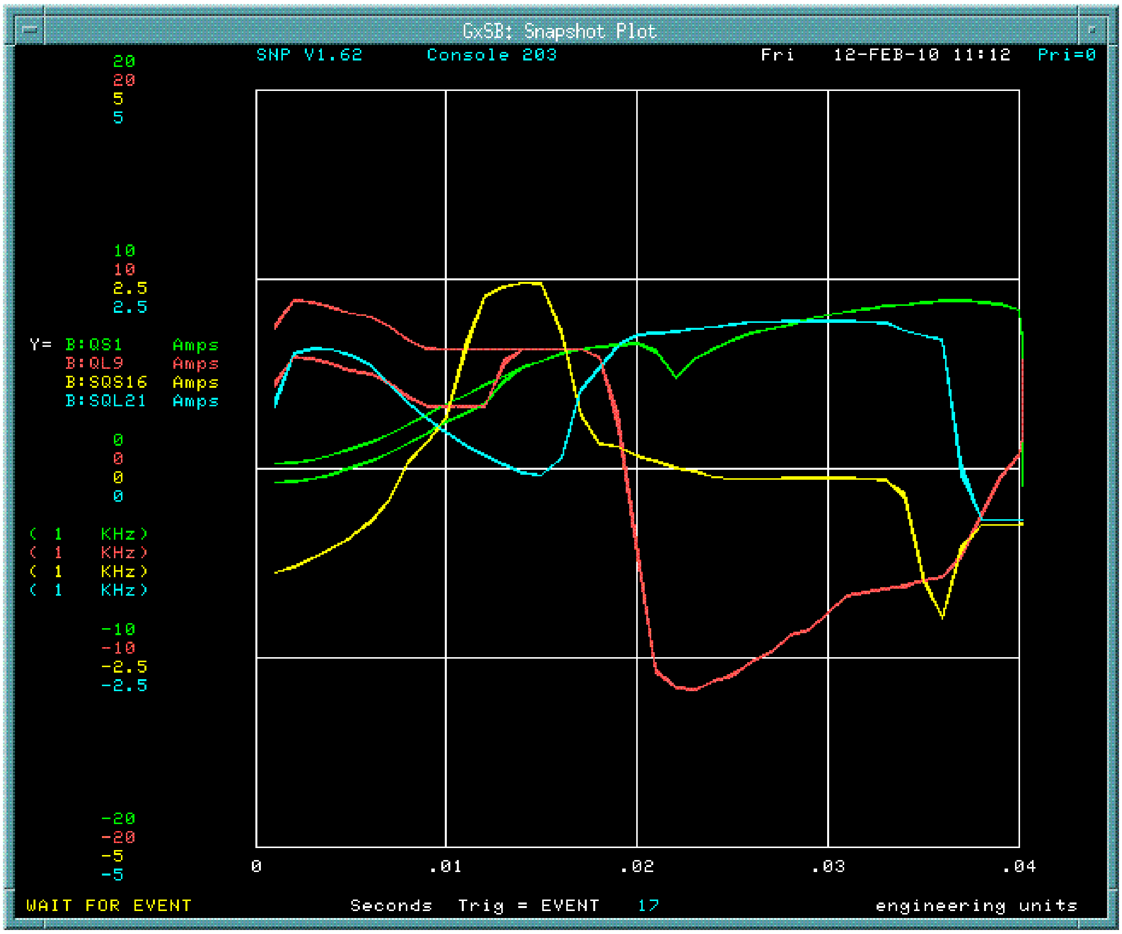

Figure 5.1. Representative Corrector-Current Ramps over the Booster Cycle During the Study (Red for QL, Green for QS, Yellow for SQS, Blue for SQL).

Such a separation was deemed sufficient to render unimportant any coupling in the transverse planes affecting the tune measurement as given in (5.3). While as much separation as possible was preferable, stable operation was difficult to achieve for intensities above 3-4 injected turns for larger changes in the tunes. The vertical kickers were enabled during the study to provide sufficient betatron amplitude for a strong signal to the BPM's, while the horizontal kickers were unavailable for use during the study. Excitation in one plane of motion, however, was frequently sufficient to obtain a measurable response in both planes.

5.2.2 BPM Combining and Tune Measurement. Data were recorded on the ACNET console program B38, written and implemented by B. Marsh, which obtains all BPM positions and performs a power-spectrum (i.e. Fourier) analysis on the signals turn-by-turn, providing a complete picture of the time evolution of the frequency content in each plane throughout the cycle. BPM signals were calibrated and combined using a variation of the Mais-Ripken parameterization [86] according to methods prescribed by Alexahin and Gianfelice-Wendt [3]. It was suggested during the processing of the BPM-signal data to obtain optimal resolution that a continuous Fourier transform [2], sampled over ten turns, be applied to obtain tune values with maximal resolution in this window.

Typical readouts of the BPM-combined power contour for the horizontal and vertical planes are given in Figures 5.2 and 5.3 for ten injected turns, or around 4.7×10^{12} particles. Frequency-content amplitude is displayed in a false-color scheme, with magenta representing the strongest response and green the weakest. Turquoise represents intermediate values. Spectrum data were saved for offline processing as well. Figures 5.2 and 5.3 shows results from the vertical and horizontal BPMs, respectively.

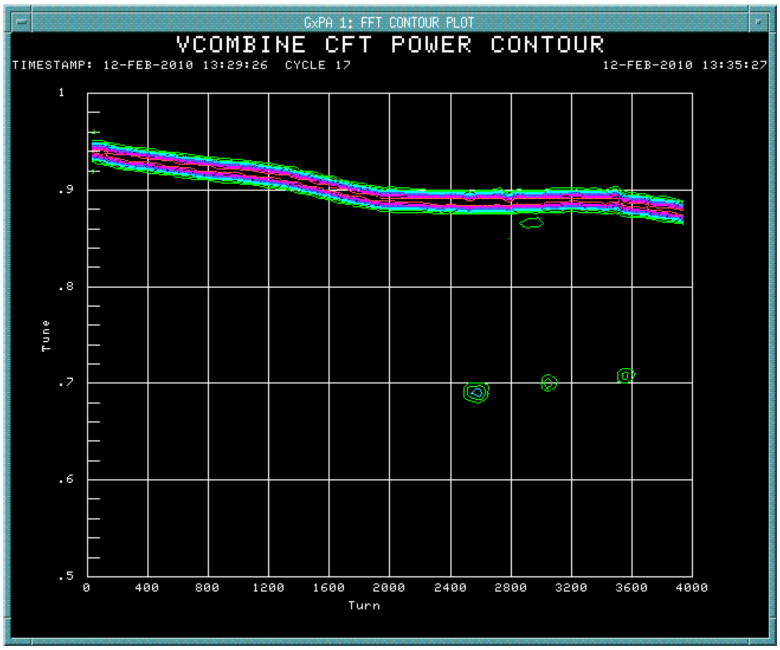

Figure 5.2 Vertical Tunes Obtained by Continuous Fourier Transform of Beam Position Information from the 100 BPMs in the Booster. Stronger Responses are Given by the Magenta Coloring, and Weakest by the Green Coloring.

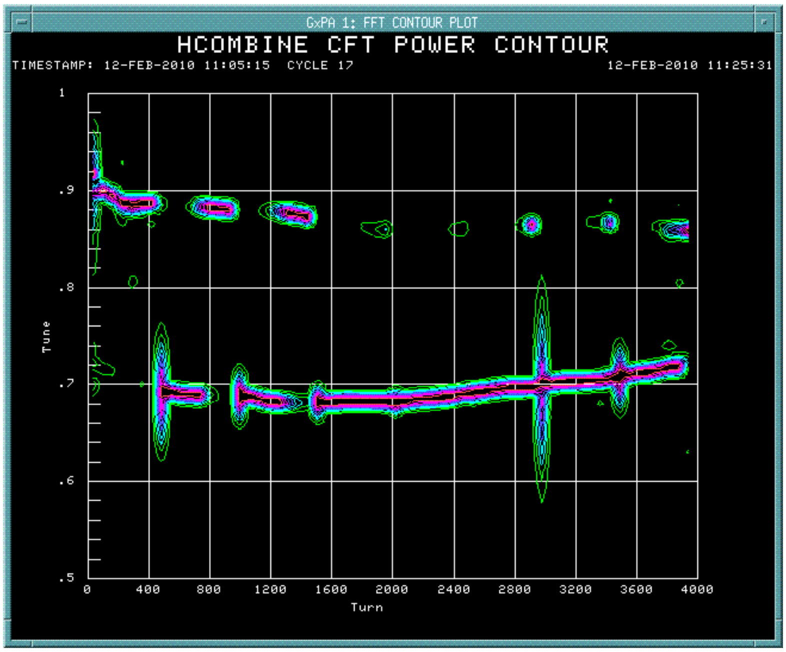

Figure 5.3 Horizontal Tunes Obtained by Continuous Fourier Transform of Beam Position Information from the 100 BPMs in the Booster. Stronger Responses are Given by the Magenta Coloring, and Weakest by the Green Coloring.

Figure 5.3 indicates that some vertical response is present in the horizontal plane. The lack of a horizontal kicker was responsible. The horizontal amplitude was only enhanced from the residual effect from the vertical plane (kicker plus some coupling).

Beam intensity was varied from 0.9×10^{12} to 6.8×10^{12} particles at injection in increments of roughly 0.45×10^{12}. Intensity was measured and recorded for each data set using the CHG0 intensity monitor. Figure 5.4 shows intensities (green curves) and beam loss (red curves) taken over the entire Booster cycle for 0.9×10^{12} to 4.2×10^{12} particles (2-9 turns of injected beam) and 4.75×10^{12} to 6.8×10^{12} (10-15 turns of injected beam), respectively.

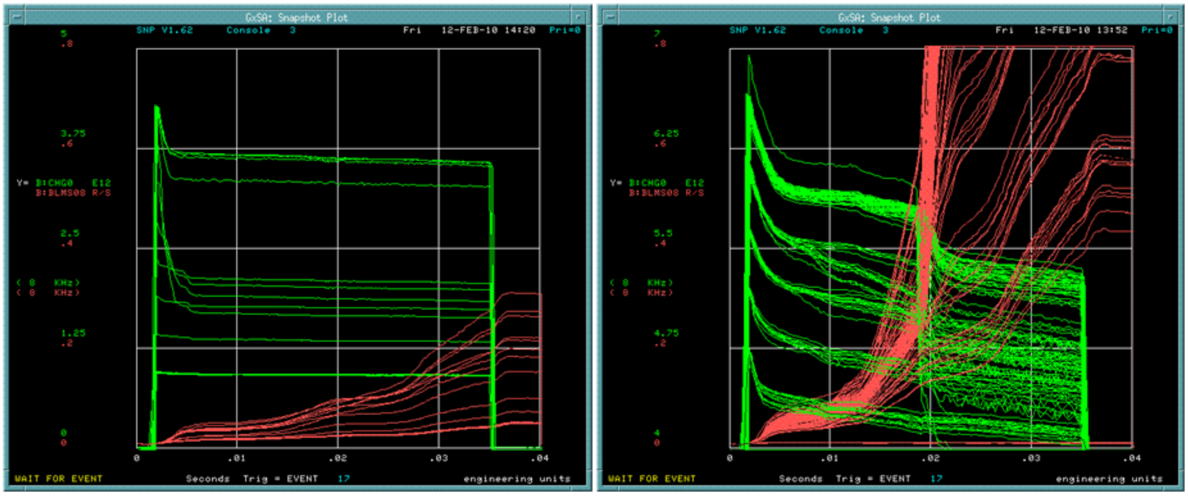

Figure 5.4. Intensity (Green Curves) and Loss Values (Red Curves) from ACNET Console for 0.9×10^{12} to 4.2×10^{12} Particles (left) and 4.75×10^{12} to 6.8×10^{12} Particles (right) over the Entire Booster Cycle.

The various intensity increases can be observed from the step-by-step increments at injection. The "smearing" of the curves at higher intensities represents the repeated injections at a particular intensity over the dozen or so $17 events. In some cases several cycles passed before the instrumentation was ready for data-taking, and also several cycles passed during which the BPM-combination algorithm was obtaining the power spectrum. At the lower intensities shown in Figure 5.4, a beam-permit switch was actively used to minimize the number of cycles where data was not being analyzed, providing the clean-looking single curves as seen. A peculiar issue during these measurements arose at moderate intensities (6-8 turns injected), where loss was surprisingly large relative to that at higher intensities. Apparently the Booster was tuned well to high intensities during this operation, sacrificing stability at moderate values. The lowest intensities (2-5 turns injected), easily within the machine acceptance, seldom pose a problem under any circumstance. The stability at high intensities was beneficial to the experiment even with some loss of resolution in the intermediate range.

5.2.3 Tune dependence on Intensity. The tune shift as a function of intensity was evaluated at three different times near injection, one very near injection at 33 turns, another further from injection, at the onset of acceleration, after paraphasing was complete at 545 turns, and one later in the cycle, during acceleration, at 1633 turns. These values correspond to 2, 3, and 5.5 ms on the horizontal axis in Figure 5.4. Intensities were obtained from the curves at these times. The need for the last point at 1633 turns was to verify that the cumulative quadrupole wake discussed in Section 4.7 had indeed reached a steady state by 545 turns. These particular values of the turns corresponded to times in the cycle where the console program B38 produced output for every intensity. The consistency of the output depended on the value of the kicker-threshold setting. Fourier-transforms below a certain amplitude would be rejected, in this case those below 20% of the maximal signal amplitude at a particular A lower value was able to yield data more frequently but also produced more noise in the signal, especially from the other transverse plane of motion. The chosen values were a compromise in which the spacing between subsequent samples in the cycles is sufficient without obscuring the contour spectrum with excessive noise.

Figures 5.5 and 5.6 show the horizontal and vertical tune dependence on intensity for these representative locations (in time) within the cycle. While the tunes change during the cycle for all intensities, the slope of the intensity dependence at any point is practically independent of the starting locations. In the vertical plane we observe a defocusing effect with increasing intensity for all three samples of cycle time. The familiar dipole wakefield is capable of explaining this, but the increase in magnitude of the slope of the shifts observed for the points at 545 and 1633 turns is indicative of the quadrupole effect accumulating as predicted by Chao et al [24]. In the horizontal plane, ignoring the spread in the set of data earliest in the cycle, we observe a small but positive tune shift, which, if the dipole wakefield were the only effect, would not occur. This suggests that a quadrupole wakefield is indeed present and is of similar magnitude to the dipole effect, augmenting the defocusing dipole-wakefield tune shift in the vertical plane and competing with it in the horizontal plane.

The jitter in the horizontal plane can be explained by momentum dispersion and the effect of the feedback system for momentum control. Increasing intensity has the potential to change the orbit of the beam if the feedback systems are insufficient to control beams with greater particle density as readily. This has the potential to "fool" the BPM system into obtaining different betatron tunes than expected because the reference orbit is not properly located [93]. Physically this occurs when the fractional momentum offset

Δp⁄p changes. To verify the orbit control, the momentum offset of the beam was measured using the ACNET Booster Turn-by-Turn orbit monitor, B40, which calculates the absolute and relative momentum offset of the beam given the known dispersion function values at the location of the BPM's.

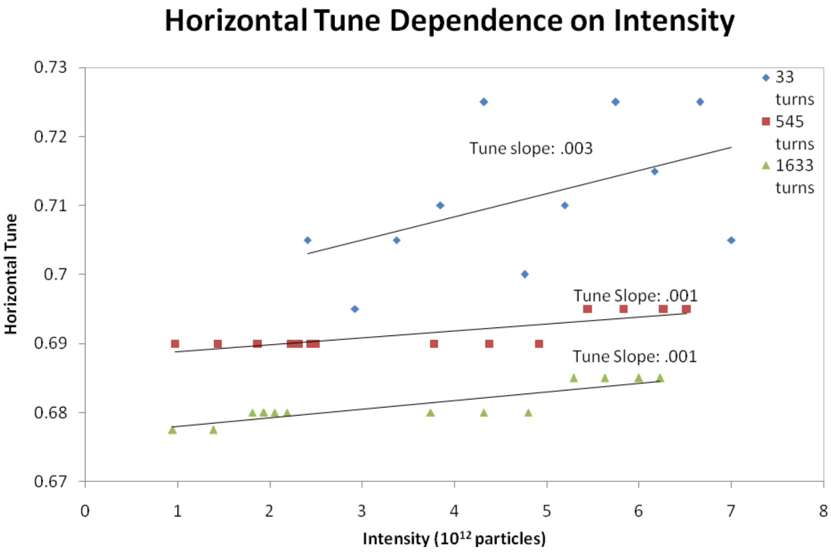

Figure 5.5. Dependence of Horizontal Tune on Beam Intensity for Various Times in the Cycle near Injection. Color Scheme for the Different Turns is Specified in the Legend.

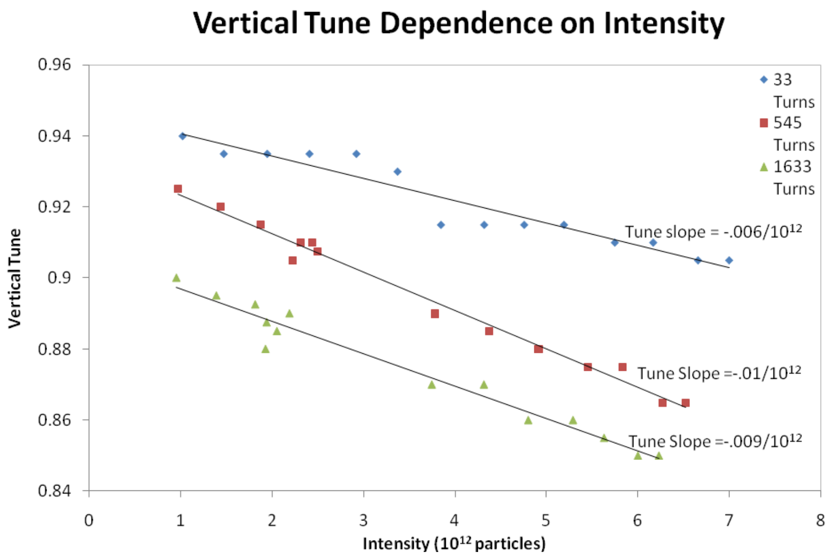

Figure 5.6. Dependence of Vertical Tune on Beam Intensity for Various Times in the cycle near Injection. Color Scheme for the Different Turns is Specified in the Legend.

The values from B40 at different locations in the cycle between 1 turn and 2450 turns after injection at various intensities are presented in Figure 5.7.

We observe that, with the exception of precisely after injection, no detectable change in the momentum offset of the orbit is observed. At injection, it is reasonable to assume that the increase in the momentum offset was causing the response in the feed-back systems, resulting in the observed horizontal tune jitter. It should be noted that the vertical plane does not show this behavior, since there is no momentum dispersion in the vertical plane.

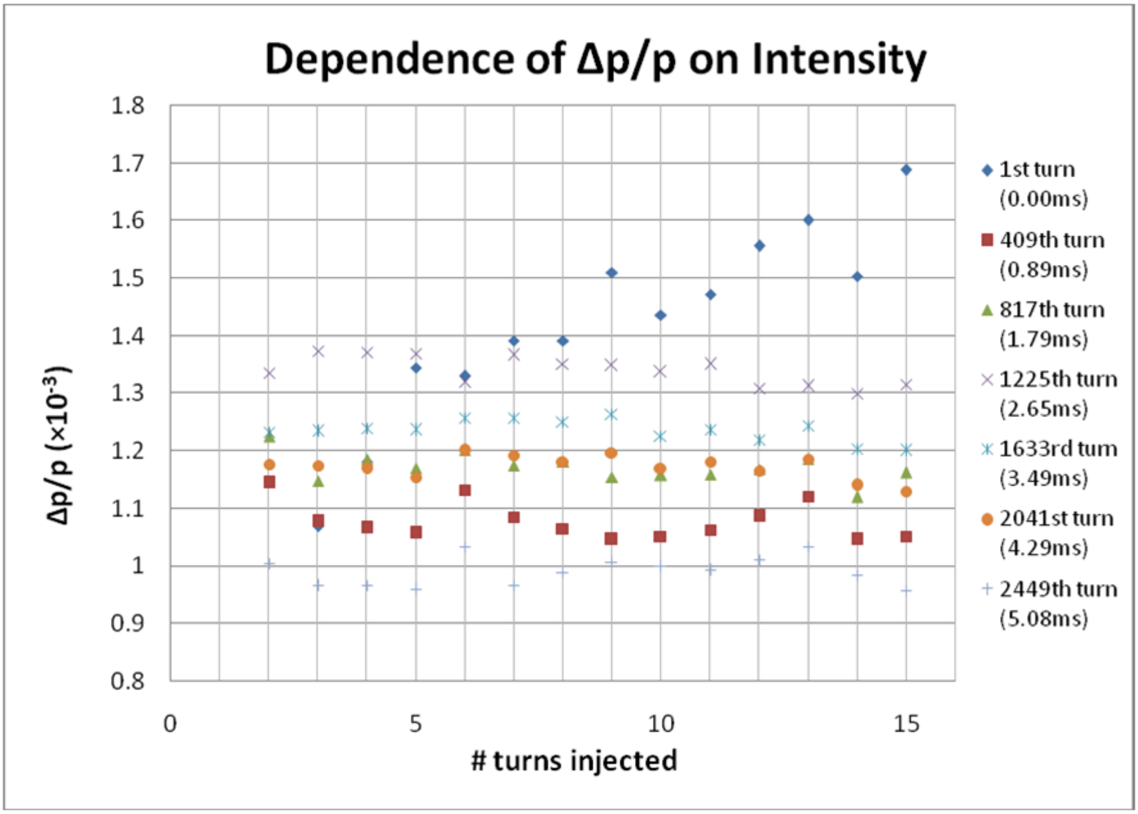

Figure 5.7 Dependence of Momentum Spread (Δp/p) on Intensity for Various Times within the First 5ms after Injection. Coloring Scheme is Provided in the Legend. Turn Number and Time Correspond to after the Completion of Injection.

5.3 Measurements of the Intensity Dependence of the Normal-Mode Tunes near a Coupling Resonance

In this section we provide results from the earlier study, of intensity-dependent tune shift for a beam near a coupling resonance. In normal operation the Booster is run with some transverse coupling. Experimentally it has been observed that to some degree this enhances beam stability at higher intensities. However, for the purpose of obtaining the tune dependence as a function of intensity it was imperative that the planes be as minimally coupled as reasonably achievable. As shown in (5.3), for sufficiently large differences in the horizontal and vertical tunes the coupling has little effect on the normal modes, since the difference between the modes and the betatron tunes scales as the inverse of the squared-frequency-difference. In this first study of the intensity dependence of the mode frequencies, the transverse planes were as minimally coupled as reasonably achievable by minimizing the coupling directly by varying the current in the skew-quadrupoles with the mode separation near the degeneracy condition given in (5.4).

5.3.1. Procedure for Obtaining Mode Separation near Coupling Resonance, and Results. At the lowest detectable intensity (two turns of injected beam, or around 1.0×10^{12} particles), horizontally and vertically focusing quadrupole strengths were manually varied to find a minimal horizontal and vertical tune separation within practical limits near the degeneracy condition (5.4) for which the normal-mode frequencies were obtainable. Actual values of the horizontal and vertical tunes were still maintained somewhere in the vicinity of 6.7 to 6.8, near the nominal Booster values, and away from any destructive resonances. The tune separation in any case was obtained from FFT of turn-by-turn readouts from the console program B40. During the study, the separation was in the vicinity of 0.05, and no larger than 0.1.

The skew-quadrupole field strengths were then varied systematically with circuits whose currents were varied from -1.0 A to 1.0 A in increments of 0.1 A using the older correctors installed prior to 2007. The mode frequencies were obtained for each quadrupole setting near turn 1000 in the cycle using pickups attached to the Booster BPMs, interfaced to a signal analyzer (VSA 89441A). The skew-quadrupoles affected the extent to which the motions of the horizontal and vertical planes are coupled, so differing skew-quadrupole fields necessarily lead to different mode separations. When a minimal separation was obtained initially, the skew-quadrupole settings at this tune configuration were recorded, as a central value near which a similar degenerate condition at higher intensities would lie. We note that in order to maximally decouple an accelerator, an iterative, often lengthy procedure of tweaking the settings of various skew-quadrupoles possessing different betatron phase advances is necessary. This was not performed. The skew-quadrupoles did not have independent control, but were powered in groups corresponding to the set of correctors in the short and long drift sections. So while the coupling was reduced using this manual routine, it was not eliminated.

The scan was repeated for five different intensities, using 2, 3, 4, 5, and 8 turns of injected beam (one turn of injection corresponds roughly to 5×10^{10} injected particles before acceleration losses). The results are shown in Figure 5.8. The horizontal axis represents the value of the skew-quadrupole current, and the vertical axis represents the fractional part of the measured mode frequency (or normal-mode tune). Mode frequencies are divided into 'upper' and 'lower' regions, with the upper mode having the higher value and the concave-up shape with differing skew-quadrupole settings.

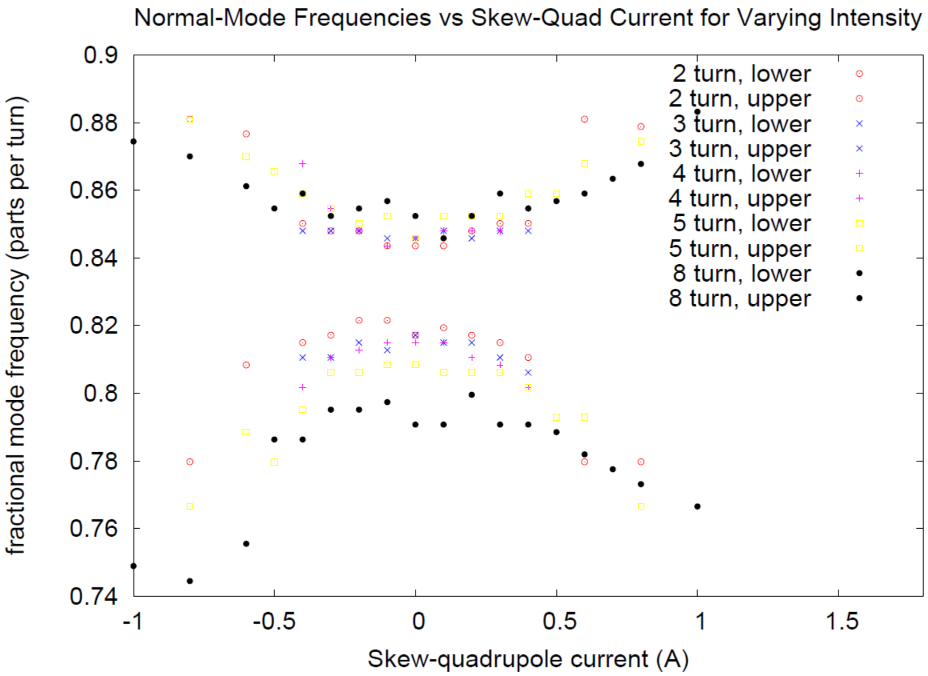

Figure 5.8. Fractional Mode Frequency for Varying Values of the Skew-Quadrupole Corrector Current at Different Intensities. Points for a Given Intensity are Colored According to the Legend in the Upper-Right Corner.

We see a splitting of the upper and lower modes which increases with intensity. One interesting feature is that the splitting is not symmetric with respect to the zero-intensity baseline. The upper-mode frequency increases much less rapidly with intensity than the lower-mode frequency decreases. The minimal mode separation for given intensities is plotted in Figure 5.9, along with a linear fit, providing a 'separation slope' for the mode-frequency intensity dependence, as well as a zero-intensity-limit coupling value corresponding to the amount of coupling present in our crude coupling-minimization effort, assuming the trend is linear to this limit. Some jitter was present in the scan. To compensate for this, individual values of the splitting for each intensity were obtained from the average including the point to the left and the right of the measured minimum, where the shape of the scans was still relatively flat and the frequencies of the measured normal modes roughly the same.

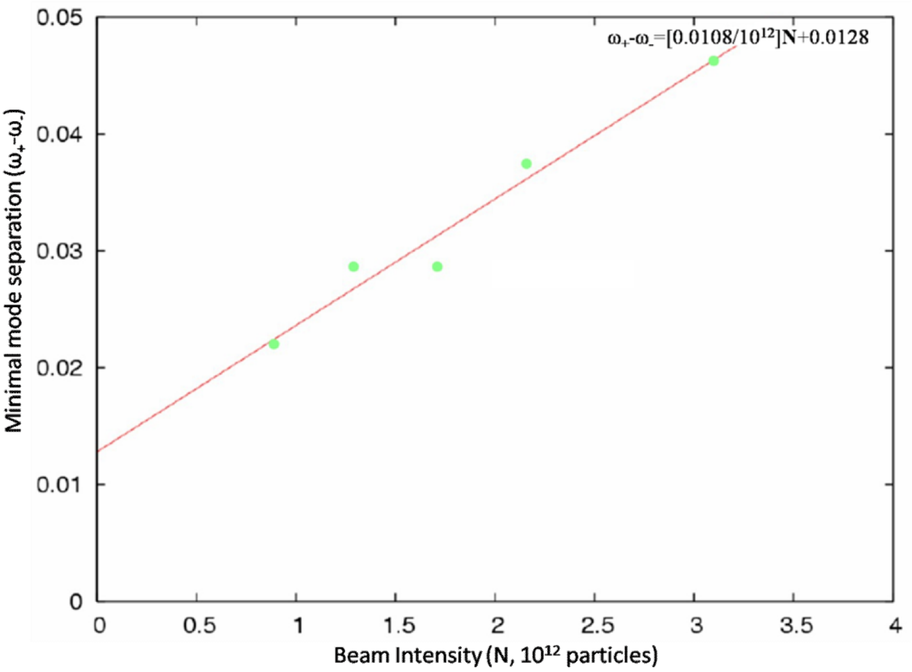

Figure 5.9. Points of Average Minimal Mode Separation (green) and Corresponding Linear Fit (red).

5.3.2. Interpretation of the Data Near the Coupling Resonance. While the coupling was minimized as much as practically possible during the study by varying the skew-quadrupoles, the lattice configuration was left near the difference resonance. The original goal was to better understand the role of space charge in coupling of the horizontal and vertical transverse motion. However, the analysis showed a tune dependence well-matched to published results of intensity-dependent wakefield effects; in particular showing the signature of a quadrupole wake effect arising from an asymmetric beam pipe. However, a clear conclusion could not be drawn, since both wakefield and coupling effects could have been be responsible for the observed trends. So, a second study was done with the tunes decoupled, in order to separate these possible causes. As will be seen, the tune shift slopes at the coupling resonance are consistent with those observed when the tunes were decoupled.

Since the separation is nearly equal to the sum of the absolute tune slopes in Figures 5.5-5.6, and the same qualitative trend is observed (i.e. a combination of a completely downward shift for one mode and seeming competition of an upward and downward shift of the other), we expect that the dipole/quadrupole wakefield observed in the more recent study explains the behavior. To verify this, we decompose the absolute separation in Figure 5.9 into the relative shifts for the upper and lower modes. These are shown in Figures 5.10 and 5.11. As in Figure 5.9, the points were averaged with the adjacent ones to the left and right of the minimum. The lower mode has a similar tune slope to the vertical measurements in Figure 5.6, and the upper mode behaves qualitatively like the horizontal tune in Figure 5.5, though its intensity slope is larger by a factor of four.

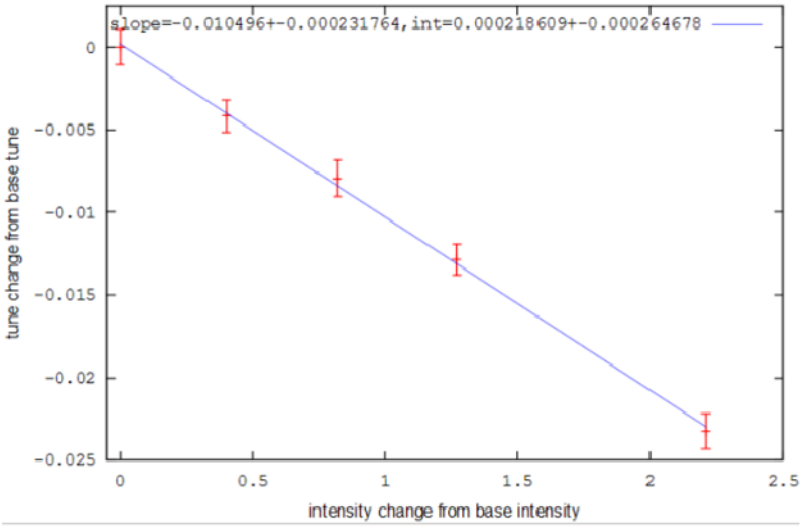

Figure 5.10. Decomposition of Intensity Dependence of Upper Mode from Figure 5.8. Points are Shown in Red and Linear Fit in Blue.

Coupling may have played some role in redistributing some of the horizontal and vertical motions into the observed mode shifts, but the precision (or lack thereof) in the measurement was more likely the cause. The resulting tune shift in the horizontal plane (observed in the lower mode), with a focusing and defocusing term canceling each other, was relatively small to begin with, so any absolute imprecision in the measured lower mode frequency was made more prominent buy this cancelation.

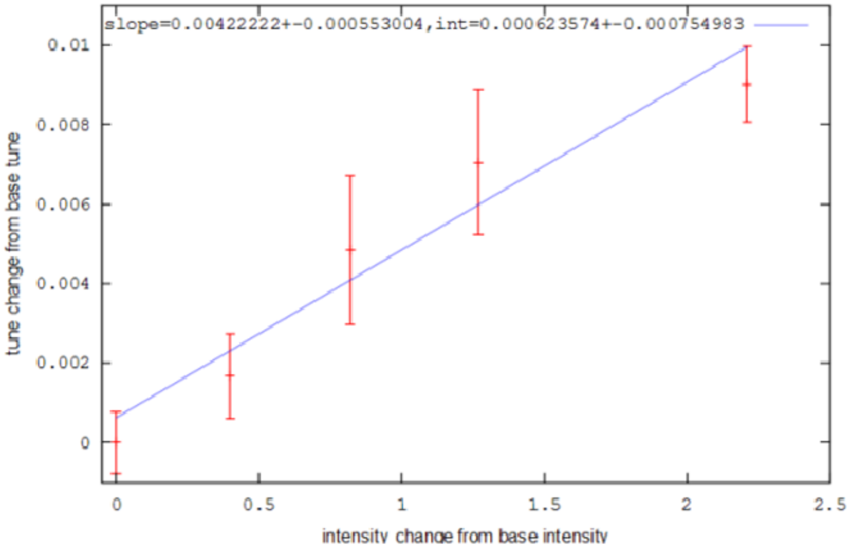

Figure 5.11. Decomposition of Intensity Dependence of Lower Mode from Figure 5.8. Points are Shown in Red and Linear Fit in Blue.

In any case, comparing the numbers from the two studies, reasonable agreement is obtained, suggesting that, despite the much greater proximity of the tunes, the effect of the coupling did not play a substantial role.

5.4 The Effect of the Laminations on the Wakefield Behavior

Up to this point, the analysis been done with structures of solid material with contiguous surface areas. However, the magnets in the Booster are composed of longitudinally stacked, electrically separated laminations. Laminated magnets, in addition to providing ease of fabrication, are used to minimize the effect of eddy currents, which decrease the effective field strength and can lead to substantial power losses due to Joule heating from the resistive material. In the Booster, the laminations make possible (or more efficient) its rapid-cycling capability. Since the currents are more or less confined to individual laminations, and the magnetic-flux lines associated with these eddy currents must of course close, adjacent flux lines tend to cancel each other, suppressing these heating and field-strength-attenuation phenomena. However, the same phenomenon mitigating these losses and effective-field attenuation has been shown to measurably augment the resistive-wall impedance on the passing particle beam. We discuss these effects in this section and modify the analysis to account for this, after which the data in Section 4.2 will be compared to the modified analytical predictions.

Qualitatively, the much larger surface area of the many laminations over that of a solid magnet leads to problems whit high-intensity beams when wakefields are taken into account. Field from the passing beam produces surface charges and currents far in excess of what would normally be observed for a thick, solid magnet of a certain skin depth wherein the field can penetrate. Quantitatively, the problem is quite complicated. The original analysis was done by Snowdon [116] and Rugierro [107,108] and later by Gluckstern [54] and Ng [91] for the energy loss from the longitudinal motion in the presence of these laminations. Systematic measurement of the coupling impedance from the laminated magnets was done initially by Shafer [112] and later by Crisp and Fellenz [42] and also by Lebedev [78]. While numerical predictions differ somewhat depending on models and frequency ranges, it has been shown that that the electrical separations of the laminations (the gaps) contribute to the impedance at least as substantially as the laminations themselves in some frequency ranges, and augment the effective relative permeability in any case. In particular, the wakefield dependence on frequency is modified by the extra surface area for low frequencies,[45] while at high frequencies the behavior of the frequency response of the impedance is changed by the resulting displacement current [21, 85]. At low frequencies, where the oscillation wavelength of the beam is much larger than the skin depth which in turn is much larger than the lamination thickness, the laminations behave more like a continuous magnet with a considerably larger effective surface area. At high frequencies, where the skin depth is comparable to or smaller than the lamination thickness, the layered structure becomes the dominant feature in describing the dynamics near the leading particles, and the instantaneous response is not only larger but extends further to trailing particles (to within meters rather than fractions of millimeters).

5.4.1. Augmentation of the Dipole Wakefield. We are interested in the effect of the laminations on the impedance in both the low-frequency and high-frequency regimes. It has been estimated that the laminations magnify the effect of the transverse impedance by a factor on the order of 10^2 [79]. For the dipole-wakefield term, where the average effect tends to zero from successive bunches, the instantaneous[46] effect (or high-frequency content) on the beam is important. From (4.43) the tune shift on a particle at the edge of a rigid, uniform bunch with parameters listed in Table 4.3 was 1.3×10^{-4}. At the given intensity (relative to a zero-intensity limit), a tune slope of $3.1 \times 10^{-5}/10^{12}$ is obtained. This is

---

[45] The effect is similar to the way a stack of radiative fins improves heat dissipation compared to a solid metal block

[46] By 'instantaneous' we mean several turns at most.

very small compared to the observed tune slopes from the cumulative quadrupole wake. Experimentally, negative tune shifts simultaneously in both planes have been observed very near to injection (i.e. before possible accumulation of the quadrupole term) which are much larger than this [78].

It has been discussed by Burov [78] that in the frequency regime of interest the magnetic permeability is augmented by a factor α_{lam}, given by

$$\alpha_{lam} = \frac{2b}{d_{lam}} \tag{5.5}$$

where b is the chamber half-aperture and d_{lam} is the average lamination thickness. The actual relative permeability, which is normally close to unity otherwise, also plays a significant role, since the magnets are constructed from steel. The impedance and corresponding wakes given in (4.72-73) are modified in the presence of ferromagnetic materials by making the substitutions

$$W \rightarrow \mu W \tag{5.6}$$

$$\delta_0 \rightarrow \frac{1}{\sqrt{\mu}} \delta_0 \tag{5.7}$$

where μ is the relative permeability of the material. For the dipole effect, within proximity to the driving particle over shorter distances, the wakefield (hence the wake force, and hence the tune shift) is proportional to δ_0, and ultimately to the square root of μ. The relevant parameters are summarized in Table 5.1, from which we obtain an instantaneous dipole-wakefield magnification of around 90, and a corresponding predicted tune slope of $2.8 \times 10^{-3}/10^{12}$.

Table 5.1. Parameters for Calculation of Dipole-Wakefield Modification in the Presence of Laminations

Magnet Half-Apertures (b)	2.5 cm
Lamination Thickness (d_{lam})	640 μm
Augmentation Factor (α_{lam})	78
Relative Permeability of Steel (μ)	~100
Dipole Wakefield Multiplier $(\mu\alpha_{lam})^{1/2}$	90
Tune Slope of Augmented Wakefield	$2.8 \times 10^{-3}/10^{12}$

This value is in keeping with what we observe from Figures 5.5 and 5.6, (using the data nearest to injection), within a factor of two or three, with tune slopes per 10^{12} particles on the order of 10^{-2} to 10^{-3}. The original, unaugmented tune-shift value in Section 4.6.6 gave a tune slope of $3.1 \times 10^{-5}/10^{12}$, using the nominal intensity responsible for the shift, and was based on the assumption of a round cylindrical pipe, so exact agreement with data is not expected. The understanding of the detailed behavior of the wakefields in the presence of laminations is by no means a trivial problem, so order-of-magnitude agreement alone is encouraging. We shall separate the actual contributions from the dipole and quadrupole wakes in Section 5.5, using other tune-shift data obtained near injection from independent measurements.

5.4.2. Augmentation of the Quadrupole Wakefield. The effect of the laminations on the quadrupole wake is more subtle. From (4.72-73) we observe that at short distances the wake is proportional to δ, while for large distances it depends on δ^2. So for short distances from the leading particle the wakes are still augmented by the square root of μ. For large distances, however, the squared dependence of δ cancels the effect of the relative permeability in the numerator, and the resulting tune shift is still governed by (4.82). In the long-range regime, the effect on the betatron tunes is the same. The modification from the laminations arises in the time required for the accumulation of the wakes to reach the steady state. Oscillation growth rates may be more strongly affected over the longer accumulation time but the resulting tune shift will be the same.

Qualitatively it stands to reason that the accumulation of the quadrupole-wakefield effect should be prolonged. The field will still leak through the thin, stacked laminations eventually, but the overall leakage behavior may be different since for a large, solid magnet the longitudinal size of the material is comparable to the betatron oscillation wavelength of the passing bunches causing the disturbance, while a single lamination is three to four orders of magnitude smaller. Quantitatively, however, it is not clear what the magnitude of this delay should be, but preliminary analytical predictions by Macridin show that the very-long-range effects are smaller in magnitude than the no-lamination case, but diminish somewhat more slowly. The short-range effect (within a few meters) is large but oscillatory, tending to cancel over this region [85]. Investigation of the precise magnitude of this effect will likely require simulations in future work.

5.4.3. Separation of dipole and quadrupole terms. Given the effect on the tunes due to the laminations, we now seek to isolate the contributions from the dipole and quadrupole terms. In Figures 5.5 and 5.6, tune slopes are obtained very early in the cycle (33 turns), and several hundred turns later (545, 1633 turns). If we assume the dipole wakefield is the dominant contributor near injection, any change in the slope later in the cycle may be attributed to the quadrupole effect. However, while this was observed in the vertical plane, the horizontal data near injection were inadequate to discern this behavior.

Because the dipole wakefield leads to a defocusing in both planes, while the quadrupole wake produces a focusing effect, it is also tempting to consider the sum and difference of the horizontal and vertical tune slopes at any point in the cycle. The difference would isolate the quadrupole term and the sum would yield the dipole term. In general, however, no reason exists for the tune shift from the dipole wakefield to be identical in both planes, so while order-of-magnitude calculations may be done, this trick will not suffice for more precise determination. To verify the predictions of the quadrupole tune slope from (4.83) and Table 4.4, we rely on independent data from a previous impedance study by Lebedev [78]. Table 5.2 reproduces the tunes obtained for nominal and half of nominal intensities from 30 to 60 turns after injection. Since the quadrupole wake accumulates over a few hundred turns, during the initial 30 turns it was assumed that it was not yet a significant factor. Tune slopes obtained from these data are $2.3 \times 10^{-3}/10^{12}$ in the horizontal plane and $5.5 \times 10^{-3}/10^{12}$ in the vertical plane.

Table 5.2. Measured Horizontal and Vertical Tunes near Injection for Nominal and Half-Nominal Booster Intensities. (Courtesy V. Lebedev, A. Burov, W. Pellico, X. Yang, 2006)

Intensity (10^{12} particles)	2.3	4.5
Horizontal Tune (ν_x)	6.830	6.825
Vertical Tune (ν_y)	6.831	6.819

These are of the same order of magnitude as the value from the data in Table 5.1 in the previous section, suggesting that the lamination magnification factor α_{lam} is indeed on the order of 100 (90 was what was calculated). Also, the vertical tune slope agrees experimentally with our value of $6 \times 10^{-3}/10^{12}$ presented in Figure 5.6, for the case near injection. We then utilize these numbers as representative of the dipole-wakefield tune slope, relying on them especially for the horizontal case.

The data in Figures 5.5 and 5.6, in addition to the slopes obtained from the values in Table 5.2, are compared with predictions made in this and the previous chapter. The comparisons are summarized in Table 5.3.

Table 5.3. Predicted and Measured Contributions from Quadrupole and Dipole Wakes on Betatron Tune-Slopes Versus Intensity

Type of Wake a) near injection b) far from injection	Dipole (a,b)	Quadrupole (a)	Quadrupole (b)
Predicted Horizontal Tune Slope ($10^{-3}/10^{12}$)	-2.8	~0	4
Predicted Vertical Tune Slope ($10^{-3}/10^{12}$)	-2.8	~0	-4
Observed Horizontal Tune Slope ($10^{-3}/10^{12}$)	-2.3	not observed	3.3
Observed Vertical Tune Slope ($10^{-3}/10^{12}$)	-5.5	-0.5	-4.5

Horizontal and vertical tune slopes are divided into the components corresponding the dipole and quadrupole wakefields. The observed dipole-wake slopes are obtained from the data in Table 5.2. The observed quadrupole slopes are calculated by subtracting the slopes obtained from Table 5.2 from the fits obtained in Figures 5.5 and 5.6.

Predicted and observed results of the quadrupole effect agree to within 10%. The cumulative effect seems to occur within 500 turns (as an experimental upper limit). For the dipole-wake effect, initially the assumption of a cylinder with a radius of 4cm was used. No attempt was made to account for the various Booster elements of differing geometry, in particular the rectangular magnets. The majority of the discrepancy in the vertical plane is most likely because the half-aperture of the magnetic pole faces is smaller than 4 cm, in fact closer to 2.5 cm in both the focusing and defocusing pole tips.

Considering the differing geometries present in the Booster, the precision in the factors contributing to the magnification effects from the laminations (such as the magnetic permeability), and the relative crudeness of the rigid-bunch model initially used, the dipole tune-shift calculations are considered adequate. No attempt was made to further refine the values. We content ourselves with the fact that the experimental data for dipole tune shifts, when subtracted from the total tune slope later in the cycle, yield a tune shift from the quadrupole effect which agrees well with its predicted value.

CHAPTER 6

MEASUREMENT OF THE INCOHERENT TUNE SHIFT AND STOPBAND WIDTH THROUGH RESONANT EXTINCTION, AND AN ASSESSMENT OF THE SPACE-CHARGE TUNE SHIFT FROM THE REALISTIC BEAM DISTRIBUTION

6.1 Synopsis

The data in Chapter 5, and much of the theory dealing with it in Chapter 4, centered around the effect of the surroundings on the beam. This came in the form of electromagnetic wakefields, where leading particles deposited some of their field energy in passing through the vacuum chamber in such a way as to affect trailing particles. Both the geometry of the chamber as well as the multipole distribution of the beam were shown to play a role in the perturbation on the trailing particles. This effect was considered coherent in nature, because the particles in the bunch were more or less affected uniformly by these wakefields. A study of the dynamics of the beam limiting particle intensity should include a discussion of the incoherent motion of the particles about the centroid, in particular the effects due to space charge within the bunch.

In this Chapter we attempt to realistically quantify the space charge effect in the Booster. In Section 4.5 an estimate of the relative importance of the space-charge tune shift to the image fields from the Laslett tune shift was given, where near injection the maximal space-charge tune shift was larger by a factor of 50. It was shown from the predictions in Chapter 4 and the results in Chapter 5 that the impedance effects, which were extensions of the image-charge analysis, coupled with the presence of the laminations were substantially larger than what was calculated using the simple dipole analysis in a round, resistive chamber.

Similarly, in Section 6.2 we present a more refined analysis over what was given in Section 4.5, using a nonuniform distribution without the assumption of a rigid bunch. In Section 6.3 we detail a study in which the tune-spread dependence on intensity was obtained, whose results can be used to place an upper limit on the direct space-charge effect on individual particles. The space-charge tune shift is shown to be less substantial than predicted in Section 4.5, and in fact is on the same order of magnitude as the coherent tune shifts of the resistive-wall wakefields quantified in Chapters 4 and 5.

6.2 The Effect of Incoherent Motion on Transverse Beam Stability

Transverse stability of coherent motion depends in part on the proximity of the centroid tune to certain resonances, in particular the half-integer and third-integer, as well as some parametric resonances, especially where the sum of the fractional parts of the horizontal and vertical tunes is equal to unity. The individual particle tunes may be distributed about some central value. Some particles may be closer to such a resonance, and hence their motion can lead to beam growth or beam loss in the presence of gradient errors. It was pointed out by Baartman [12], however, that individual particles lying on or near a resonance may itself not be a sufficient condition for particle loss since these particles do not forever maintain an oscillation frequency (tune) near the resonance. As a particle moves through the distribution, its tune will vary depending on the space-charge field affecting it. When enough particles lie in the vicinity of the resonance long enough, however, substantial beam loss can be an issue because possible effects shifting the particle tunes away from the resonance (however much they may be) cannot compensate statistically for all of the near-resonance particles at once. This region in tune space is often referred to as the resonant 'stopband' and the width in this tune space as the stopband width. The study presented in Section 6.3 relies on measurement of the resonant stopband width for various intensities to obtain a measure of the particle tune spread.

The intensity limitations of an accelerator can be affected by the space-charge tune shift, but the size of the shift must take into account both this stopband width as well as a variation of the beam size and density profile under increasing intensity. In Section 6.2.1 we discuss the latter, and how the estimated intensity limitations based on the uniform, fixed-dimensional beam are often too conservative.

6.2.1 Single-Particle Motion and the Shortcomings of the Rigid-Bunch Assumption. So far, stability of the coherent beam motion has been discussed using the model of a rigid bunch with a leading end and a trailing end. For the case of the resistive-wall wakes the effect on the beam centroid was of concern, rather than the behavior of individual particles, so this model was adequate. In analyzing the incoherent motion of particles within the beam, space-charge forces must be treated relative to the centroid rather than as an external effect. In the calculation of the space-charge tune shift on a single particle, the assumption of a uniform bunch was initially used to obtain an order-of-magnitude estimate when compared to the wake forces. This yielded a space-charge force which grows linearly with the radial position of the particle, but was, in fact, an overestimate. In practice, the transverse distribution is Gaussian, leading to a force given by [48]

$$F = \frac{2e^2\lambda}{\gamma^2 r}\left(1 - e^{-r^2/2\sigma^2}\right) \tag{6.1}$$

where r is the radial coordinate, λ is the number of particles in the bunch (or beam) per unit length, and σ is the RMS beam width. Compared to the uniform-beam case, the maximal tune shift occurs closer to the center of the beam than at the edge. Furthermore, an increase in intensity results in an increase in beam width, so an increase in particle density is not linear with an increase in intensity. The extent to which the beam grows with intensity is difficult to predict but can be measured.

6.3 A Measurement of the Space-Charge Tune Shift via Resonant Extinction of the Beam

In the study that follows the intensity-dependent tune shift in the Booster including space-charge forces and their incoherent effect was obtained through an indirect measurement involving beam extinction near half-integer resonance for varying intensities. The procedure was performed by D. McGinnis, P. Spentzouris, J. Amundson, and W. Pellico in 2003, with the Booster operating with a coasting (unaccelerated), unbunched beam. We summarize the procedure first, after which the details of the measurement and the results are presented.

6.3.1 Summary of the Procedure. The normal operating tunes of an accelerator are usually chosen so as not to be too close to a prominent resonance, in particular, the ones involving integer and half-integer tunes. Starting from this stable operating point, quadrupole currents can be changed to bring the tunes (or the tune in one plane) slowly closer to one of these resonances. We choose the half-integer case for illustration. Inherently, the distribution, though centered about some value, has a spread in the tunes of the individual particles, so as the center is moved toward a half-integer frequency, particle loss begins. Particles with tunes nearer to the resonant frequency will usually be lost first, and as the central tune continues to approach this half-integer value, more particles fall within the resonant stopband, thus growing in betatron amplitude. In this way eventually the entire beam can be lost.

This effect was measured by scanning the tune space near the half-integer resonance. The quadrupole currents were varied for a base intensity of 5×10^{11} particles (one injected turn), and a change in tune for a given change in quadrupole strength was obtained. Beam extinction (fraction of beam lost) was then measured as a function of this calibrated tune change, for which a maximal value of this extinction at or near the half-integer resonance appeared. At higher intensities, an increase in the tune spread due to the defocusing effects of space charge was expected. A shift in the centroid tune was also observed, likely due to the known wake forces, among other things. Repeating the measurement using these higher intensities, a different tune change was then necessary to reach the extinction maximum. Furthermore, the shape of the extinction curve gave a measure of the relative tune spread of the particles in the beam, allowing the incoherent space charge effect to be studied.

6.3.2 Calibration of the Quadrupole Currents and Corresponding Tune Changes.

The measurement hinged on the correct calibration of the effect of the change in quadrupole current on the betatron tune. The calibration was performed as follows.

The Booster was run with otherwise nominal tunes at an intensity of one turn injected (0.5×10^{12}). Tune change as a function of quadrupole current (the corrector circuits QS and QL) was determined for both horizontal and vertical planes. Tune change was measured initially from a pickup attached to the damper plates interfaced to a vector signal analyzer (VSA 89441A). Once calibration was complete, a mapping from the changes in current in the quadrupole circuits to the changes in betatron tunes was obtained. The Booster was held at the 400-MeV injection kinetic energy by disabling the effects of the RF cavities and holding the main dipole and quadrupole magnet ramps to a constant current to maintain stable orbits at 400 MeV. Although the beam was not being accelerated, a slight amount of RF voltage was still present, so a minimal amount of bunch structure was detectable, but for the most part the beam was run in a coasting, DC configuration.

6.3.3 Measurement of the Beam-Extinction Maximum in Tune Space. When the quadrupole calibrations (quadrupole current change to tune change) and nominal tunes were obtained, this information was supplied to console program PA 1380,[47] which was used to calculate the precise combination of quadrupole currents to independently vary the fractional part of the horizontal and vertical tunes Q_x, Q_y,[48] in increments of 0.025 from a minimum of 0.50 to a maximum of 0.975. This yielded 20 values each for Q_x and Q_y, in every combination, for a total of 400. A typical file header, followed by a the first two lines of data, demonstrating the appropriate changes in quadrupole current to produce certain tunes, is shown in Figure 6.1

```
Reset $17
Snap flag
Min E12 0.100000
Max dQx 0.250900  Min dQx -0.249100  Num dQx 20
Max dQy 0.187600  Min dQy -0.312400  Num dQy 20
Qx0 0.749100
Qy0 0.812400
dIQL -0.100000  dIQS -0.100000
dQx/dIQL -0.010000 dQy/dIQL 0.024900
dQx/dIQS -0.043200 dQy/dIQS 0.006600

# Description 1turn 01/30/03 00590059
# dQx       dQy        dIQS       dIQL       pdcs       chg1       chg2
-0.249100 -0.312400 -0.923717 1.499459 0.595942 0.504893 0.190696
-0.249100 -0.287400 -0.898957 1.392495 0.591056 0.253224 -0.047907
```

Figure 6.1. Headers and First Two Lines of Readout from Console Application PA1380 Determining Quadrupole Current for Precise Booster Tune Control Calibrated at One Injected Turn of Intensity.

---

[47] Application was written by D. McGinnis.

[48] We use Q as the fractional part of the tune to maintain consistency with the software notation.

The meaning of the readout is as follows. Q_{x0} and Q_{y0} were the initial tunes as the beam was injected from the 400-MeV transport line. The maximal change in Q_x, Max dQ_x, from this nominal value was 0.250900 and the minimal (i.e. "most negative") change Min dQ_x was -0.249100. The description is analogous for Q_y. This total tune interval was 0.5 (the sum of these two quantities) and was covered in 20 steps in both planes (Num dQ_x, Num dQ_y, 0.02500 per step), so that both fractional tunes would sweep through a range from 0.500 to 0.975 inclusive. The next lines show the results of the calibration of the quadrupole circuits. With dIQL and dIQS changed by 0.1 A, the tune changes dQx and dQy with respect to quadrupole-circuit current changes dQS and dQL are given. These are $dQ_x/dIQS = -0.043200$, $dQ_x/dIQL = -0.010000$, $dQ_y/dIQL = 0.024900$ and $dQ_y/dIQS = 0.006600$ (all in A^{-1}). Given these calibration parameters the ability to scan through the values of Q_x and Q_y in regular intervals was provided by PA 1380. (An algorithm similar to the one implemented has been documented, albeit much earlier, by C. Ankenbrandt [11].)

The first two lines of data (400 in total for each intensity) represent the measurements relevant to the study. pdcs represents the measured Linac intensity, whose values were considered representative of the Booster injection intensity. chg1 was the Booster intensity at 2000 turns, and chg2 the Booster charge at 6000 turns. chg1, chg2, and pdcs are all given in units of 10^{12} particles, while dQ_x and dQ_y are the changes in the horizontal and vertical tunes relative to the nominal values Q_{x0} and Q_{y0}, obtained by changing the quadrupole circuits by the amounts given in the columns dIQS and dIQL (measured in Amperes).

Intensity was recorded both at injection from the Linac and after 2000 turns, from which the percentage of beam lost was calculated. 2000 turns was chosen because the extinction (i.e. loss) of the beam at the half-integer resonance by 2000 turns into the cycle was prominent enough to be measured, with tunes near this value demonstrating a reduced loss of the beam, allowing for a clean numerical fit of the tune width over which beam loss was occurring. Measuring earlier in the cycle would have lowered the signal amplitude, since fewer particles would have been lost, resulting in less precision, while measuring later in the cycle (such as at 6000 turns) would have tended to replace the fit with a broad, flat range of tunes near the resonance all at 100% extinction. 2000 turns was thus considered a good compromise.

To obtain the behavior of the extinction maximum for increasing intensity, the measurements were repeated for 2, 3, and 9 turns injected. The tune shift due to space charge could be inferred by observing how much tune change was needed to bring the beam within the half-integer stop-band, as a function of injected beam intensity (all other machine conditions remaining the same). Since space charge is naturally defocusing, given the same initial quadrupole settings, the tune change needed to reach the extinction point (half-integer stop band) with more beam intensity differed from the one-turn-injected case. Thus, the final tune value at the extinction maximum as calculated from the console program (in which the starting tune values were assumed to be the same as they were in the one turn calibration) would have appeared to be different than for the one-turn case. The actual difference however, did not lie in the final tune, which of course, was the same half-integer resonance eventually extinguishing the beam, but in the tune change required to reach complete beam extinction from the starting quadrupole settings. Since the amount of tune change is the quantity varying with intensity, for clarity the subsequent figures use difference in the tune change required to reach the measured extinction maximum (ostensibly the half-integer resonance) relative to the tune change required for one turn injected, rather than the tune as calculated by the program.

6.3.4 Selected Results from the Extinction Study. Before proceeding with these results, we provide an example of the measurement and its indirect evaluation of the tune change. For one turn injected, for a given pair of initial tunes of, say, $Q_x = 0.550$, $Q_y = 0.700$, the necessary changes to the quadrupole currents to reach these tune values from the initial nominal tunes, found by the calibration, were dIQS = −0.602328 A and dIQL = 0. 611059 A. For higher intensity, because of the space-charge defocusing and the resistive-wall wakes, the actual starting tunes of the particles were lower than this. However, the initial tune at these higher beam intensities was not directly measured. Instead, the quadrupole-current change needed to reach the extinction maximum was determined, and given the calibration this was mapped to the necessary tune change to reach extinction. The application software was operated under the assumption that the initial tunes at these varying intensities were identical (since the initial quadrupole current settings were the same) and that the tune at which the beam was extinguished changed. In fact, the tune at which the beam is extinguished (the half-integer resonance in this case) does not change, and it was the initial tune that varies due to intensity dependent defocusing effects. At higher beam intensities the initial tunes were certainly lower than they were in the one-turn case for the same corrector strength, and the extinction maxima in the higher-intensity cases were achieved with lower quadrupole current, and appeared to come at tunes larger than 0.5. The difference between the extinction maxima at higher intensity and the extinction maximum at one turn corresponds to the shift in tune due to intensity effects such as the resistive-wall wakes and space charge.

The data set with the most clarity was in the vertical plane where the particles were driven toward the half-integer resonance. The half-integer points were approached in both the horizontal and vertical planes, but the results were not as clear in the horizontal. Figure 6.2 demonstrates the behavior near the half integer point for the vertical tune under varying intensities.

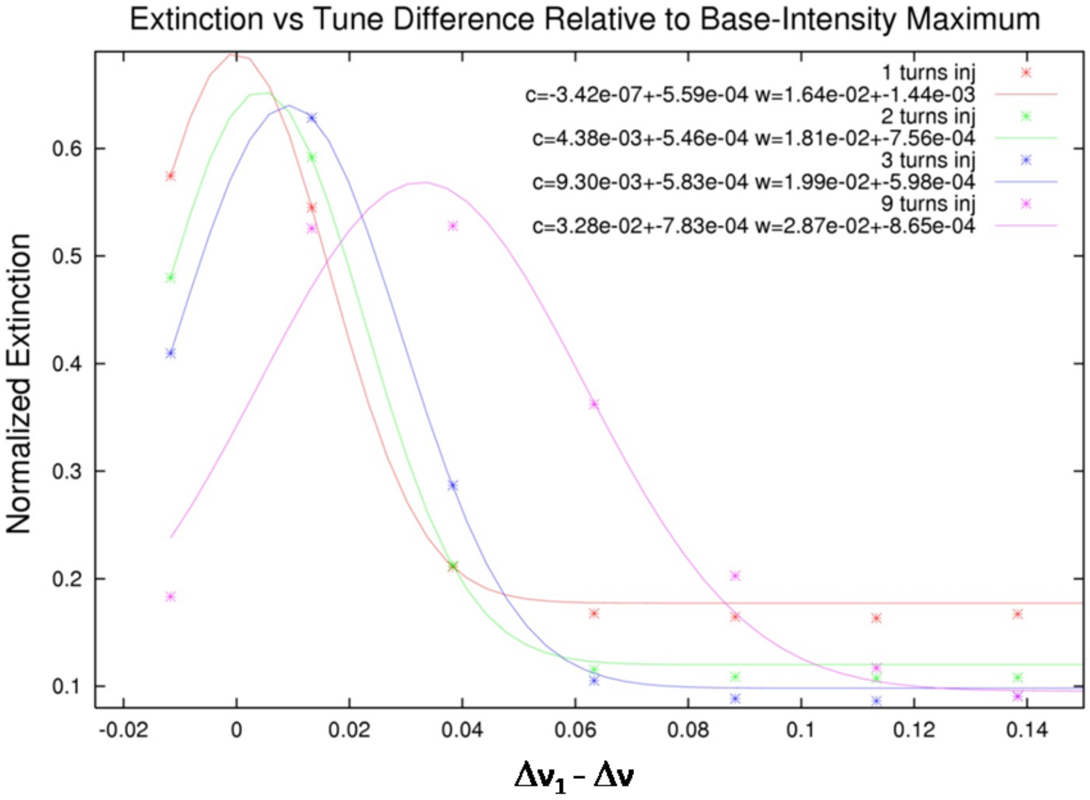

Figure 6.2. Extinction Curves for Vertical Tune Change Approaching the Half-Integer Resonance, with Respect to Change Required to Reach Maximal Extinction in the One-Turn-Injected Case. Horizontal Tunes are Far from Resonance. Color Scheme for Various Intensities is Provided in the Legend.

We are interested in how the location in tune of the extinction maximum varies with intensity. $\Delta\nu_1$ refers to the required change in tune in the one-turn-injected case from the initial tune to reach the extinction maximum. Δν is a corresponding tune change for some quadrupole setting, assuming all intensities had the same starting tunes. The required tune change to reach maximal extinction in the lowest-intensity case was naturally the largest, so $\Delta\nu_1$-Δν begins at zero at the extinction maximum for this intensity, and the curves for all higher intensities are located to the right of this. It must be stressed that this measurement does not characterize the shift in the tune of the beam for every value in tune space relative to the one-turn-injected case. It only shows a relative shift in the apparent location of the extinction maximum as intensity increases. We let $\Delta\nu_n$ be the tune change required to reach maximal extinction for n turns injected (n being 1, 2, 3, or 9). The shift of this point as a function of starting beam intensity is shown in Figure 6.3.

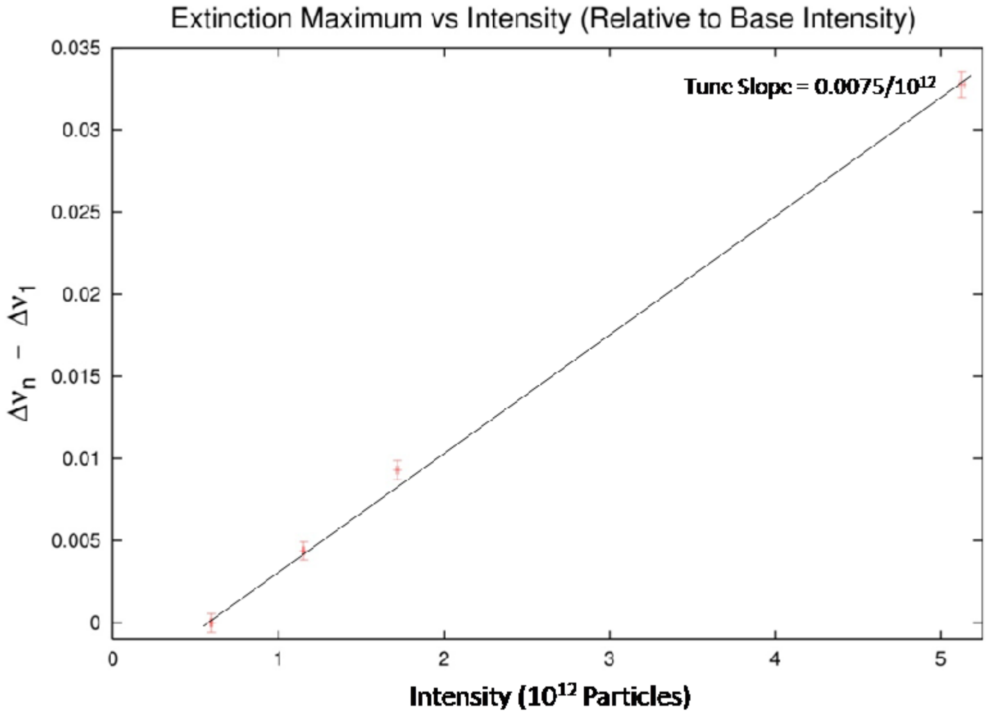

Figure 6.3. Shift in Extinction Maximum under Increasing Intensity from 0.5×10^{12} to 5.1×10^{12} Particles. Points (red) and Linear Fit with Slope (black) are Provided.

The slope of the shift of the maxima in Figure 6.3 is around $7.5 \times 10^{-3}/10^{12}$. This represents a change in the coherent motion of the beam, since it demonstrates how the central tune of the particle distribution has shifted. The obtained tune slope is in keeping with the value obtained from the studies presented in Chapter 5, where the combination of the defocusing dipole and quadrupole wakefields were capable of explaining the effect. In this case, the value is somewhat lower (20%). Since the beam was unbunched, the longitudinal density was lower. The wakes, then, especially for the dipole contribution, likely had less of an impact than in the bunched case. Also a relatively gradual particle loss near the extinction point may have played a role. Particle loss near the resonance did not happen instantaneously, and as the beam intensity near the half-integer tunes was diminished, the resulting tune shift was then mitigated somewhat, and the effective tune slope was softened to some degree, resulting in a slightly lower observed value than in the studies presented in Chapter 5.

Since the shift in the peak leading to earlier approach to the resonance is a purely coherent effect, it can be explained by the wakefield phenomena already discussed, since its magnitude is also similar to the predicted values from Chapters 4 and 5. The change in the width of the curve, a purely incoherent phenomenon, corresponds directly to the effect of the space-charge forces within the beam. In Figure 6.4 the Gaussian width of the extinction curves is plotted as a function of intensity.

A linear trend is observed, with an extinction-width dependence on intensity given by $3 \times 10^{-3}/10^{12}$. We equate the stopband width for the given intensity with the fitted width (σ_{ext}) of the extinction curve. The shape of the extinction curves in Figure 6.2 arises from the existence of the particle tune spread. The broadening of the curves with intensity gives a measure of the change in the tune spread since the level of beam extinction depends on the fraction of particles sitting, on average, at or near the half-integer tune. Under higher intensity the spreading increases as more particles are, on average, perturbed by stronger local space-charge fields. And, of course, a greater number of particles are available to be perturbed by these self-fields, leading to more samples further from the central tune relative to lower-intensity case. These two factors lead to the widening of the stopband and thus to an increase in the tune spread with intensity.

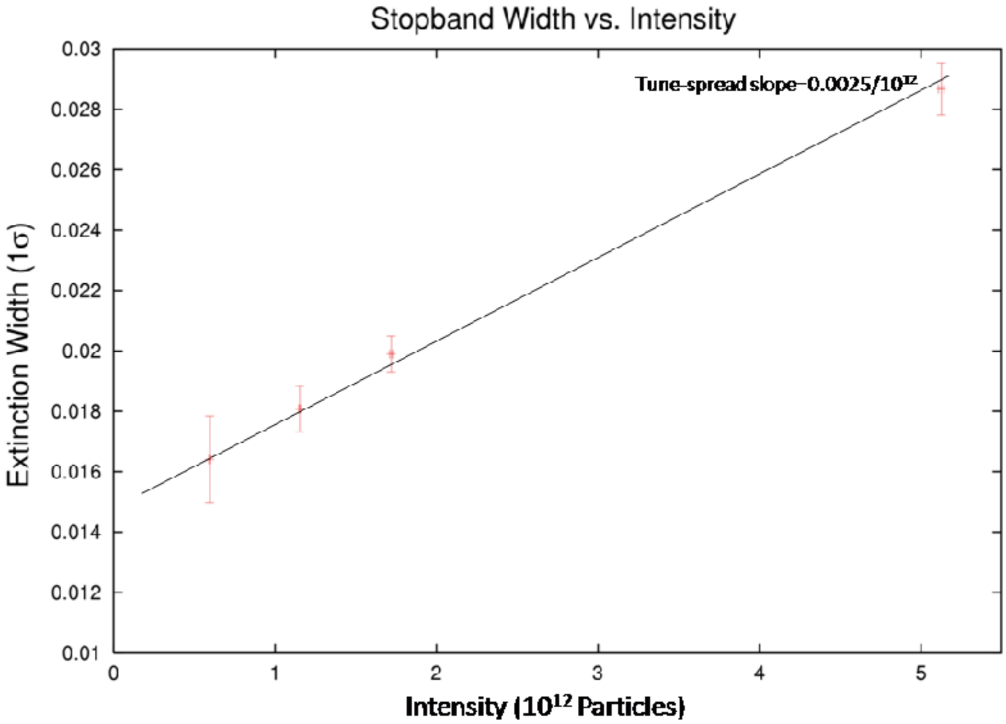

Figure 6.4 Dependence of Extinction Width under Increasing Intensity from 0.5×10^{12} to 5.1×10^{12} Particles. Points (red) and Linear Fit with Tune-Width Slope (black) are Provided.

6.4 Comparison with more Realistic Calculations of the Space-Charge Tune Shift

We now seek to compare a more realistic prediction of the space-charge tune shift with the data presented in Section 6.3.4. The space-charge tune shift for a Gaussian particle distribution (in configuration space) can be obtained from the space-charge force within a Gaussian beam given by (6.1). Unlike the uniform beam, whose space-charge forces increase linearly with radial coordinate, a Gaussian beam does not have a defined edge, so while initially the space-charge force increases away from the beam centroid, eventually the inverse-square behavior of the electromagnetic force dominates over the increasing charge seen by the particle away from the center. We wish to use comparable numbers as in the uniform case, wherein the maximal tune shift was calculated for a representative Booster beam of 5mm in size. Since RMS beam widths, σ_{RMS}, are readily measured, let ς represent the ratio of the particle coordinate to the RMS width, or

$$r = \varsigma \sigma_{RMS} \tag{6.2}$$

In this case (6.1) can be written as

$$F = \frac{2e^2}{\gamma^2 \varsigma} \frac{1 - e^{-\varsigma^2/2}}{2\pi R_{path}} \frac{\Xi}{\sigma_{RMS}} \tag{6.3}$$

Since the beam was unbunched, the particle density λ can be expressed in terms of the total particle count Ξ divided by the orbit circumference $2\pi R_{path}$. Figure 6.5 shows the behavior of the tune shift parameterized by ς for a given σ_{RMS}, as calculated from (2.13). For the Gaussian beam, we see a maximum, for any value of σ_{RMS}, at ς near 1.5. For a given intensity, then, the maximal tune shift for a Gaussian beam is inversely proportional to the RMS width. Evaluation of the maximal space-charge tune shift then hinges on obtaining suitable RMS beam-width values.

RMS widths for the coasting beam were not obtained during this study, but representative IPM data were obtained in subsequently by X. Huang in the same month [7] under similar operating conditions. These have been retrieved and values near the intensities in the study are given in Table 6.1. Calculated particle densities are included as well. Since the extinction measurement corresponds to the vertical plane, vertical IPM data are used.

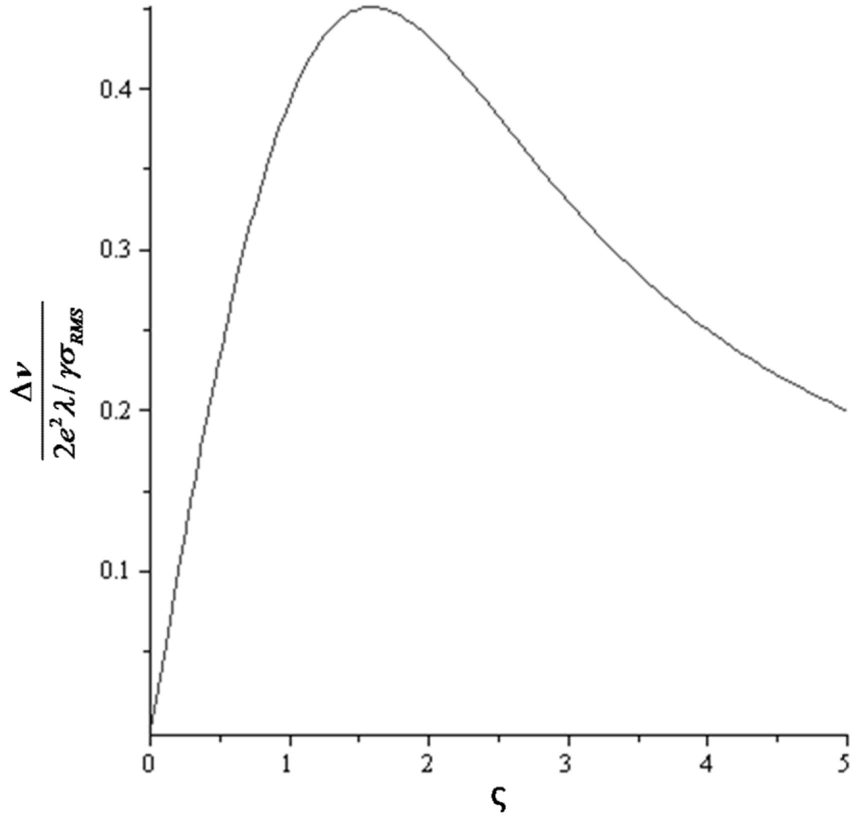

Figure 6.5. Tune Shift for a Particle at Radial Position r = $\varsigma\sigma_{RMS}$ Within a Gaussian Beam with Transverse Width σ_{RMS} as a Function of ς.

Table 6.1. Particle Densities, Intensities, and RMS Widths for Values Similar to Those in the Extinction Measurement (Ref [11])

Intensity (10^{12} particles)	0.50	1.3	1.8	5.2
Particle Density (10^{10}/m)	0.11	0.28	0.38	1.1
IPM Width (mm)	6.0	6.3	6.8	9.2

Inserting (6.3) into (4.8), the tune shift is then given by

$$\Delta\nu = \frac{R_{path} r_p}{\varsigma^2 \gamma^3 \beta^2} \frac{1-e^{-\varsigma^2/2}}{2\pi\nu_0} \frac{\Xi}{\sigma_{RMS}^2} \tag{6.4}$$

We choose ς to be 1.5 as before, and the remaining factors have their usual meaning as given throughout this work. They are given in Table 6.2 for convenient reference.

Table 6.2. Reference Parameters for the Evaluation of (6.4)

R_{path} (m)	r_p (m)	γ	β	ν_0
74	1.535×10^{-18}	1.4	0.71	6.8

In Figure 6.6 the values from Tables 6.1 and 6.2 in (6.4) are plotted, along with the corresponding linear fit. The tune shift $\Delta\nu_{max}$ is the maximal shift obtained at ς near 1.5, and is thus representative of the total tune spread of this Gaussian beam.

One may consider the location on the tail of the fit to the extinction data where particle loss begins to be measured, but this is subject to many operating conditions, as well as the limitation of our fitting routine. Though the tails of a Gaussian are of infinite extent, particles are not, after all, infinitely shifted in tune, so we must apply a cutoff somewhere within which almost all particles would be. A reasonable (though still somewhat arbitrary) value for this would be at $2\sigma_{ext}$, which incorporates, from the fitting model, 95% of the particles defocused by the space-charge tune shift. We then obtain a tune slope of $5\times10^{-3}/10^{12}$ (that is, twice the slope of the extinction-width change under intensity) as a realistic measure of the maximal shift due to space charge in our Gaussian-distributed beam from the extinction measurement.

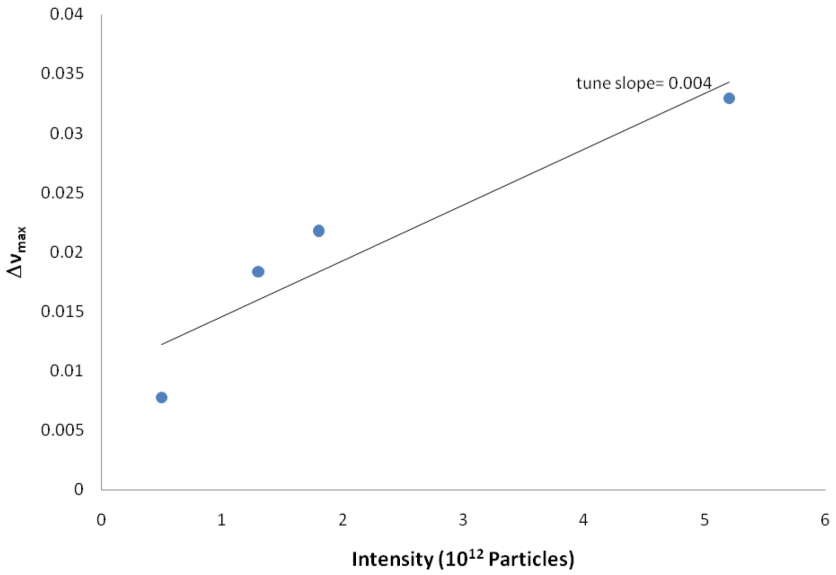

Figure 6.6. Maximal tune shift evaluated from (6.4) for Gaussian Beam with measured parameters given in Tables 6.1 and 6.2.

The tune slope in the extinction data is larger than the IPM-based prediction by 25%. Given the precision of the RMS widths from fitting IPM data, we find this level of agreement encouraging. In any case, these can now be compared to the more simple-minded calculation in Section 4.5.

For the uniform-beam case in Section 4.5 the tune shift at the periphery was found to be 0.6 at the given beam intensity of 4.5×10^{12} (0.3 in the unbunched case for the Booster). The corresponding tune slope would be (assuming zero shift at zero intensity) $0.07/10^{12}$ to $0.14/10^{12}$, depending on whether or not longitudinal bunching is considered. Compared to the values above, this is an overestimate by a factor of around 15 (unbunched prediction) to 30 (bunched prediction). While the space-charge effects were predicted from the Laslett formula to be larger by a factor of 50 near injection than the image-charge effects, because of the effects of a nonuniform (i.e. Gaussian) beam allowed to grow realistically with intensity, and because of the factors augmenting the wakefield effects given in Chapters 4 and 5, in practice they are rivaled by, and in some cases even surpassed by, the wakefield phenomena.

CHAPTER 7

CONCLUSION

7.1 Summary

The effectiveness of a hadron-particle accelerator as a tool for high-energy physics research is due in large part not only to the energy to which particles can be accelerated, but also to the achievable beam intensity. Higher particle density provides a greater number of interactions per unit time, allowing for better statistics on the observed interactions of the eventual collisions of the high-energy particles. An understanding of the phenomena leading to intensity limitations allows for possible schemes to mitigate these effects as well as provides foresight into the design of future accelerators.

The Fermilab Booster, a nearly 40-year-old proton synchrotron operating as an intermediate accelerator between the Fermilab Linac and the Main Injector, is the lowest-energy circular accelerator in the chain. Currently its operating intensity is twice that of the value intended in its design. With its relatively low injection energy, effects due to space charge are an important consideration. Also 60% of the orbit trajectory is housed inside large, 10-m-long, roughly rectangular, combined-function magnets constructed from stacked, electrically separated steel laminations. The electromagnetic response from these elements due to the passing beam has been shown to prominently affect the transverse oscillation frequencies of the beam near injection.

Measurements on the coherent shifts of the particle tunes have shown a behavior where the values in the vertical plane were lowered with increasing intensity, while those in the horizontal plane were slightly elevated. The shifting of the tunes in this opposite sense happened in a cumulative manner over several hundred turns. Unlike the familiar

Laslett tune shifts for a rectangular geometry the effect was not symmetric, and could be explained by a resistive-wall wakefield in which a combination of two components was observed. The first was a completely defocusing dipole component due to the centroid oscillation of the beam, whose average effect on the tune over many turns was predicted to be small, but because of the presence of magnetic laminations was magnified almost one hundred-fold. The second was a quadrupole-like term arising from the roughly rectangular magnet geometry, which led to a focusing in the horizontal plane and a defocusing in the vertical plane. Unlike the dipole term, the passing of successive bunch trains led to a surprisingly large cumulative effect. The predicted tune dependence on intensity due to the dipole term was found to be roughly $-0.003/10^{12}$ particles, and for the quadrupole wake a prediction of $\pm 0.004/10^{12}$ particles, with the positive value for the horizontal plane, and the negative for the vertical plane. Results from two separate studies were found to be in keeping with these results.

The effect of space charge on the individual particle tunes was investigated through a measurement involving resonant extinction of the beam. The predicted result for the representative incoherent particle tune shift under increasing intensity using a realistic Gaussian distribution, and allowing growth of the beam envelope with intensity, was found to be $0.004/10^{12}$, using actual transverse RMS widths to make the estimate. The tune-spread dependence on intensity obtained by quantification of the resonant stop-band width from the beam-extinction measurements was found to be $0.005/10^{12}$, similar to the predicted value. Both values were considerably smaller by one order of magnitude compared to the uniform-beam value obtained from the Laslett formula. Under these circumstances, the incoherent contribution from space charge to the transverse frequency shift near the injection energy was actually rivaled and in some cases surpassed by the coherent wakefield effects, shifting the particle tunes and that of the centroid by the same order of magnitude.

Emittance is typically a quantity characterizing the size of charged-particle beams and a staple in their dynamical analysis. Its statistical definition through RMS position and momentum widths can be used as a figure of merit to assess beam quality. The existence of space-charge fields tends to couple otherwise independent planes of motion, resulting in emittance exchange among them. Distinguishing between emittance exchange among the planes of motion, and possible emittance growth necessitates a simultaneous measurement in all planes of motion. A method for obtaining a simultaneous measurement of the emittance has been successfully applied using the available instrumentation in the Booster, the Ionization Profile Monitor (IPM) in the transverse planes and the Resistive Wall Monitor (RWM) in the longitudinal. Results experimentally match accepted values for the emittances in all three planes. Correction for unmeasurable correlation terms between the planes was obtained through simulation values and found to be at most an 8% effect on the emittance value. This method may prove useful when large amounts of emittance exchange are expected.

APPENDIX A

EXACT AND APPROXIMATE EXPRESSIONS FOR THE ELECTROMAGNETIC FIELDS ON A TRAILING PARTICLE DUE TO THE FIELDS FROM LEADING PARTICLES IN A RESISTIVE CYLINDRICAL CHAMBER

The electric and magnetic fields on trailing particles produced by the leading particles in a passing beam has been derived by Karl Bane [13, 31], and are given by

$$E_s = \frac{-16q}{R^2}\left[\frac{1}{3}e^u \cos\left(\sqrt{3}u\right) - \frac{\sqrt{2}}{\pi}\int_0^\infty \frac{x^2 e^{ux^2}}{x^6+8}dx\right] \tag{A.1}$$

$$E_r = B_\theta = \frac{8qr}{(2\chi)^{1/3}R^3}\left[\begin{array}{c}\frac{1}{3}e^u \cos\left(\sqrt{3}u\right) - \frac{1}{\sqrt{3}}e^u \sin\left(\sqrt{3}u\right) \\ -\frac{\sqrt{2}}{\pi}\int_0^\infty \frac{x^4 e^{ux^2}}{x^6+8}dx\end{array}\right] \tag{A.2}$$

E_s is the longitudinal electric field retarding the motion of subsequent particles and E_r, B_θ are the radial and azimuthal fields affecting their transverse motion; R is the pipe radius, χ and u are dimensionless parameters given by

$$\chi \equiv c/4\pi\sigma R \tag{A.3}$$

$$u = z/(2\chi)^{1/3}R \tag{A.4}$$

The field patterns in the region near the leading particle are plotted in Figure A.1.

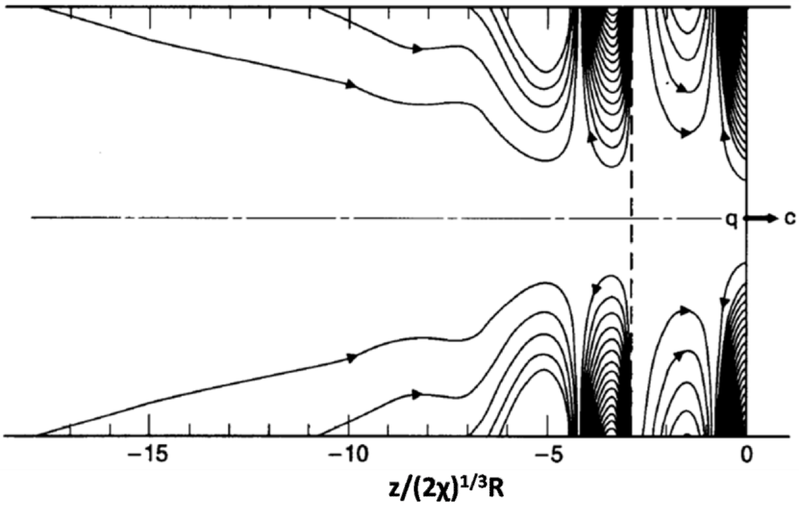

Figure A.1. Electric Wakefield Lines in a Resistive Cylindrical Chamber of Radius R Generated by a Point Charge q Moving at Speed c. Field-Line Density to the Left of the Dashed Line has been Magnified by a Factor of 40. (Courtesy K. Bane and A. Chao).

In regions for which $|z| \ll \chi^{1/3}R$ [31], the fields may be expressed as

$$E_s \approx -\frac{4q}{R^2}+\frac{64}{3}\frac{q}{R^3}\sqrt{\frac{\sigma}{c}}z^{3/2} \tag{A.5}$$

$$E_r = B_\theta \approx \frac{2q}{b}\left[\frac{b}{r}-\frac{r}{b}\right]\delta(z)+16\frac{q}{b^3}r\sqrt{\frac{\sigma}{c}}z^{1/2} \tag{A.6}$$

The dynamics is more complicated close to the leading particle. As Figure A.2 shows, the fields change sign three times in the region $|z| < 5\chi^{1/3}R$.

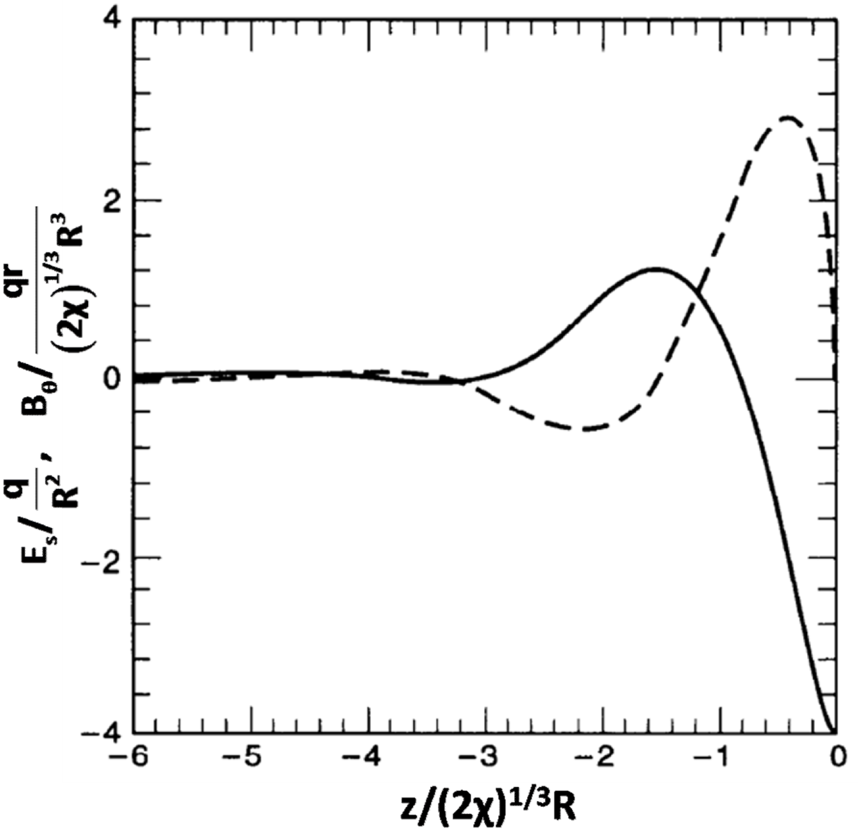

Figure A.2. Short-Range Resistive-Wall Wakefield Components E_s and B_θ in a Cylindrical Chamber of Radius R. Fields Vanish at z = 0 and Change Sign Thrice in this Region. (Figure Courtesy A. Chao).

APPENDIX B

A SUMMARY OF THE DERIVATION OF THE GENERALIZED WAKE FUNCTIONS FOR CHAMBERS OF NONCIRCULAR CROSS SECTION

For purely circular cross sections, dipole, quadrupole, etc, wakefields are the result of oscillations within the distribution. For lower symmetry, the structure can produce strong higher-order wakefields even for a beam for any type of oscillation (dipole, quadrupole, etc). Given the theory by Wagner, Heifets, and Zotter [59], we seek to obtain an expression for the wake functions describing the effect on a beam for rectangular types of symmetry. The causality condition in frequency space may be expressed as

$$Z(\omega, r, \varphi, r_0, \varphi_0) = Z^*(-\omega, r, \varphi, r_0, \varphi_0) \tag{B.1}$$

The longitudinal impedance, $Z_{||}$ can be obtained by integration over the longitudinal electric field [92]. Namely,

$$Z_{||}(\omega, r, \varphi, r_0, \varphi_0) = \int dz e^{-ikz} E_z(\omega, r, \varphi, r_0, \varphi_0) \tag{B.2}$$

In the frequency domain, we may write E$_z$ as the double-Fourier transform

$$E_z(\vec{r}, \vec{r}_0, t) = \int_{-\infty}^{\infty} \frac{d\omega dq}{(2\pi)^2} \left[A(\omega, q, \vec{r}, \vec{r}_0) + A^*(-\omega, -q, \vec{r}, \vec{r}_0) \right] e^{i(qz-\omega t)} \tag{B.3}$$

E$_z$ may be decomposed into a component whose wave speed is synchronous with the (monoenergetic) beam, and another consisting of all others asynchronous with it. It has been shown that the effects of all field components traveling asynchronously average to zero [128]. For the remaining synchronous component, E_z^{syn}, we may identify q = k = ω/c. This requires that E_z^{syn} independently obey the wave equation

$$\left[\nabla^2 + k^2 \right] E_z^{syn} = 0 \tag{B.4}$$

And hence the corresponding impedance must therefore satisfy the (transverse) Laplace equation,

$$\nabla_{\perp}^{2} Z_{\parallel}\left(\omega,\vec{r},\vec{r}_0\right)=0 \tag{B.5}$$

Solutions to the Laplace equation may be written as a power series, or in this case, a double power series in both $\vec{r}$ and $\vec{r}_0$. It may also be convenient to write this sum in terms of the complex variables $r_{\pm}=x\pm iy$ in place of the radial coordinates.

$$\begin{aligned} Z_{\parallel}\left(\omega,\vec{r},\vec{r}_0\right)=\sum_{m=1}^{\infty}\sum_{k=0}^{\infty}\Big\{&\left[\alpha_{mk}\left(\omega\right)r_{0+}^{k}+\beta_{mk}\left(\omega\right)r_{0-}^{k}\right]r_{+}^{m}+\ldots \\ &\ldots+\left[\alpha_{mk}^{*}\left(-\omega\right)r_{0-}^{k}+\beta_{mk}^{*}\left(-\omega\right)r_{0+}^{k}\right]r_{-}^{m}\Big\} \end{aligned} \tag{B.6}$$

In our case this will facilitate our transition into rectangular geometries. Since the wake function is the inverse Fourier transform of the impedance, it may also be so expressed, except that the coefficients α_{mk},β_{mk}, etc. are now functions of the longitudinal coordinate s instead of frequency content ω. Specifically,

$$\alpha_{mk}\left(s\right)=\int_{-\infty}^{\infty}\frac{dw}{2\pi}\alpha_{mk}\left(\omega\right)e^{-i\omega s/c} \tag{B.7}$$

and so on. The corresponding wake function is then

$$\begin{aligned} W_{\parallel}\left(\vec{r},\vec{r}_0,s\right)=\sum_{m=1}^{\infty}\sum_{k=0}^{\infty}\Big\{&\left[\alpha_{mk}\left(s\right)r_{0+}^{k}+\beta_{mk}\left(s\right)r_{0-}^{k}\right]r_{+}^{m}+\ldots \\ &\ldots+\left[\alpha_{mk}^{*}\left(s\right)r_{0-}^{k}+\beta_{mk}^{*}\left(s\right)r_{0+}^{k}\right]r_{-}^{m}\Big\} \end{aligned} \tag{B.8}$$

Up to now our discussion in this section has been focused on developing the impedance or wake affecting the longitudinal motion. The Panofsky-Wentzel theorem (4.26) provides the necessary connection.

In this case it can be re-expressed in terms of these generalized wakes as

$$\nabla_{\perp}W_{\parallel}\left(\vec{r},\vec{r}_0,s\right)=\frac{\partial}{\partial s}W_{\perp}\left(\vec{r},\vec{r}_0,s\right) \tag{B.9}$$

Making use of (B.9), the transverse wakes in the x and y direction are given by

$$W_x(s)=\sum_{m=1}^{\infty}\sum_{k=0}^{\infty}m\left\{\left[a_{mk}(s)r_{0+}^{k}+b_{mk}(s)r_{0-}^{k}\right]r_{+}^{m-1}+\dots\right.$$
$$\left.\dots+\left[a_{mk}^{*}(s)r_{0-}^{k}+b_{mk}^{*}(s)r_{0+}^{k}\right]r_{-}^{m-1}\right\} \tag{B.10}$$

$$W_y(s)=\sum_{m=1}^{\infty}\sum_{k=0}^{\infty}im\left\{\left[a_{mk}(s)r_{0+}^{k}+b_{mk}(s)r_{0-}^{k}\right]r_{+}^{m-1}-\dots\right.$$
$$\left.\dots-\left[a_{mk}^{*}(s)r_{0-}^{k}+b_{mk}^{*}(s)r_{0+}^{k}\right]r_{-}^{m-1}\right\} \tag{B.11}$$

where

$$\frac{\partial a_{mk}(s)}{\partial s}=-\alpha_{mk}(s),\quad \frac{\partial b_{mk}(s)}{\partial s}=-\beta_{mk}(s) \tag{B.12}$$

For a beam executing dipole oscillations in a rectangular (or elliptical) chamber, (B.10-11) reduce to

$$W_x(s)=ax_0+bx \tag{B.13}$$
$$W_y(s)=-\bar{a}y_0-by \tag{B.14}$$

The coefficients a and ā are complex conjugates of each other, and represent the dipole component of the wakefield. In the case of symmetry with respect to 90° rotation (including circular or square symmetry), a = ā and the quadrupolar components vanish, reducing to the familiar dipole wakefield in a circular chamber.

BIBLIOGRAPHY

[1] Alexahin Y., & Gianfelice-Wendt, E. (2006). A new algorithm for the correction of the linear coupling at the Tevatron. *Proceedings of the European Particle Accelerator Conference 2006, Edinburgh, Scotland,* 2047-2049

[2] Alexahin Y., private communication

[3] Alexahin, Y., & Gianfelice-Wendt, E. (2006). Determination of linear optics functions from TBT data. *Fermilab Pub-06-093-AD,* n.p.

[4] Amundson J., & Spentzouris, P. (2003). Synergia: A Hybrid, Parallel Beam Dynamics Code with 3D Space Charge. *Proceedings of the 2003 Particle Accelerator Conference, Portland, Oregon,* 1-3

[5] Amundson J., Lackey, J., Spentzouris, P., Jungman, G., & Spentzouris, L. (2003). Calibration of the Fermilab Booster ionization profile monitor. *Physical Review, Special Topics - Accelerators and Beams 6*, *102801*, 1-8

[6] Amundson J., Pellico, W., Spentzouris, L., Spentzouris, P., & Sullivan, T. (2006). An experimentally robust technique for halo measurement using the IPM at the Fermilab Booster. *Fermilab Pub-06-060-CD,* 1-16

[7] Amundson J., Private Communication

[8] Amundson J., Spentzouris, P., & Dechow, D. (2005) Overview of the Synergia 3D multi-particle dynamics modeling framework. *Proceedings of the 2005 Particle Accelerator Conference, Knoxville, TN,* 3490-3492

[9] Amundson J., Spentzouris, P., Qiang, J., & Ryne, R. (2006) Synergia: An accelerator modeling tool with 3D space charge. *Journal of Computational Physics, 211,* 229-248

[10] Amundson, J., & Spentzouris, P. (2002). Synergia: A hybrid, parallel 3D space charge code with circular machine modeling capabilities. *Proceedings of the International Computational Accelerator Physics Conference, Michigan State University,* 2939-2941

[11] Ankenbrandt C.M. (1977). Relationship between QS, QL, and Booster tunes. *FNAL Operations Bulletin, 584,* n.p.

[12] Baartman, R. (1998). Betatron resonances with space charge. *Workshop on Space Charge Physics in High Intensity Hadrons Rings, Shelter Island NY, May 1998*, 56-72

[13] Bane, K. (1991). The short range resistive wall wake fields. *Slac Report AP-87*, 1-26

[14] Blewett, J.P. (1946). Radiation losses in the induction electron accelerator. *Physical Review 69,* 87-95

[15] Booster Staff, & E.L. Hubbard (Ed.). (1973). Booster Synchrotron. *FNAL Technical Memo TM-0405*, 57

[16] Booster Staff, & Hubbard, E.L. (Ed.)., (1973). Booster Synchrotron. *FNAL Technical Memo, TM-0405*, 1-120

[17] Buon J., (1992). Beam Phase Space and Emittance. *CERN Accelerator School : 5th General Accelerator Physics Course, Jyväskylä, Finland,* 89-116

[18] Burov A., & Danilov, V. (1999). Suppression of transverse bunch instabilities by asymmetries in the chamber geometry. *Physical Review Letters 82-11,* 2286-2289

[19] Burov A., Lebedev, V. (2002). Transverse resistive wall Impedance for multilayer flat chambers. *Procedings of the 2002 European Particle Accelerator Conference,* 1455-1457

[20] Burov, A., Lebedev, V. (2002). Transverse Resistive Wall Impedance for Multi-Layer Round Chambers. *Proceedings of the European Particle Accelerator Conference 2002,* 1455-1457

[21] Burov, A., Private Communication

[22] Chao, A. Heifets, S., & Zotter, B. (2002). Tune shifts of bunch trains due to resistive vacuum chambers without circular symmetry. *Physical Review Special Topics - Accelerators and Beams, 5,* 111001:1

[23] Chao, A., Heifets, S.,Zotter, B. (2002). Tune shifts of bunch trains due to resistive vacuum chambers without circular symmetry. *Physical Review Special Topics - Accelerators and Beams, 5,* 111001-5

[24] Chao, A., Heifets, S.,Zotter, B. (2002). Tune shifts of bunch trains due to resistive vacuum chambers without circular symmetry. *Physical Review Special Topics - Accelerators and Beams, 5,* 111005, (Private Communication w/ Cho Ng)

[25] Chao, A.W. (1993). *The physics of collective beam instabilities in high energy accelerators.* New York: John Wiley and Sons, Inc., 172-173

[26] Chao, A.W. (1993). *The physics of collective beam instabilities in high energy accelerators.* New York: John Wiley and Sons, Inc., 203-211

[27] Chao, A.W. (1993). *The physics of collective beam instabilities in high energy*

accelerators. New York: John Wiley and Sons, Inc., 38-126

[28] Chao, A.W. (1993). *The physics of collective beam instabilities in high energy accelerators.* New York: John Wiley and Sons, Inc., 40-56

[29] Chao, A.W. (1993). *The physics of collective beam instabilities in high energy accelerators*. New York: John Wiley and Sons, Inc., 41

[30] Chao, A.W. (1993). *The physics of collective beam instabilities in high energy accelerators*. New York: John Wiley and Sons, Inc., 43-48

[31] Chao, A.W. (1993). *The physics of collective beam instabilities in high energy accelerators.* New York: John Wiley and Sons, Inc., 47

[32] Chao, A.W. (1993). *The physics of collective beam instabilities in high energy accelerators.* New York: John Wiley and Sons, Inc., 55

[33] Chao, A.W. (1993). *The physics of collective beam instabilities in high energy accelerators*. New York: John Wiley and Sons, Inc., 59

[34] Chao, A.W. (1993). *The physics of collective beam instabilities in high energy accelerators*. New York: John Wiley and Sons, Inc., p. 88

[35] Christofilos, N. (1950). Focusing systems for ions and electrons. *U.S. Patent # 2,736,766*

[36] Cockcroft, J.D. & Walton, E.T.S. (1932). Experiments with high velocity positive ions. *Proceedings of the Royal Society of London A137,* 229-242

[37] Conte, M., & McKay, W.W. (2008). *An introduction to the physics of charged particle accelerators (2nd ed.).* Singapore: World Scientific Publishing Co. Pte. Ltd

[38] Courant E., & Sessler, A.M. (1965). Transverse Coherent Instability of Bunched Beams. *SLAC Storage Ring Summer Study SLAC-49,* 36-48

[39] Courant E., & Snyder, H. (1958). Theory of the alternating gradient synchrotron. *Ann. Phys. (Paris) 3, 1 (1958).*

[40] Courant E.D., Sessler, A.M. (1966). Transverse coherent resistive instabilities of azimuthally bunched beams in particle accelerators. *Rev. Sci. Instr. 37, 1579-1588*

[41] Courant, E.D., Livingston, M.S., & Snyder, H.S. (1952) The strong-focusing synchrotron - a new high energy accelerator. *Physical Review 88,* 1190-1196

[42] Crisp, J., & Fellenz, B. (2001). Measured longitudinal beam impedance of Booster gradient magnets. *Fermilab Technical Memo, TM-2145*

[43] Davidson, R.C. (2001). *The physics of nonneutral plasmas.* Singapore: World Scientific Publishing Co. Pte. Ltd.

[44] Dawson, J.M. (1983). Particle simulation of plasmas. *Reviews of Modern Physics 55*, 403

[45] E. Prebys, Radiation Issues for Fermilab Booster Magnets. *Proceedings of the 2005 Particle Accelerator Conference, Knoxville, TN*, 2041-2043

[46] E., Baller, B., & Spalding, W.J. (2004). The Proton Plan, *Fermilab-Beams-doc 1441,*n.p.

[47] Edwards, D.A., & Syphers, M.J. (1993). *An introduction to the physics of high energy accelerators.* New York: John Wiley and Sons, Inc.

[48] Edwards, D.A., & Syphers, M.J. (1993). *An introduction to the physics of high energy accelerators.* New York: John Wiley and Sons, Inc., 174

[49] Edwards, D.A., & Syphers, M.J. (1993). *An introduction to the physics of high energy accelerators.* New York: John Wiley and Sons, Inc., 32

[50] Elder, F.R., Gurewitsch, A.M., Langmuir, R.V. & Pollock, H.C. (1947). Radiation from electrons in a synchrotron. *Physical Review, 71* (11)*,* 829-830

[51] Endo, K., Egawa, K., Ohsawa, Y., Michikawa, & T. (1996). Estimation of radiation dose to epoxy resin by IR spectrophotometry. *Presentation at Euorpean Particle Aceleration Conference, 1996, Barcelona, Spain*, n.p.

[52] Ferlenghi E., Pellegrini, C., Touschek, B. (1966) *Nuovo Cimiento 44B,* 253

[53] Gluckstern R. (2000). Analytic methods for calculating coupling impedances. *CERN No. 2000-011*, 1-48

[54] Gluckstern, R. (1985). Coupling impedance and energy loss with magnet laminations. *Fermilab Technical Memo TM-1374*

[55] Gluckstern, R. (2000). Analytic methods for calculating coupling impedances. *CERN Report, CERN 2000-011*

[56] Griffiths, D.J. (1989). *Introduction to Electrodynamics (2nd ed.).* Englewood Cliffs, New Jersey: Prentice Hall, 385-386

[57] Haines M.G. (1996). Historical perspective: Fifty years of controlled fusion research. *Plasma Physics and Controlled Fusion, 38,* 643-656

[58] Harlow, F.H., (1955). A machine calculation method for hydrodynamic problems. Los Alamos Scientific Laboratory report LAMS-1956, n.p.

[59] Heifets, S., Wagner, A., & Zotter, B. (1998). Generalized impedances and wakes in asymmetric structures. *SLAC report, SLAC-AP110*

[60] Herrup D.A. (1995). Longitudinal emittance measurements in the Fermilab Booster. *Proceedings of the 1995 Particle Accelerator Conference and International Conference in High-Energy Accelerators,* 3007

[61] Hofmann, I. (2010). http://www-wnt.gsi.de/ihofmann/myhomepage/publistnew1 .pdf (current as of June, 2010)

[62] Humphreys, S. (1986). *Principles of Charged Particle Acceleration.*New York: John Wiley and Sons

[63] Iselin, C. (1983). Computing in accelerator design and operation. *Proceedings of the Europhysics Conference, Berlin, Germany, 1983, Lecture Notes in Physics, 215,* 146-151

[64] Ising, G. (1924). Prinzip einer Methode zur Herstellung von Kanalstrahlen hoher Voltstahl. *Arkiv for Matematik, Astronomi och Fysik 18, 30*, 1-4

[65] Iwanenko D., & Pomeranchuk I., (1944) On the maximal energy attainable in betatron. *Physical Review 65,* 343.

[66] Kapchinskij, I.M., Vladimirskij, V.V. (1959). *Proceedings of the 2nd International Conference on High Energy Accelerators, CERN, 1959*, 274

[67] Kashikhin, V.S., Carson, J.A., Harding, D.J., Lackey, J.R., Makarov, A., Pellico, W., & Prebys, E.J. (2005). A new correction package for the Fermilab Booster Synchrotron. *Proceedings of the 2005 Particle Accelerator Conference, Knoxville, TN,*n.p.

[68] Kerst, D. W., & Serber, R. (1941). Electronic orbits in the induction accelerator. *Physical Review, 60,* 53–58

[69] Kerst, D.W. (1940). The acceleration of electrons by magnetic induction. *Physical Review, 58* (9)*,* 841

[70] Kerst, D.W. (1941). The acceleration of electrons by magnetic induction. *Physical Review, 60,* 47-53

[71] Lapostolle, P.M. (1971). Possible emittance increase through filamentation due to space charge in continuous beams. *IEEE Trans Nucl Sci. NS-18,* No3*,* 1101-1104

[72] Laslett L.J, & Sessler, A.M. (1965). The asymptotic perturbation field of a longitudinally bunched beam within a rectangular pipe with resistive walls. *SLAC Storage Ring Summer Study SLAC-49,* 23-31

[73] Laslett L.J. (1963) Proceedings of the 1963 Summer Study of Storage Rings, Accelerators and Experimentation at Super-High Energies

[74] Laslett, L.J. (1963). On Intensity limitations imposed by transverse space-charge effects in circular particle accelerators. *Proceedings of the 1963 Summer Study of Storage Rings, Accelerators and Experimentation at Super-High Energies,* 324-378

[75] Laslett, L.J. (1963). On Intensity limitations imposed by transverse space-charge effects in circular particle accelerators. *Proceedings of the 1963 Summer Study of Storage Rings, Accelerators and Experimentation at Super-High Energies*, 341-347

[76] Laslett, L.J., Neil, V.K., Sessler, A.M. (1965). Transverse resistive instabilities of intense coasting beams in particle accelerators. *Rev. Sci. Instr. 36-4*, 436-448

[77] Lawrence, E.O. (1934) "Method and apparatus for the acceleration of ions", U.S. Patent #1,948,384

[78] Lebedev V., Burov, A., Pellico, W., Yang, X. (2006). Coherent instabilities at the FNAL Booster. *Proceedings of HB2006, Tsukuba, Japan,* 69-73

[79] Lebedev, V. Private Communication (Unpublished Result)

[80] Lee, S.Y. (2004). *Accelerator physics (2nd ed.).* Singapore: World Scientific Publishing Co. Pte. Ltd.

[81] Lee, S.Y. (2004). *Accelerator physics (2nd ed.).* Singapore: World Scientific Publishing Co. Pte. Ltd., 241-243

[82] Lee, S.Y. (2004). *Accelerator physics (2nd ed.)*. Singapore: World Scientific Publishing Co. Pte. Ltd., 251-255

[83] Lee, S.Y. (2004). Accelerator physics (2nd ed.). Singapore: World Scientific Publishing Co. Pte. Ltd., 63-64

[84] Lee, S.Y. (2004). *Accelerator physics (2nd ed.).* Singapore: World Scientific Publishing Co. Pte. Ltd.,253

[85] Macridin, A. Private Communication

[86] Mais H., & Ripken, G. (1982). Theory of coupled synchro-betatron oscillations. *DESY internal report, DESY M-82-05,* n.p.

[87] McMillan, E. (1945). The Synchrotron: A proposed high energy particle accelerator, *Physical Review 68,* 143-144

[88] Mokhov, N.V., Drozhdin, A.L., Kasper, P.H., Lackey, J.R., Prebys, E.J., & Webber, R.C. (2003). Fermilab booster beam collimation and shielding. *Proceedings of the 2003 Particle Accelerator Conference, Portland, OR., 1-4*

[89] Nassibian G., & Sacherer, F., (1979). Methods for measuring transverse coupling impedances in circular accelerators. *Nuclear Instruments and Methods, 159*, 21-27

[90] Neil V.K., Sessler, A.M. (1965). *Rev. Sci. Instr., 36*, 429

[91] Ng K.Y., "Coupling Impedances of Laminated Magnets", *Fermilab Note FN-0744*, n.p.

[92] Nielsen, C.E., Sessler, A.M., Symon, K.R. (1959). Longitudinal instabilities in intense relativistic beams. *Proceedings of the International Conference on High Enery Accelerators and Instrumentation, CERN*, 239-252

[93] Pellico, W. Private communication

[94] Piwinski A. (1994). Impedances in lossy elliptical vacuum chambers. *DESY Report No. 94-068*, 1-23

[95] Prebys, E., Lackey, J., Harding, D., & Drennan, C. (2006). Booster corrector systems specification. *Fermilab Beams-doc-1430, n.p.*

[96] Qiang J., Ryne, R.,& Habib, S. (2000). Fortran implementation of object-oriented design in parallel beam dynamics simulations. Computer Physics Communications 133, 18-33

[97] Qiang, J.,Ryne, R., Habib, S., & Decyk, V. (2000). An object-oriented parallel particle-in-cell code for beam dynamics simulation in linear accelerators. *Journal of Computational Physics, 163,* 434-451.

[98] Qiang, J.,Ryne, R., Habib, S., & Decyk, V. (2000). An object-oriented parallel particle-in-cell code for beam dynamics simulation in linear accelerators. *Journal of Computational Physics, 163,* 435-438

[99] Qin H., & Davidson, R.C. (2006). Symmetries and invariants of the oscillator and envelope equations with time-dependent frequency. *Physical Review Special Topics Accelerators and Beams 9* (5)*,* 054001:1-8.

[100] Qin, H., & Davidson, R.C. (2006). An exact magnetic-moment invariant of charged-particle gyromotion. *Physical Review Letters, 96,* 085003:1-4.

[101] Reiser, M. (1994). Theory and design of charged particle beams. New York: John Wiley & Sons, Inc,

[102] Reiser, M. (1994). *Theory and design of charged particle beams.* New York: John Wiley & Sons, Inc, 57, 65

[103] Reiser, M. (1994). *Theory and design of charged particle beams*. New York: John Wiley & Sons, Inc, 63

[104] Robinson K.W. (1965). The wake fields of a charged particle traveling in a vacuum chamber with resistive walls. *SLAC Storage Ring Summer Study SLAC-49,* 32-35

[105] Rotblat, J. (2000, September). Obituary: Mark Oliphant (1901-2000). *Nature 407,* 468

[106] Ruggiero A.G. (1970). Longitudinal space charge forces within bunched beams", *Fermilab note FN-219,* n.p.

[107] Ruggiero A.G. (1971). Energy loss due to resistive magnet lamination in the NAL Booster. *Fermilab note FN-230,* 1-17

[108] Ruggiero A.G. (1971). Longitudinal space charge forces within a bunched beam in the presence of magnetic lamination. *Fermilab note FN-220*, n.p.

[109] Sacherer, F. (1968).Transverse space-charge effects in circular accelerators. *Ph.D. thesis, University of California, Lawrence Radiation Laboratory Report No. UCRL-18454*

[110] Schmidt C.W., (1993). The Fermilab 400-MeV Linac upgrade. *Proceedings of the Particle Accelerator Conference, 1993, Wasington, DC,* 1655-1659

[111] Sessler A., & Vaccaro, V. (1967). Longitudinal instabilities of azimuthally uniform beams in circular vacuum chambers with walls of arbitrary electrical properties. *CERN Report, CERN ISR-RF 67-2*

[112] Shafer, R.E. (1986). Coupling impedance of laminated magnets in the Booster. *Fermilab Technical Memo, TM-1408*

[113] Shiltzev, V. Private communication

[114] Siemann R. (1989). Bunched beam diagnostics. *Cornell U., LNS CLNS-89-878,* 1-44

[115] Sloan D.H., & Lawrence, E.O. (1931). The production of heavy high speed ions without the use of high voltages. *Physical Review, 38,* 2021-2032

[116] Snowdon S.C. (1970). Wave propagation between Booster laminations induced by longitudinal motion of the beam. *Fermilab Technical Memo TM-277,* n.p.

[117] Stahl, S. (1991). Beam dynamics in the Fermilab Booster in the presence of space charge. *Fermilab Thesis-1991-28*, 1-116

[118] Steimel, J. Private Communication

[119] Sutherland, J. Private Communication

[120] Teng, L.C. (1960). Transverse space charge effects. *Argonne National Laboratory ANLAD-59,* 1-22

[121] Thompson, G.P. & Blackman, M. (1946). Improvements in or relating to gas discharge apparatus for producing thermonuclear reactions. *British Patent 817681*

[122] van der Meer, S. (1985). Stochastic cooling and the accumulation of antiprotons. *Review of Modern Physics 57,* 689-697

[123] Veksler, V. I. (1944). New method for accelerating relativistic particles. *Dokladay Akademii Nauk SSSR*, *43*, 346-348 (in Russian)

[124] Vlasov, A.A. (1938). On vibration properties of electron gas. *Journal of Experimental and Theoretical Physics 8* (3)*,* 291

[125] Vlasov, A.A. (1945). On the kinetic theory of an assembly of particles with collective interaction. *Journal of Physics USSR 9* (1), 25–40

[126] Vlasov, A.A. (1968). The vibrational properties of an electron gas. *Soviet Physics Uspekhi* 10, 721

[127] Webber, R. (1989). Longitudinal emittance: An introduction to the concept and survey of measurement techniques including design of a wall current monitor. *AIP Conference Proceedings on Accelerator Instrumentation, 212,* 85–126

[128] Weiland, T. (1983). On the computation of resonant modes in cylindrically symmetric cavities. *Nuclear Instrumentation and Methods*, 216, 31-34

[129] Widerøe R. (1928). On a new principle for the production of higher voltages. *Archiv für Elektrotechnik 21*, 387-391

[130] Worthel, B., & Morgan, J.P. (2004). *Booster rookie book, v.3.0.* FNAL:Booster Staff, 17

[131] Worthel, B., (1998). *The Booster Rookie Book V.3.0.* FNAL: Booster Staff, 3

[132] Worthel, B., (1998). *The Booster Rookie Book.* FNAL: Booster Staff

[133] Zagel, J., Chen, D., & Crisp, J. (1994) Fermilab booster ion profile monitor system using LABVIEW. *The 6th workshop on beam instrumentation, Vancouver,*

Canada, AIP Conference Proceedings, 333, 384-385

[134] Zagel, J., Chen, D., & Crisp, J. (1994) Fermilab booster ion profile monitor system using LABVIEW. *The 6th workshop on beam instrumentation, Vancouver, Canada, AIP Conference Proceedings, 333*, 384-390.

[135] Zotter B. (1968). Boundary conditions at a cylindrical wall of finite conductivity. *CERN Intersecting Storage Rings Document Cern ISH-TH/68-58,* 1-7

[136] Zotter B. (1969). Transverse oscillations of a relativistic particle beam in a laminated beam chamber. *CERN Yellow Report ISRD 69-15,* 1-44

[137] Zotter, B. (1969). Transverse oscillations of a relativistic particle beam in a laminated beam chamber. *CERN 69-15 ISRD*, 27-31